

Pulse Shaping Filter Design and Interference Analysis in UWB Communication Systems

by

Dongsong Zeng

Dissertation Submitted to the Faculty of
The Bradley Department of Electrical and Computer Engineering
Virginia Polytechnic Institute and State University
in partial fulfillment of the requirements for the degree of
DOCTOR OF PHILOSOPHY
in
Electrical Engineering

Co-Chairmen

Dr. Amir I. Zaghloul
Dr. Annamalai Annamalai Jr.

Committee Members

Dr. Jeffrey H. Reed
Dr. Yao Liang
Dr. Yuriko Renardy
Dr. E. F. Charles Laberge

July 20, 2005
Northern Virginia Center, Falls Church, Virginia

Copyright © 2005 Dongsong Zeng

Pulse Shaping Filter Design and Interference Analysis in UWB Communication Systems

Dongsong Zeng

Abstract

Ultra wideband (UWB) is a promising technology for short range and high-speed wireless communications such as home entertainment, wireless video downloading, wireless LAN, wireless USB and so on. This dissertation studied several important issues in the application of UWB technology and its contributions are summarized as follows.

First, a 2-stage optimal UWB pulse shaping filter design procedure is proposed, which not only satisfies the FCC transmission spectral masks but also suppress the multiple access interference (MAI). The major advantages of the proposed joint optimization method are: (1) it has superior MAI suppression capability; (2) it can achieve the best system performance by optimizing transmitting and receiving filters jointly.

Second, a pulse shaping optimizer is proposed to achieve the best received signal-to-noise ratio (SNR). Since the objective function of the SNR optimization has multiple maxima, genetic algorithms are adopted in this all-pass filter optimization.

Third, a novel analytical method of assessing the narrowband performance degradation due to UWB interferences is proposed. This method models the UWB interferences as a composite signal of white Gaussian noise and jamming tones.

Finally, a RAKE receiver simulation model under a realistic UWB channel is proposed and numerical results are presented.

Overall, this dissertation investigates several important issues in the application of UWB technology, and provides some insights on the role of UWB technology in the evolving course of wireless communications.

Acknowledgements

I would like to thank my advisors Dr. Zaghloul and Dr. Annamalai, for their insightful advices, consultations, and discussions. I would acknowledge the committee members, Dr. Reed, Dr. Liang, and Dr. Renardy, for their support in the course of my dissertation.

I would like to acknowledge Honeywell research lab for providing me such an inspirational research environments. Special gratitude is due to Dr. Chuck Laberge for sharing his brilliant ideas with me.

I am grateful to Dr. Tyan, R&D director of Glocom Inc., for his guidance into this field and his encouragement to pursuing higher education.

Thanks to my parents, Senfu and Youzhi, for their constant support and encouragement.

I would like to thank my wife, Jihong, for her taking care of our daughter, while I was writing. And thanks to our lovely daughter, Arin, too. She has been showing interests in my dissertation at her age of two. Their love gives me purpose, strength, and persistence.

Table of Content

1	Introduction.....	1
1.1	UWB Advantages and Disadvantages.....	2
1.2	UWB Applications	5
1.3	UWB History and Literature Review	6
1.4	Comparison of UWB with Existing Wireless Standards.....	10
1.5	UWB Regulations.....	14
1.6	Research Scope and Organization of the Dissertation	16
2	UWB Pulses and Modulation	19
2.1	UWB Pulses	20
2.2	UWB Modulation	24
2.3	Overview of BER Analysis for UWB Systems.....	31
2.4	Summary	36
3	UWB Channel Modeling and RAKE Receiver.....	37
3.1	UWB Channel Model.....	38
3.2	RAKE Receivers	48
3.3	Performance of M -ary Bi-Orthogonal Keying (MBOK) and M -ary Orthogonal Keying (MOK) UWB Signals with RAKE receiver	53
3.4	Summary	60
4	FIR Pulse Shaping Filter	62
4.1	Optimization Problem Formulation.....	64
4.2	Transmitting Filter Optimization.....	68
4.3	Receiving Filter Optimization	73
4.4	Simulation Study	75
4.5	Conclusions	80
5	UWB Pulse Shaping Filter Design with IIR	81
5.1	Elliptic Pulse Shaping Filter Design Procedure	82

5.2	Pulse Shaping Filter with Zero Phase Implementation	92
5.3	Pulse Shaping Filter with Constant Delay through Delay Equalizer	96
5.4	UWB Receiver with Sinusoidal Template	103
5.5	Pulse Shape Optimizer	106
5.5.1	The Effect of Time Offset.....	114
5.5.2	The Effect of Frequency Offset.....	115
5.6	Conclusions	116
6	UWB Interferences to C-band Satellite Receivers	118
6.1	C-band Receivers and UWB devices Overview.....	120
6.2	Separation Distance between UWB Devices and C-band Receivers.....	122
6.3	Power Spectral Density of UWB signals	126
6.4	C-Band Receiver Performance Degradation Due to UBW Interference.....	133
6.5	Conclusions	140
7	Summary.....	142
7.1	Contributions	142
7.2	Future Research Directions	147
8	References	149
9	Appendix A. Instantaneous SER of Common Modulation Schemes.....	163
10	Appendix B. Elliptic Filter Coefficients Calculation Formulas.....	164
11	Vita	166

List of Figures

Figure 1.1 Spatial Capacity of Some Contemporary Wireless Standards	13
Figure 1.2 UWB Indoor Emission Mask	15
Figure 1.3 UWB Out Door Emission Mask.....	16
Figure 1.4 A General UWB Communication System	17
Figure 2.1 UWB Pulses in Time Domain.....	21
Figure 2.2 Power Density Spectra of UWB Pulses	22
Figure 2.3 A simple pulse generator circuit (adapted from [MaLe03])	23
Figure 2.4 Pulse generation example (adapted from [MaLe03]).....	23
Figure 2.5 Application Frequency Ranges of Solid State Technologies.....	24
Figure 2.6 TH-PPM Modulation Example	26
Figure 2.7 TH-BPAM Modulation Example.....	27
Figure 2.8 DS-BPAM Modulation Example	28
Figure 2.9 BER performance vs. SNR of GA and CF methods	34
Figure 2.10 Base-band Equivalent OFDM System Model.....	35
Figure 3.1 UWB Path Loss vs. Distance in LOS and NLOS Channels.....	40
Figure 3.2 Impulse Response of CM1 Channel.....	43
Figure 3.3 Delay Profile of CM1 Channel.....	43
Figure 3.4 Impulse Response of CM2 Channel.....	44
Figure 3.5 Delay Profile of CM2 Channel.....	44
Figure 3.6 Impulse Response of CM3 Channel.....	45
Figure 3.7 Delay Profile of CM3 Channel.....	45
Figure 3.8 Impulse Response of CM4 Channel.....	46
Figure 3.9 Delay Profile of CM4 Channel.....	46
Figure 3.10 MBOK Performances in MRC RAKE Receivers with Different M Values.....	56
Figure 3.11 MBOK Performances in EGC RAKE Receivers with Different M Values	56
Figure 3.12 MBOK Performances in MRC RAKE Receivers with Different L	57
Figure 3.13 MBOK Performances in EGC RAKE Receivers with Different L	57

Figure 3.14 MOK Performances in MRC RAKE Receivers with Different M Values..	58
Figure 3.15 MOK Performances in EGC RAKE Receivers with Different M Values...	58
Figure 3.16 MOK Performances in MRC RAKE Receivers with Different L	59
Figure 3.17 MOK Performances in EGC RAKE Receivers with Different L	59
Figure 4.1 Transmission Filters (41- tap and 81-tap) Coefficients.....	72
Figure 4.2 Transmission Filter Frequency Response	73
Figure 4.3 Component Filter (81-tap) Coefficients	75
Figure 4.4 Relationship between average SINR and number of users	77
Figure 4.5 Relationship between average SINR and power spread.....	77
Figure 4.6 BER performance in LOS channel environment.....	79
Figure 4.7 BER performance in NLOS channel environment.....	79
Figure 5.1 UWB Pulse Shaping Filter Specification	83
Figure 5.2 Amplitude and Phase Response of Analogue Band Pass Filter	86
Figure 5.3 Direct Form II Transposed Implementation of SOS	89
Figure 5.4 Diagram of Granular Zero-Input Limit Cycles	90
Figure 5.5 Limit Cycle Free Diagram for State-Space Implementation of SOS.....	92
Figure 5.6 Theoretical Analog Zero-Phase Filter Structure	93
Figure 5.7 Theoretical Digital Zero-Phase Filter Structure.....	93
Figure 5.8 Theoretic Zero Phase Digital Filter Implementation.....	93
Figure 5.9 Practical Zero Phase Digital Filter Implementation [PoCh91]	94
Figure 5.10 Filtered Monocycle by Zero-Phase Filter Implementation	95
Figure 5.11 Filtered Monocycle by Two Identical Filters of $H(z)$	96
Figure 5.12 Stable Region in (c_{1j}, c_{2j}) Plane	97
Figure 5.13 Phase Response of the Equalized filter	100
Figure 5.14 Group Delay Response of the Equalized Filter	100
Figure 5.15 Zero-Pole Diagram of the Equalizer	101
Figure 5.16 Monocycle Pulse Shape Filtered by Delay Equalizer	102
Figure 5.17 UWB Correlation Receiver	103
Figure 5.18 Filtered UWB Pulses	104

Figure 5.19 Filtered Doublet and Template Wave	105
Figure 5.20 The Proposed UWB Transceiver System.....	107
Figure 5.21 Relationship between Correlation and Biquad Coefficients c_1 and c_2	108
Figure 5.22 General Genetic Algorithm Flow Chart (adapted from [Liu99]).....	109
Figure 5.23 Convergence Process of Optimized Correlation vs. Evolution Times.....	112
Figure 5.24 Comparison of Different Transform Methods in Terms of Phase Response	114
Figure 5.25 The Effect of Time Offset On SNR	115
Figure 5.26 The Effect of Receiving Template Frequency Offset	116
Figure 6.1 The Satellite Forward and Reverse-Link Overview.....	121
Figure 6.2 UWB Interference to C-band Receivers.....	123
Figure 6.3 Gaussian Doublet Pulse in Time Domain	131
Figure 6.4 Gaussian Doublet Pulse in Frequency Domain.....	131
Figure 6.5 Power Spectrum of UWB Pulses without TH-PPM.....	132
Figure 6.6 Power Spectrum of UWB Pulses with TH-PPM.....	132
Figure 6.7 Probability Density Distribution of Single Tone Interference	136
Figure 6.8 Probability Density Distribution of Gaussian Noise	137
Figure 6.9 Probability Density Distribution of Tone plus Noise Interference	138
Figure 6.10 SER vs. SINR under Different TNRs.....	139

List of Tables

Table 1.1 A Brief History of Three Waves of UWB Research	8
Table 1.2 Comparison of Existing Wireless Communication Standards and UWB Technology.....	11
Table 2.1 Numerical Parameters of TH-PPM System.....	33
Table 3.1 Parameter Settings for IEEE UWB Channel Models [BeGi04]	42
Table 3.2 Coherence Bandwidth of UWB Channels	47
Table 4.1 Simulation Parameters for UWB Channel Model	78
Table 5.1 Zero-Pole-Gain Table of the Analogue Band-Pass Filter.....	86
Table 5.2 Filter Coefficients of Direct Form II Transposed Second-Order-Sections.....	88
Table 5.3 Filter Coefficients of the Equalizer	101
Table 5.4 Correlation Comparison for Different Types of Filters.....	112
Table 6.1 An Exemplar C-Band Receiver Reverse-Link Budget.....	122

1 Introduction

Ultra-wide-band (UWB) signal is defined as one whose bandwidth over center frequency ratio is greater than 0.2, or one whose bandwidth is over 500 MHz [FCC02] [CrSc02]. Usually, UWB systems transmit extremely short pulses and occupy an ultra wide frequency bandwidth. Based on its RF simplification and high processing gain, UWB promises low cost implementation with fine time resolution and high throughput in short to medium ranges. Due to its wide bandwidth, UWB has a capability to convey bigger data throughput than conventional narrow band signals. UWB signals include not only carrier-less base-band signals, such as impulse radio or non-sinusoidal pulses, but also wide-bandwidth signals with carriers, such as multi-band orthogonal frequency division multiplexing (MB-OFDM).

Recently the wireless application is growing much more rapidly than wireline services [Leep01]. According to the consulting firm Earnst & Young [Zere99], wireless applications will surpass wire-line applications as the dominant telecommunication technology by 2008. Even though the cellular phones for voice calls have been the most

popular wireless technology so far, the wireless local area network (WLAN) is getting more and more customer acceptance with the latest technological advancements. By the end of 2008, the UWB technology will generate \$1.39 billion revenues world wide according to the prediction of Allied Business Intelligence [Abi03].

Because the potential market of UWB is huge, many industrial heavyweights, such as Intel, Texas Instrument (TI), Motorola, and Samsung, have been investing in UWB technology and UWB related devices. As many practical UWB devices are being designed, an industrial standard is expected to be made. Now a new high-speed wireless standard, IEEE 802.15.3a, is in the making, which will achieve up to 480 Mbps throughput. Two proposals, multi-band OFDM proposed by Intel and TI, and DS-CDMA proposed by Motorola, are competing in the IEEE802.15.3a working group. Final results are expected to come out in the near future. The FCC also granted the frequency range from 3.1 GHz to 10.6 GHz with very little emission power to UWB technology and therefore consolidated the legality of UWB technology. Altogether, UWB is a promising technology for future high-speed wireless communications and has a great potential to penetrate the PC peripherals and consumer electronics market [Abi03] [Leep01].

1.1 UWB Advantages and Disadvantages

Comparing to narrow band signals, UWB signal has the following four main advantages [FCC02]:

1. UWB signals have the capability to convey high-speed data. According to Shannon's communication theory [ShGa67] [WeSh49], the information capacity increases linearly with frequency bandwidth, and decreases logarithmically with the signal to noise ratio. Since UWB has wide

frequency bandwidth, it is inherently suited for high data rate communications. For instance the data rate of the IEEE 802.15.3a proposals can achieve up to 480Mbps. This is a giant leap from the existing 1 Mbps of Bluetooth, 11 Mbps of 802.11b, and 54 Mbps of 802.11a/g.

2. UWB signals have fine range resolution. This enables the use of RAKE receiver techniques in UWB systems. RAKE receiver improves system performance by equalizing signals from different paths. The RAKE receiver can enhance the performance of UWB systems in multi-path channel environments, especially in indoor environments. Due to its fine range resolution, UWB technology can also be applied to location-aware wireless networking such as E911 services. In the wall penetrating radar, UWB signal can precisely track the moving objects behind the wall.
3. UWB communication system is inherently secure. Since the power density of UWB signals is usually below environment noise, only a receiver that knows the schedule of the transmitter can decode the random pulses into a message. Other narrow band receivers cannot even tell the difference of UWB signals from the environment noise. This property of UWB is desirable in highly secure communication systems, such as in military walkie-talkie systems.
4. Impulse radio is carrier-less, so it only has base-band processing and no intermediate frequency (IF) processing is needed. This makes impulse radio devices much cheaper than other communication devices. Since the super-heterodyne architecture was invented by Edwin Armstrong in 1914, almost all communication systems thereafter adopted this technique, in which base-band signal is first up-converted to IF signal by multiplexing with a local oscillator (LO) frequency, then this IF signal is further up-converted to radio frequency (RF) signal. This superheterodyne technique can improve narrow

band receivers' sensitivity. However, in the impulse radio devices, no LO is necessary, no up- or down- converters are needed, therefore, impulse radio devices are simple and of low cost.

While it has all the above advantages, UWB technology also has four major disadvantages:

1. Since UWB signal uses a wide RF bandwidth, its interference with existing narrow band turns out to be a critical problem. This interference could be in two directions: one direction is that narrow band signals can interfere to UWB receivers, such as IEEE 802.11a that shares 5 GHz frequency band with UWB signals; the other direction is that UWB signals may interfere into narrow band receivers. For instance, GPS signals are usually of low power density, so it is vulnerable to UWB interference. However, without sacrificing much system performance, the interference of UWB to legacy systems can be mitigated through pulse shaping filter and different modulation scheme.
2. Since UWB pulses are very short in time domain, high-speed ADC (Analog to Digital Converter) and high-speed DSP are essential for UWB systems to digitize and process UWB signals.
3. UWB systems require wide-band antennas. Traditional frequency selective antennas could not keep constant amplitude and constant group delay for a wide frequency bandwidth. Instead, wide-band antennas, such as discone antenna, logarithmic antenna, etc., have to be adopted. However, wide-band antennas are bigger and more expensive than narrow-band antennas, designing a small and inexpensive antenna is crucial for UWB technology to be widely deployed.

4. UWB communication systems are limited in range. In order to make UWB interference to other radio systems insignificant, the transmission power of UWB signals has to be bounded under the emission mask set by the FCC. The low output power leads to smaller coverage area. In general, with high gain antenna, UWB signals may cover up to one kilometer. But with regular antennas, the range of UWB signals is usually from ten to twenty meters.

1.2 UWB Applications

The applications of UWB can be categorized into four categories, i.e., communications, distance determinations, remotely sensing radar, and vehicular radar [FCC02].

1. **Communications:** UWB transceivers can send and receive high-speed data with very low power at relatively low cost. UWB communication systems are often advantageous in short-range wireless (SRW) market segment, which is very active now and poised for fast growth in the future. Currently, UWB technologies are primarily targeting at indoor applications within several to dozens meters at bit rates up to hundreds of megabits per second, such as cable replacement, home entertainment, and high speed wireless LAN communications.
2. **Distance determination:** Due to its precise time resolution, UWB technique may also be used to determine the separation distance between two objects. For instance, inside water tanks, UWB radar can be used to measure the height of the water surface. UWB radar on the ship may sense the rail height relative to the water line. UWB radar can be used to measure not only the level of a single layer, but also the levels of multiple layers. For instance, in the crude oil tank, UWB radar can measure the levels of oil, emulsion, and water layers at the same time.

3. **Remote sensing of objects:** UWB radars may be used to detect and image the objects inside enclosed spaces or behind walls. Ground-penetrating radars (GPRs) can sense the presence of pipes or land mines. Placed outside a room or a house, UWB radar may be used to determine or image the positions of people inside the rooms.
4. **Vehicular Radar:** Vehicular radars use the frequency band surrounding 24 GHz to measure the location and movement of objects around a vehicle by transmitting UWB pulses and detecting the reflected signals. These devices enable the features such as auto navigation, collision avoidance, improved airbag activation, intelligent suspension systems, etc.

Throughout the full range of UWB applications, applying UWB into short-range high-speed wireless communication is currently one of the most active areas. A lot of research is being conducted. Many big companies, such as Intel, TI, and Motorola, have already invested a huge amount of money in the research and development of UWB technology. The era of UWB technology has just started.

1.3 UWB History and Literature Review

Even though UWB communications got a lot of research attention only recently, its history can be traced back to over one hundred years ago. The first wave of UWB study started when James Clark Maxwell first proposed the electromagnetic theory at the end of 19th century, in which he formulated the law of electromagnetism into the following four equations.

$$\nabla \cdot E = 4\pi\rho \tag{1.1}$$

$$\nabla \times E = -\frac{1}{c} \frac{\partial B}{\partial t} \tag{1.2}$$

$$\nabla \cdot \mathbf{B} = 0 \quad (1.3)$$

$$\nabla \times \mathbf{B} = \frac{4\pi}{c} \mathbf{J} + \frac{1}{c} \frac{\partial \mathbf{E}}{\partial t} \quad (1.4)$$

In equations (1.1) to (1.4), notation $\nabla \times$ denotes the curl operation, $\nabla \cdot$ denotes the divergence operation, \mathbf{E} represents the electric field, \mathbf{B} represents the magnetic field, \mathbf{J} is the vector of the current density, ρ is the charge density, and c is the speed of light.

It was this theory that started the first wave of UWB research and broke a new ground of modern electric and electronic applications. Since then, tremendous advancements of UWB research had been achieved. Several years after Maxwell published his theory, Hertz demonstrated the propagation of electromagnetic wave through space in his laboratory. But at that time, Hertz couldn't foresee the usage of this electromagnetic wave. He told his students that this demonstration was just an experiment that proved Maxwell was right. In 1895, Marconi invented and patented his spark gap generator, which was used to transmit Morse telegraph codes. Pressing the telegraph key causes current to flow in the primary side of coil, and introduces a high voltage in the secondary coil. A discharge arc was then created to excite the antenna and produce a RF signal. Since the RF signal has a wide frequency band, this electric spark gap generator is considered the first UWB signal generator. Later, Nikola Tesla invented similar polyphase AC generator. The first wave of UWB research was halted due to World War I and II.

The second wave of UWB research was from 1960s to 1990s. During this period, many research and national laboratories got involved in the UWB research, which mainly focused on radar and highly secure communications. For instance, Harmuth wrote prolifically on the electromagnetics of UWB signal transmission and reception in both radar and communication systems [Harm72], [Harm75], [Harm78], and [Harm81]. Ross and Robin deployed the UWB theory into many radar and communication applications [RoRo87], [RoRo873], and [Ross73]. In the 1960s, both Los Alamos National Laboratory (LANL) and Lawrence Livermore National Laboratory (LLNL) conducted

tremendous amount of research on pulse transmitters, antennas, and receivers. In 1974, Geophysical Survey Systems, Inc. invented ground penetrating UWB radar [Barr00].

Table 1.1 A Brief History of Three Waves of UWB Research

UWB research waves	Time	Representative names	Major research achievements
First Wave	From the end of 19 th century to world war I	Maxwell, Hertz, Marconi, etc.	Fundamental electromagnetic theory and basic practice.
Second Wave	From 1960s to 1990s	Harmuth, Ross, Robins, Barret, etc.	Basic design for UWB transmitters and receivers in the areas of radar and high secure communications.
Third Wave	From 1990s to now	Scholtz, Win, IEEE802.15g working group, etc.	UWB for commercial high speed, short-range wireless communications.

The third wave of UWB research started when a series of papers by Scholz and Win stirred up both academic and industrial interests of UWB's capability in high-speed wireless communications in 1990s. In this wave, the UWB research focused more on communication methodology and commercial short-range wireless applications such as wireless LAN and home entertainment, etc. Some representative papers of Win and Scholtz are briefed in the following. [WiSc97] demonstrated both analog and digital impulse radio structures for wireless multiple access communication systems. [WiRa97] and [WiSc02] studied the indoor and outdoor UWB propagation channel characteristics. [WiSc98a], [WiSc98b], and [Win98] analyzed the UWB signal power spectral density and performance in multi-path channel environments. [WiSc00] investigated the time-

hopping spread spectrum in UWB multiple access communication systems. The three waves of UWB researches are summarized in Table 1.1.

Based on the plural fundamental research of UWB and enormous market demand for high speed wireless connection, the IEEE (Institute of Electrical and Electronics Engineers) 802.15.3a work group is tasked to draft and publish a new standard, which is expected to enable a new class of high speed wireless applications, such as wireless DVDs, digital still and video cameras, and wireless USB.

In developing the best technical solution for the emerging UWB specification, the work group has been divided into two camps. One camp is called the Multi-Band OFDM Alliance (MBOA), which is led by Texas Instruments and Intel, and followed by Samsung Electronics, Panasonic, Hewlett Packard and many other companies. These companies support the proposal, which was originally introduced by Texas Instruments in March 2003. The other camp, involving Motorola, ParthusCeva, etc., supports a rival proposal based on direct sequence code division multiple access (DS-CDMA).

In the vote meeting in Albuquerque, N.M., in November, 2003, MBOA won the majority votes. However, the proposal was not be able to reach the 75-percent approval that is required to confirm it. The final tally was 96 votes for the MBOA proposal, 69 against it, with three abstentions. That neither proposal has been passed to be a UWB standard raises the likelihood that de facto UWB standards may emerge in the industry. Even though the new standard is still in the making, the commercial applications of UWB technology are expected to be available in the near future.

1.4 Comparison of UWB with Existing Wireless Standards

Currently, four wireless standards, i.e., Bluetooth, IEEE802.11a, IEEE802.11b, and IEEE802.11g, are commonly used in north America. In Europe and Japan, HiperLan II is also widely used, whose physical layer is similar to IEEE802.11a.

The Bluetooth radio employs frequency hopping spread spectrum (FHSS) with totally 79 hops. The frequency hopping range is from 2.402GHz to 2.480GHz. Its baseband modulation uses Gaussian Frequency Shift Keying (GFSK), where a binary one is carried out by a positive frequency deviation and a binary zero by a negative frequency deviation. The power control of Bluetooth devices is realized using 3 power classes. Power Class 1 is designed for long range (about100m) devices, with a max output power of 20 dBm. Power Class 2 is for ordinary range devices (about 10m) devices, with a max output power of 4 dBm. Power Class 3 is for short-range devices (about 10cm) devices, with a max output power of 0 dBm.

802.11b employs direct sequence spread spectrum (DSSS) with complementary code keying (CCK) base-band modulation. Its RF spectrum occupies 83.5 MHz bandwidth (for North America) from 2.4000 GHz to 2.4835 GHz. 802.11b has 11 channels, each of which is 22 MHz wide, and offers data speeds up to 11Mbps. Currently 802.11b is the most widely used standard for PC wireless communications.

802.11a adopts OFDM technology. Its frequency spectrum occupies 300 MHz in three different bandwidths of 100 MHz each. These three bandwidths are UNII (Unlicensed National Information Infrastructure) lower band (5.150 to 5.250 GHz), UNII middle band (5.250 to 5.350 GHz), UNII upper band (5.725 to 5.825 GHz). 802.11a provides 12 channels of 20 MHz each and can offer data rate up to 54 MHz.

802.11g offers data speeds up to 54Mbps, and operates at radio frequency between 2.4 GHz and 2.4835 GHz. 802.11g uses 802.11b's Complementary Code Keying (CCK) to achieve bit transfer rates of 11Mbps. In addition, 802.11g adopts 802.11a's Orthogonal Frequency Division Multiplexing (OFDM) modulation for data rate of 54Mbps. 802.11g is compatible with 802.11b, but not compatible with 802.11a since 802.11g and 802.11a operate at different frequency bands.

Table 1.2 Comparison of Existing Wireless Communication Standards and UWB Technology

	Bluetooth	IEEE802.11b	IEEE802.11g	IEEE802.11a	UWB
Frequency Band	2.4 GHz	2.4 GHz	2.4 GHz	5 GHz	3-10GHz
Max Transmit rate	725 kbps	11 Mbps	54 Mbps	54 Mbps	480 Mbps
Modulation	FHSS	DSSS	OFDM	OFDM	Multi-band OFDM or DS-CDMA

IEEE 802.15.3a will achieve up to 480 Mbps throughput with UWB technology. Now there are two candidate proposals, i.e., MB-OFDM and DS-CDMA, are competing for the standard. DS-CDMA proposal has two frequency bands: one is from 3.1 GHz to 5.15 GHz, and the other is from 5.825 GHz to 10.6 GHz. *M*-ary bi-orthogonal keying (MBOK) is employed in data bit modulation. On the other hand, MB-OFDM proposal divides the frequency range from 3.1 GHz to 10.6 GHz into totally 13 frequency bands, and each frequency band is 528 MHz wide. There are 128 sub-carriers inside each frequency band, each sub-carrier has a 4.125 MHz bandwidth. Among these 128 sub-carriers, 6 of them are unused, 12 of them are pilot tones, 10 of them are guard tones, and the rest 100 sub-carriers are used to carry data. Both MB-OFDM and DS-CDMA proposals can achieve 480 Mbps throughput, which is much faster than those of existing

wireless standards. Some key characteristics of existing wireless standards and UWB technology are summarized in Table 1.2.

From the perspective of spatial capacity, UWB is also advantageous over other wireless standards. Spatial capacity is usually measured by data bits transmitted per cubic meter. However, [Leep02] and [shel02] argue that since we are living on the surface of the earth, data bits per square meter are of more interest. So in the following study, bits per square meter are employed to calculate spatial capacity.

Bluetooth has a range of about 10 meters in free space. In a circle with a 10-meter radius, approximately 10 Bluetooth piconets can operate simultaneously, the aggregate over-the-air speed is about 7 Mbps. Divided by the area of the circle, this yields a spatial capacity of approximately 22 Kbps/m².

IEEE 802.11b devices have a range of about 100 meters in free space. In a circle with a 100-meter radius, three IEEE 802.11b systems can operate simultaneously, each offering a peak over-the-air speed of 11 Mbps. The total aggregate speed of 33 Mbps, divided by the area of the circle, yields a spatial capacity of approximately 1 Kbps/m².

IEEE 802.11a has a range of about 20 meters in free space. In a circle with a 20-meter radius, twelve IEEE 802.11a devices can operate simultaneously, each offering a peak over-the-air speed of 54 Mbps. The total data rate (648 Mbps), divided by the area, yields a spatial capacity of approximately 515 Kbps/m².

IEEE 802.11g has a range of about 50 meters in free space. In a circle with a 50-meter radius, twelve IEEE 802.11g devices can operate simultaneously, each offering a peak over-the-air speed of 54 Mbps. The total data rate (648 Mbps), divided by the area, yields a spatial capacity of approximately 83 Kbps/m².

UWB has a projected range of about 15 meters in free space. In a circle with a 15-meter radius, 15 UWB systems can operate simultaneously, each offering a peak over-the-air speed of 480 Mbps. The total data rate is 7200 Mbps. The spatial capacity, i.e., data rate per square meter, is approximately 10 Mbps/m².

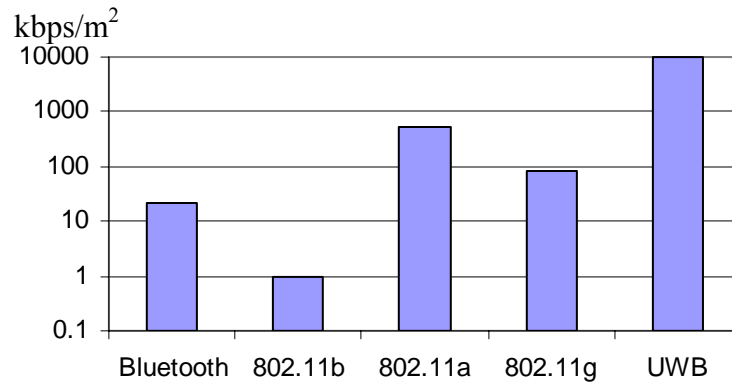


Figure 1.1 Spatial Capacity of Some Contemporary Wireless Standards

As shown in Figure 1.1, the UWB technology has better spatial efficiency over all other existing wireless standards. It is worth to note that spatial capacity is rather a vague concept. The above calculations are based on the specifications of the standards. In the real world, the data rates over different distances for a wireless standard are different. The data reported by different company or different resources may also be different. To precisely calculate the spatial capacity for real world application is almost impossible and unnecessary.

Power consumption is also an important perspective for wireless devices. The transmission power of Bluetooth devices power is about 100 mW, 802.11b output power is about 200 mW, 802.11a output power is from 40 mW to 800 mW, and 802.11g transmission power is about 65 mW [Stro03] [AiRo03]. The transmission power of UWB devices is only 1 mW, which is significantly lower than those of Bluetooth, 802.11b/a/g.

Since UWB devices consume much lower power than other wireless products, some researchers are considering applying UWB devices in wireless sensor networks. The advantages of UWB devices in sensor networks are: (1) UWB devices are easy to have precise distance information (2) more nodes can be accommodated in the network (3) good for real time control applications where response time is more important (4) UWB devices consume lower power. The disadvantages of UWB devices in sensor networks are: (1) overkill for low data rate, slow response applications (2) potential interferences to legacy devices.

1.5 UWB Regulations.

In 1998, FCC recognized the importance of UWB technology and began the process of regulatory review. In February 2002, FCC made the formal rule that permits Ultra Wideband to operate under certain indoor and outdoor power spectral masks.

As shown in Figure 1.2, for indoor applications, the emission power of UWB devices should be below -41.3 dBm/MHz from 0 Hz to 0.96 GHz, below -75.1 dBm/MHz from 0.96 GHz to 1.61 GHz, below -53 dBm/MHz from 1.61 GHz to 1.99 GHz, below -51.3 dBm/MHz from 1.99 GHz to 3.1 GHz, below -41.3 dBm/MHz from 3.1 GHz to 10.6 GHz, below -51.3 dBm/MHz from 10.6 GHz above. As shown in Figure 1.3, for outdoor applications, the emission power of UWB devices should be below -41.3 dBm/MHz from 0 Hz to 0.96 GHz, below -75.1 dBm/MHz from 0.96 GHz to 1.61 GHz, below -63.3 dBm/MHz from 1.61 GHz to 1.99 GHz, below -61.3 dBm/MHz from 1.99 GHz to 3.1 GHz, below -41.3 dBm/MHz from 3.1 GHz to 10.6 GHz, below -61.3 dBm/MHz from 10.6 GHz above.

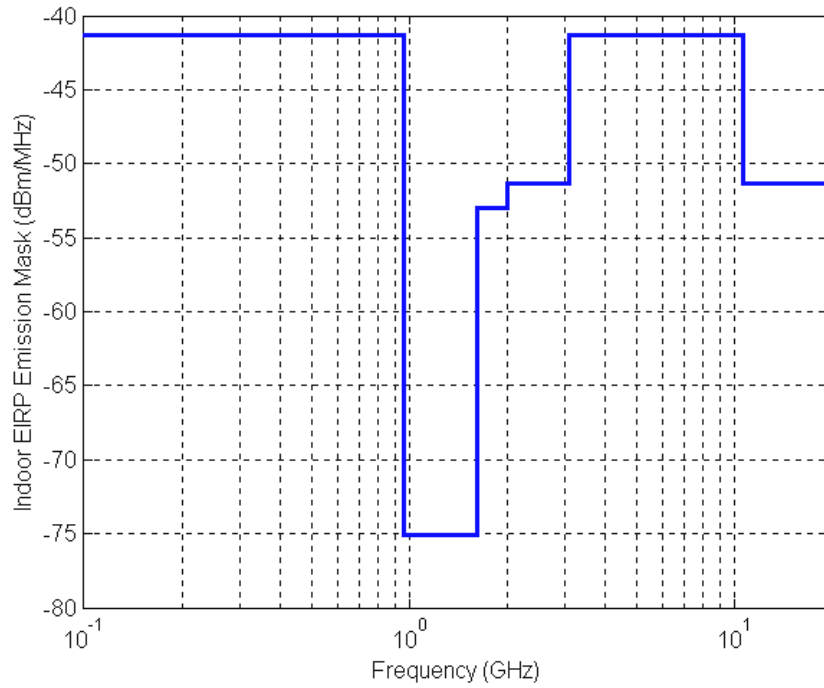


Figure 1.2 UWB Indoor Emission Mask

The emission limits are defined as the effective isotropic radiated power (EIRP) in terms of milli-watt per 1 MHz bandwidth. The emitted power measured from a radiator can be expressed as:

$$p = E_0^2 4\pi R^2 / \eta \quad (1.5)$$

Notation E_0 denotes the electric field strength with a unit of V/m. Notation R represents the radius of the sphere at which the field strength is measured. Notation η is the characteristic impedance. In vacuum space, η equals to 377 ohms. For instance, the power spectral density of -41.3dBm/MHz is equivalent to the electric strength of $500 \mu\text{V}/\text{m}$ measured at a distance of 3 meters away from the radiator in a 1 MHz resolution bandwidth.

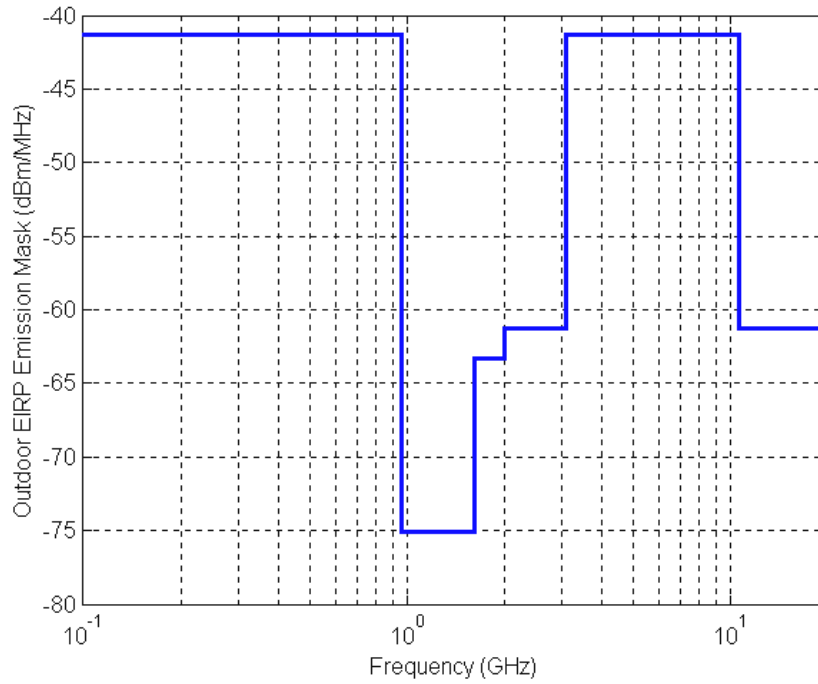


Figure 1.3 UWB Out Door Emission Mask

1.6 Research Scope and Organization of the Dissertation

A general UWB communication system can be delineated in Figure 1.4. On the transmitting side, the incoming data stream is first encoded and modulated. All encoding methods for narrowband, such as convolutional codes, block codes, turbo codes, etc., are all applicable to UWB systems. In the encoding process, other schemes such as interleaving, scrambling, and puncturing are often employed to randomize the appearances of spaces and marks, and to enhance system immunity to multi-path fading. The UWB modulation types include time hopping pulse position modulation, time hopping pulse amplitude modulation, direct sequence pulse position modulation, multiple-band OFDM, etc. The modulated signal is then multiplexed with the pulses

generated by pulse generator. The multiplexed pulses will then go through pulse shaping filter and transmission antenna, and finally get on the air.

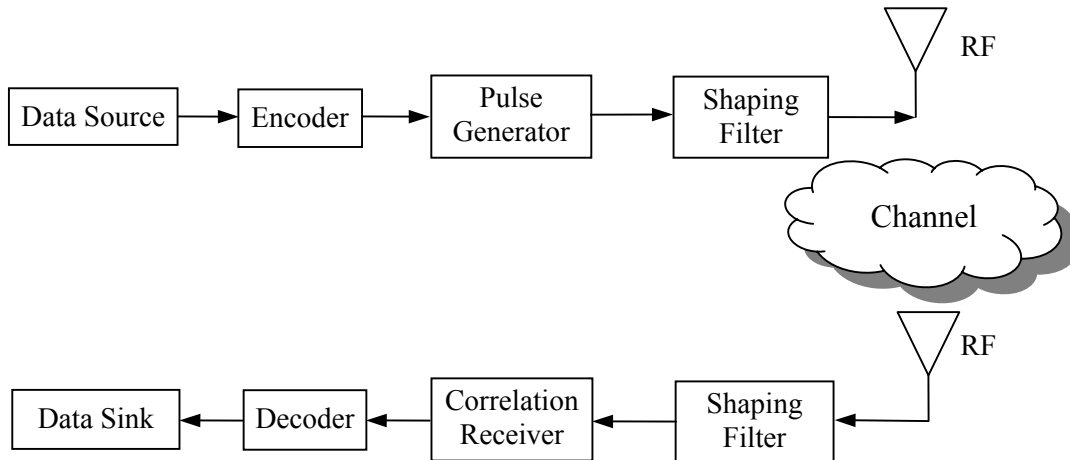


Figure 1.4 A General UWB Communication System

On the receiving side, the UWB signal is first captured by a receiving antenna. Second, the signal is filtered with a matched filter, which is usually the same as the transmitting pulse shaping filter. Third, the filtered signal is demodulated and decoded. The demodulation process is the inverse process of the modulation. The decoding methods, such as Viterbi decoder, turbo decoder, and sequential decoder, which are used in narrowband communications, can also be applied in UWB systems. If the interleaving, scrambling, and puncturing are used in the transmitter, de-interleaving, de-scrambling, and de-puncturing should be conducted accordingly in the receiver.

The scope of this research covers the UWB pulse shaping filter design, UWB modulation types, channel models, performances and interferences, etc. This dissertation is organized as follows. Chapter 2 discusses UWB modulation types and its SNR and BER analysis methods. Chapter 3 talks about UWB channel models and RAKE receivers. Chapter 4 proposes a joint optimal pulse shaping filter design procedure with a FIR (Finite Impulse Response) approach, which can not only suppress

UWB interference to satisfy the FCC requirements, but also achieve the best system performance at the same time. Chapter 5 proposes a pulse optimizer design procedure, which can improve the receiver's SNR performance. Chapter 6 studies the interference of the UWB devices to C-band receivers. Chapter 7 summarizes the findings and concludes the dissertation.

2 UWB Pulses and Modulation

Impulse radio is based upon transmitting and receiving very short pulses. Pulse generation and pulse shaping are among the most fundamental problems in UWB systems. Three types of UWB pulses have often appeared in the recent UWB research literature, i.e., Gaussian pulse, monocycle pulse, and doublet pulse. These pulses are usually employed to conduct basic theoretic analysis and simulation study. The information bits are embedded in the transmitted pulse sequence. Many UWB modulation types, such as time hopping pulse position modulation, time hopping binary phase and amplitude modulation, direct sequence spread spectrum, and orthogonal frequency division modulation, are commonly used in the UWB communication systems. Bit-error-rate (BER) is usually used to evaluate the performance of UWB communication systems. The BER analysis methods of UWB pulse systems can be categorized into two classes. One is based upon the Gaussian assumption, and it is

named GA method. The other doesn't have to assume Gaussian distribution, and it derives the BER through characteristic function (CF). So it is called CF method. Since CF method doesn't need to make any assumption, it is considered more accurate than GA method in theory. In particular, when the interference in UWB systems is not close to Gaussian distribution, GA method may cause bigger errors than CF method does. That is why CF method is preferred in the BER analysis of UWB systems. Like always, although the CF method is more accurate, it is more complex too. Gaussian assumption makes the BER analysis simpler to calculate and easier to understand. Whenever it is reasonable to make Gaussian assumption in the real world applications, most engineers prefer GA method.

In the rest of this chapter, three types of UWB pulse, i.e., Gaussian pulse, Gaussian monocycle, and Gaussian double, are introduced first. Then some circuits and solid-state technologies, which are used in pulse generation, are described. Third, several popular UWB modulation types are explained and compared. Finally, two general bit error rate analysis methods, i.e., Gaussian assumption method and characteristic function, are analyzed in theory and compared with numerical results.

2.1 UWB Pulses

In most UWB literature, three types of UWB pulses are usually employed, i.e., Gaussian pulse, Gaussian monocycle, and Gaussian doublet. Gaussian pulse has a shape of Gaussian distribution. It is worth to note that Gaussian pulses remain Gaussian distribution when they pass through any linear systems. A general formula of Gaussian pulse is shown in equation (2.1), in which τ is a time constant. Gaussian monocycle is the first derivative of Gaussian pulse and Gaussian doublet is the second derivative of Gaussian pulse. The general formulas for Gaussian monocycle and Gaussian doublet are shown in equation (2.2) and (2.3) respectively.

$$g_0(t) = -e^{-\left(\frac{t-t_0}{\tau}\right)^2} \quad (2.1)$$

$$g_1(t) = -\frac{t-t_0}{\tau} e^{-\left(\frac{t-t_0}{\tau}\right)^2} \quad (2.2)$$

$$g_2(t) = \left[1 - 4\pi\left(\frac{t-t_0}{\tau}\right)^2\right] e^{-2\pi\left(\frac{t-t_0}{\tau}\right)^2} \quad (2.3)$$

Notation τ is a time constant and t_0 is a time offset. The three pulses, i.e., Gaussian pulse, monocycle, and doublet, are compared in time domain in Figure 2.1. It can be seen that Gaussian pulse has no zero crossing point, monocycle has one zero crossing, and doublet has two zero crossings.

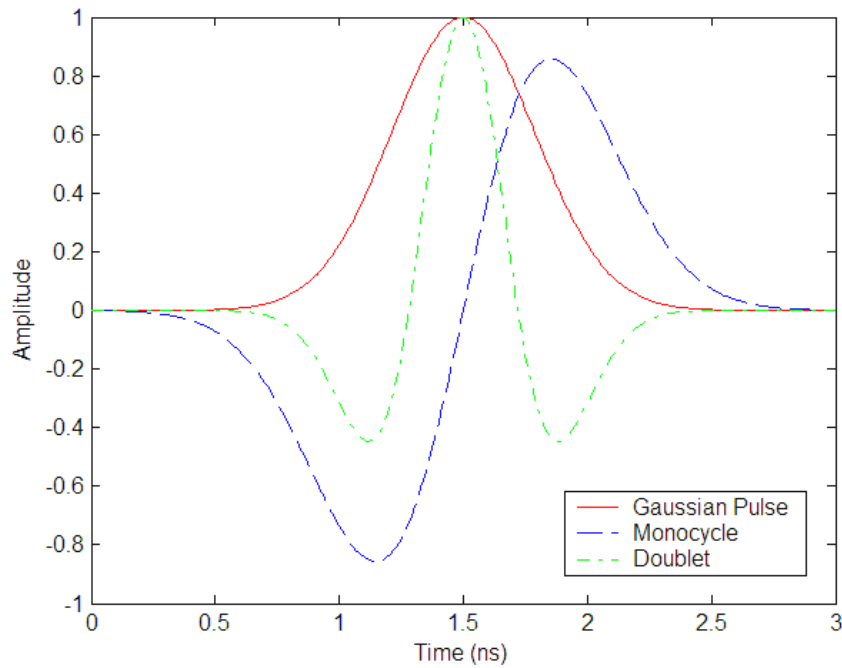


Figure 2.1 UWB Pulses in Time Domain

The power density spectra of the three pulses are examined side by side in Figure 2.2. The power density spectrum of Gaussian pulse centers at zero frequency. The power

density spectrum centers of monocycle and doublet are skewed to higher frequency, and doublet is more skewed than monocycle is.

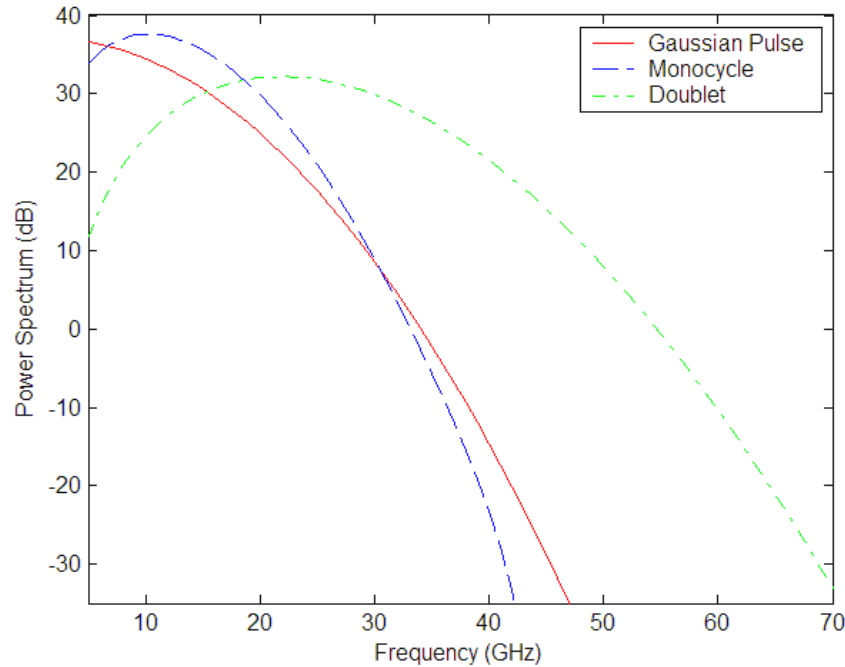


Figure 2.2 Power Density Spectra of UWB Pulses

As to the generation of UWB pulses, a variety of circuits have been proposed so far [MaLe03]. In UWB communication systems, transistors and diodes are commonly used to generate the pulses. A simple pulse generator circuit described in [MaLe03] is shown in Figure 2.3, in which a, b, c, d are the control taps of the four MOSFET (metal oxide semiconductor field effect transistor) transistor, L denotes an inductor, and C represents a capacitor for DC blocking. By switching control taps a, b, c, and d from GND to Vdd or from Vdd to GND, a pulse voltage is generated on the load. For instance, initially the control taps a, b, c, and d are set to Vdd, GND, GND, and Vdd respectively. In the stable state, there is no current flowing through the load. When the control tap, a, switches to GND, this transistor turns off. The current inside transistor, a, will deviate to the load. This results in a positive slope of a pulse. After some delay, transistors b and c

are turned on. Finally, transistor d is turned off. The transistors transient process and the resultant pulse generation are illustrated in Figure 2.4.

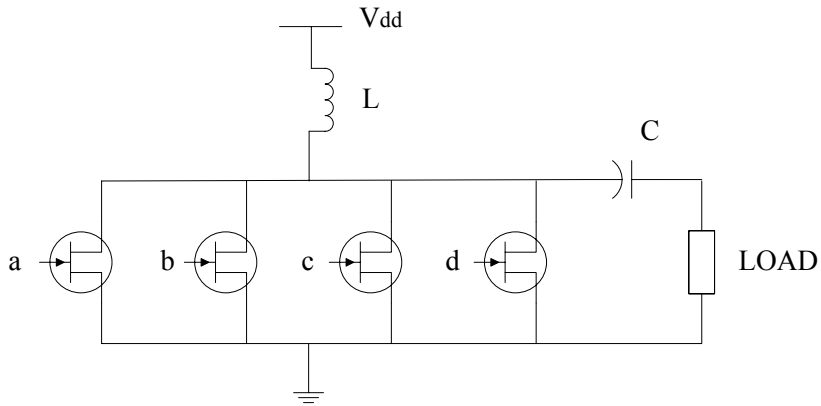


Figure 2.3 A simple pulse generator circuit (adapted from [MaLe03])

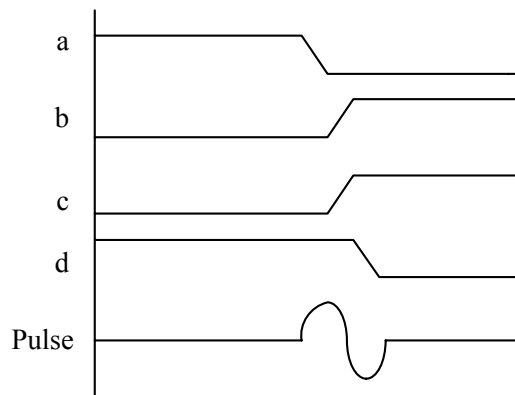


Figure 2.4 Pulse generation example (adapted from [MaLe03])

The pulse width depends up on both the circuit architecture and the semiconductor materials, which are used to generate the pulse. So far four types of materials have been used in manufacturing transistors: (1) Silicon (Si); (2) Gallium Arsenide (GaAs); (3) Silicon Germanium (SiGe); (4) Indium Phosphide (InP).

In general, Si is used for low frequency applications and it is the most inexpensive material. For pulses with frequency bandwidth less than 10 GHz, Si is usually the best

option. GaAs is used in higher frequency applications, where Si simply doesn't work as well as GaAs does. Currently, the power amplifiers in cell phone handsets are almost all made of GaAs. SiGe not only has better linear performance than GaAs, but also is more power efficient. In the next generation of mobile wireless devices, more and more SiGe is expected to be used. InP has the lowest noise of all materials known today at very high frequencies (>40 GHz). But right now InP is too expensive to be widely used in engineering practice. The application frequency ranges for the four solid state technologies are summarized in Figure 2.5.

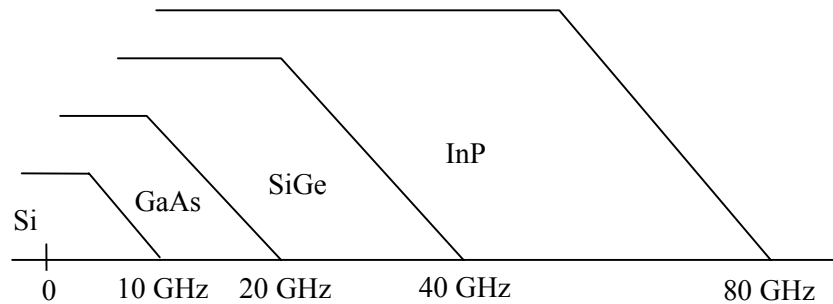


Figure 2.5 Application Frequency Ranges of Solid State Technologies

[Yeap04] prototyped real world UWB pulse generator using Step Recovery Diode (SRD). The low cost sub-nanosecond impulse generator consists of SRD and filtering network that matches to 50 ohms. The impulse generator is driven by a continuous sinusoidal waveform (CW) of 100 MHz at 10dBm. The ring effect on the pulse tail is effectively suppressed. At this stage, the entire components cost of the UWB pulse generator is less than \$0.60, and the pulse width is within sub-nanoseconds.

2.2 UWB Modulation

There are a variety of UWB modulation types that are used to build UWB systems. Some of them modulate information bits directly into very short pulses. Since there is

no IF (Intermediate Frequency) processing in such systems, they are often called base-band processing, or impulse radio system. Some well-known modulation types, such as time hopping pulse position modulation, time hopping pulse amplitude modulation, and direct sequence pulse amplitude modulation, are in the category of impulse radio. On the other hand, some UWB systems do have carriers. For instance, in the orthogonal frequency division multiplexing (OFDM) system, the information bits are modulated into orthogonal carriers. The IEEE 802.15.3a candidate physical layer specification proposed by MBOA (Multi-band OFDM Association) extends conventional OFDM to multi-band UWB OFDM. This candidate proposal has gained a majority support from the working group in the meeting in Albuquerque, New Mexico, 2003, and is very promising to become the standard in the future.

Time-hopping pulse position modulation (TH-PPM) impulse radio [WiSc00] is built upon the position shift of pulses with a certain shape in time domain. A UWB system with TH-PPM could accommodate multiple users simultaneously through code division multiple access. In TH-PPM UWB system, the impulse radio signal from the k -th transmitter is generally expressed as:

$$s_k(t) = \sum_{i=0}^{\infty} \sum_{j=0}^{N_s-1} \delta(t - jT_f - c_{k,j}T_c - iT_b - b_i\Delta) \otimes g(t) \quad (2.4)$$

In equation (2.4), notation $g(t)$ denotes the transmission pulse shape function, notation \otimes represents the convolution operation, and the delta function, $\delta(t)$, is defined as:

$$\begin{cases} \delta(t) = 1, & t = 0 \\ \delta(t) = 0, & t \neq 0 \end{cases}$$

The term $\delta(t - jT_f - c_{k,j}T_c - iT_b - b_i\Delta) \otimes g(t)$ indicates that the j -th pulse transmitted by the k -th user starts at time epoch $t - jT_f - c_{k,j}T_c - iT_b - b_i\Delta$. In Equation (2.4), the sequence set $\{c_{k,j}\}$ is a pseudo-random time-hopping sequence for user k , and the range of $c_{k,j}$ is between 1 and the number of hopping positions, N_h . In multiple-access

systems, each user has a distinct pseudorandom sequence to distinguish one from the others. Notation T_c is the chip duration and T_f is the frame duration, which is greater than or equal to $N_h T_c$. The ratio of $N_h T_c$ over T_f , i.e., $R_{frac} = N_h T_c / T_f$, represents the fraction of time over which time hopping sequence occupies. If R_{frac} is too small, the number of hopping positions is too small and collision probability may increase significantly. Notation b_i is information bit sequence of 1s and 0s and Δ is time position difference between pulse 0 and pulse 1. The information bit duration is represented by T_b , the number of hops in each bit duration is signified by N_s , and T_b equals N_s times frame duration, T_f , i.e., $T_b = N_s T_f$.

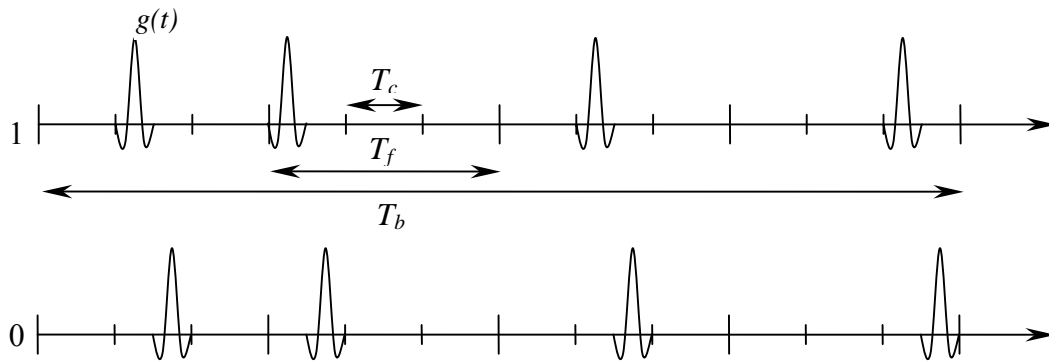


Figure 2.6 TH-PPM Modulation Example

An example of pulse trains for binary data bit 1 and 0 are demonstrated in Figure 2.6, in which the first pulse train is transmitting binary bit 1, and the second pulse train is sending binary bit 0. The only difference between the two is that all pulses in pulse train 0 are delayed a little bit comparing to the pulses in pulse train 1.

Time hopping binary pulse amplitude modulation (TH-BPAM) is another type of UWB modulation, which interests many researchers. The pulse amplitude of information bit 1 is set to unit, while the pulse amplitude of information bit 0 is set zero. By setting the pulse on and off, binary information bits, 0 and 1, are sending out. Similar to TH-PPM,

the TH-BPAM signal from the k -th transmitter is expressed in equation (2.5), where notation b_i denotes the i -th binary sequence bit.

$$S_k(t) = \sum_{i=0}^{\infty} \sum_{j=0}^{N_s-1} \delta(t - iT_b - jT_f - c_{k,j}T_c) \otimes g(t) * b_i \quad (2.5)$$

An example pulse train of TH-BPAM is shown in Figure 2.7. In this example, a binary bit sequence, 1, 0, 1, 1, are modulated into a pulse train, in which there is one pulse sent out when the data bit is 1, and there is no pulse sent out when the corresponding data bit is 0.

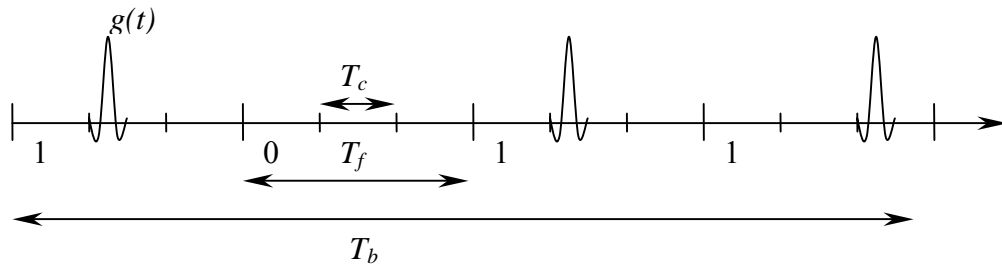


Figure 2.7 TH-BPAM Modulation Example

Direct sequence binary pulse amplitude modulation (DS-BPAM) UWB signal can be expressed in equation (2.6), in which the spreading sequence $c_{k,j}$ takes on 0 or 1 and is multiplied into signal amplitude.

$$S_k(t) = \sum_{i=0}^{\infty} \sum_{j=0}^{N_s-1} \delta(t - iT_b - jT_c) \otimes g(t) * c_{k,j} * b_i \quad (2.6)$$

An example of DS-BPAM is demonstrated in Figure 2.8, where data bit 1 is spread into a binary sequence of 010100011001. The processing gain, PG , of DS-BPAM is defined as the ratio of the RF spread bandwidth to the bandwidth of the information signal at the receiver output, i.e.,

$$PG = 10 \log(T_b / T_c) \quad (2.7)$$

Notation T_b is the data bit period, and notation T_c is the chip period.

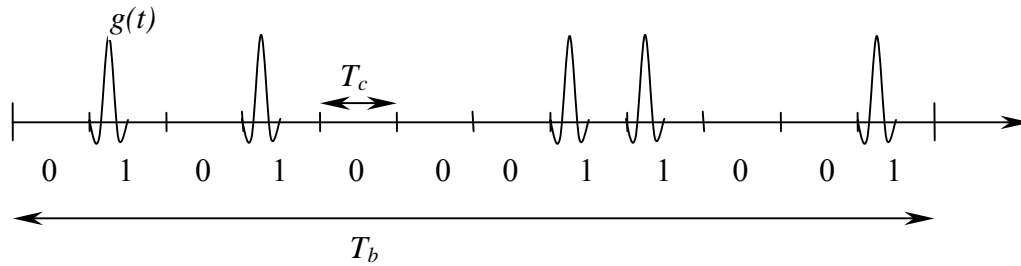


Figure 2.8 DS-BPAM Modulation Example

Orthogonal Frequency Division Multiplexing (OFDM) modulation can also be used in UWB communication systems. OFDM was invented more than 40 years ago. Now it has been widely adopted in numerous industrial standards such as Asymmetric Digital Subscriber Line (ADSL) services, IEEE 802.11a/g, IEEE 802.16a, Digital Audio Broadcast (DAB), Digital Terrestrial Television Broadcast, and DVD in Europe. OFDM is also being considered for 4G, IEEE 802.11n, IEEE 802.15.3a, and IEEE 802.20.

In OFDM communication systems, the orthogonal sub-carriers can ensure that sub-carriers do not interfere with each other, so the internal inter-carrier interference is negligible. Furthermore, the external narrowband interference will affect at most a couple of sub-carriers and information from the affected sub-carriers can be erased and recovered via the forward error correction (FEC). Therefore, OFDM has an inherent robustness against interference. Since cyclic prefix can preserve the orthogonality between sub-carriers, the OFDM receiver can easily capture the signal power from multiple paths.

Generally speaking, two complex signals, $x_1(t)$ and $x_2(t)$, on some time interval $[a, b]$, are defined as orthogonal if and only if they satisfy the following condition [Proa01]

$$\int_a^b x_1(t)x_2^*(t)dt = 0 \quad (2.8)$$

Let's define the symbol rate as f_0 , and symbol period as T . If the frequency of each sub-carrier f_c is multiple times of symbol rate f_0 , i.e., $f_c = nf_0$, then equation (2.9) happens to hold.

$$\int_0^T \cos(2\pi mf_0 t) \times \cos(2\pi nf_0 t) dt = 0 \quad (n \neq m) \quad (2.9)$$

In other words, sub-carriers nf_0 and mf_0 are orthogonal, when n and m are different. The core of OFDM is to take advantage of this good property of orthogonal sub-carriers by using the inverse discrete Fourier transform (IDFT) in the modulator and discrete Fourier transform (DFT) in the demodulator.

In OFDM modulator, there are totally N sub-carriers, among which N_u sub-carriers are active and the rest are inactive. The inactive sub-carriers are set to zero in order to shape the power density spectrum of the transmitted signal. The binary information data are mapped onto the active sub-carriers. The sub-carrier l of the OFDM symbol k is modulated with the complex coefficient $A_{k,l}$. The sub-carrier coefficient vector of symbol k , $\mathbf{A}_k = [A_{k,0}, \dots, A_{k,N-1}]$, is then transformed into time domain using a N -point IDFT, i.e., $\mathbf{a}_k = IDFT[\mathbf{A}_k]$. In the time domain, the coefficient vector \mathbf{a}_k can be calculated following equations (2.10) and (2.11).

$$\mathbf{a}_k = [a_{k,0} \dots a_{k,N-1}] \quad (2.10)$$

$$a_{k,l} = \frac{1}{\sqrt{N}} \sum_{m=0}^{N-1} A_{k,m} e^{j\frac{2\pi}{N}mk} \quad (0 \leq l < N) \quad (2.11)$$

The samples $a_{k,l}$ are transmitted using pulse amplitude modulation. The signal transmitted in time domain is expressed as

$$S(t) = \sum_{k=0}^{\infty} \sum_{l=0}^{N-1} a_{k,l} * w(t - kT_{symbol}) \quad (2.12)$$

The symbol period T_{symbol} is N times sample period T_{sample} , i.e., $T_{symbol} = NT_{sample}$.

Notation $w(t)$ is a rectangular pulse of symbol duration T_{symbol} .

In contrast to conventional frequency shift keying, the spectral overlapping among sub-carriers is allowed in OFDM since orthogonality will ensure the sub-carrier separation in the receiver. This leads to better spectral efficiency of OFDM. Since the use of steep band-pass filter is eliminated, the cost of OFDM system is also reduced. The OFDM symbol period is longer than the propagation channel delay spread, and this results in flat fading channel for each sub-carrier, which can be easily equalized if it is necessary.

The OFDM system also has its own problems. One of them is that the OFDM signal peak to average power ratio (PAPR) may be high in time domain. So the RF amplifier requires big linear dynamic range. Two categories of approaches have been investigated in the current literature to mitigate PAPR problem. The first approach makes use of coding theory to either avoid the data sequence that leads to high PAPR or reduce the appearing probability of the data sequence with high PAPR. For instance, [JoWi94] proposed a block-coding scheme to mitigate PAPR, [LiRi97] uses a m -sequence method to reduce PAPR, and [EeWa96] employs selective scrambling techniques to control the amplitude peaks. The second category of PAPR mitigation approach is to exploit a correcting function to flatten the signal amplitude while the interference caused by the correcting function should be designed to be negligible. Some exemplar correcting functions are clipping and filtering [ONLo95], peak windowing [PaKu97], additive correcting function [MaRo98], and tone reservation [Hwan01].

The second problem of OFDM is that it is sensitive to frequency errors, which are caused by the frequency discrepancy in the transmitter and the receiver. Even a small amount of frequency error in the receiver may fail the orthogonality of the sub-carriers and introduce inter-carrier interference (ICI) to the received signal. A great deal of research has been done to reduce the signal degradation caused by ICI. Frequency domain equalization [AhLe93] minimizes the frequency errors by using certain training signals. ICI self-cancellation scheme [ZhHa96] [Arms99], and cyclic extension of each symbol in time domain [LiSt95] have been proposed to alleviate the frequency error effect in OFDM systems.

Overall, TH-PPM, TH-BPAM, DS-BPAM, and OFDM modulations are commonly used in UWB communication systems. Each UWB modulation type has its own advantages and disadvantages. Which UWB modulation type to choose depends upon the real-world applications.

2.3 Overview of BER Analysis for UWB Systems

Assuming that the total noise approximates a Gaussian distribution, the bit error probability P_e according to GA method is

$$P_e = Q(\sqrt{SNR}) \quad (2.13)$$

where $Q(x)$ is the right-tail probability function of the standard Gaussian distribution, whose mean equals to zero and standard deviation equals to one.

In GA method, the combined multi-user interference to a single receiver is assumed to have the Gaussian distribution. Even though the individual interference from one user is not Gaussian distribution, when the number of users gets higher and higher, the combined multi-user interference will tend to approach to Gaussian distribution according to central limit theorem. In the TH-PPM UWB system, the total noise in the receiver is the sum of thermal noise and multi-user interference. Thermal noise always has a Gaussian distribution due to its physical generation mechanism. If the multi-user interference also has a Gaussian distribution, then the total noise is Gaussian distributed. This is usually a reasonable assumption in most BER analysis and it also simplifies the analysis tremendously. That is why GA method is widely used in engineering practice.

Since GA method usually underestimates the BER for TH-PPM UWB systems, the CF method is considered more accurate especially when the SNR is high and the number of users is low [HuBe04].

Characteristic function (CF) of a random variable, X , is defined as the Fourier transform of its probability density function (pdf). In other words, the CF of random variable X is the expected value of e^{jwx} , which is formulated as equation (2.14).

$$\phi_X(w) = E[e^{jwx}] \quad (2.14)$$

If two random variables, X and Y , are independent, the characteristic function of the sum of the two random variables is the product of the characteristic function of each individual random variable, i.e.,

$$\phi_{X+Y}(w) = \phi_X(w)\phi_Y(w) \quad (2.15)$$

It is worth to notice that the interferences from different users are usually independent and the combined interference CF can be expressed as the product of the CF of each individual interference.

The probability density function of X , $p(x)$, is the inverse Fourier transform of the characteristic function, i.e.,

$$p(x) = \frac{1}{2\pi} \int_{-\infty}^{\infty} e^{-itx} \phi_X(t) dt \quad (2.16)$$

Let X be a Gaussian random variable with mean of μ and variance of σ^2 . The probability density function of X is denoted as $N(\mu, \sigma^2)$. The characteristic function of X is

$$\phi_X(w) = e^{iw\mu - \frac{1}{2}w^2\sigma^2} \quad (2.17)$$

In equation (2.17), notation i is defined as $i = \sqrt{-1}$.

If X is a continuous random variable, the cdf of X is

$$F_X(x) = \frac{1}{2} + \frac{1}{\pi} \int_0^{\infty} \frac{\sin(xw)}{w} \phi_X(w) dw \quad (2.18)$$

The characteristic function of the interference from user k is

$$\phi_{I_k}(w) = E[e^{jwI_k(t)}] \quad (2.19)$$

After some manipulation, equation (2.19) turns out to be

$$\phi_{I_k}(w) = \frac{1}{T} \int_0^T e^{jwI_k(t)} dt \quad (2.20)$$

Notation T is the cyclostationary period of the interference. In the asynchronous UWB multi-user system, the total interference to a single receiver is

$$\phi_I(w) = [\phi_{I_k}(w)]^{(U-1)N_s} \quad (2.21)$$

where U is the number of users, N_s is the number of sequence.

The characteristic function of thermal noise is expressed as

$$\phi_N(w) = e^{-\frac{\sigma_N^2 w^2}{2}} \quad (2.22)$$

The bit error probability, P_e , can be calculated as [HuBe03] [HuBe04].

$$P_e = \frac{1}{2} - \frac{1}{\pi} \int_0^{\infty} \frac{\sin(N_s R(0)w)}{w} \phi_I(w) \phi_N(w) dw \quad (2.23)$$

Table 2.1 Numerical Parameters of TH-PPM System

Parameter	Notation	Value Used
Number of chips	N_h	8
Sequence Length	N_s	3
Number of Users	U	10
Time Factor	τ (s)	0.078125

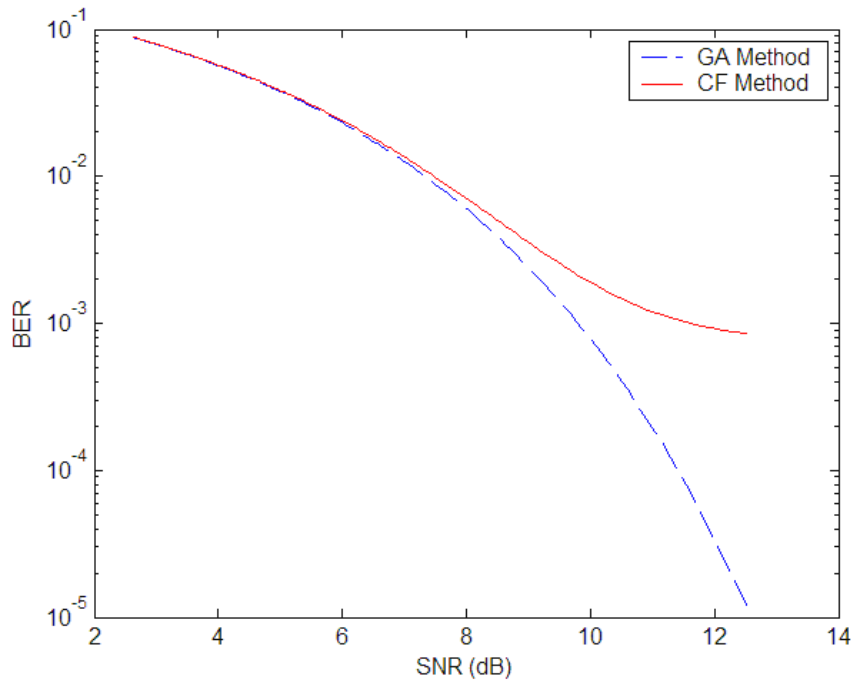


Figure 2.9 BER performance vs. SNR of GA and CF methods

For a TH-PPM UWB system, the BER performances calculated by GA method and CF method are compared in the following simulation example. The parameters for this example are summarized in Table 2.1. The BER curves calculated from the two methods are compared side by side in Figure 2.9.

As shown in Figure 2.9, both GA method and CF method get the same results when SNR is low. However, when SNR is high, the GA method tends to underestimate the BER. In other words, GA method tends to have an over optimistic BER calculation results when SNR is high. This is because that the multiple access interference (MAI) distribution is far apart from Gaussian distribution especially when the SNR is high.

In addition to pulse-based UWB communication systems, MB-OFDM can also be used to build UWB systems. A general base-band equivalent OFDM system model is shown in Figure 2.10.

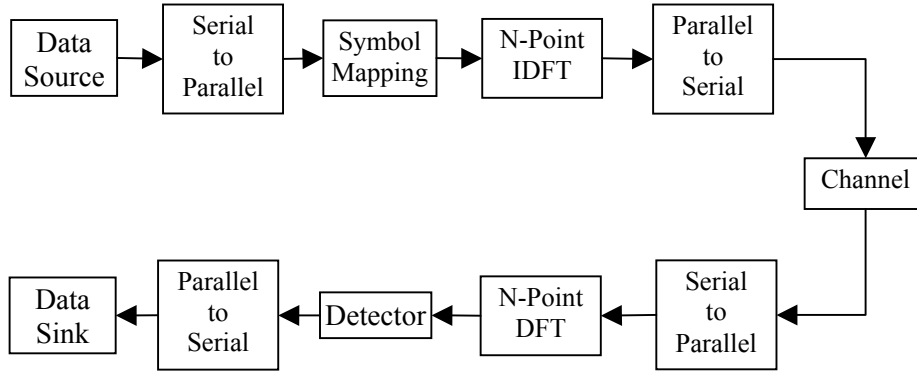


Figure 2.10 Base-band Equivalent OFDM System Model

In UWB OFDM transmitters, information data bits are first changed from serial to parallel, then, the data bits are mapped to symbols. The symbol mapping could be BPSK, QPSK, QAM, etc. A N-point inverse-discrete-Fourier-transform (IDFT) is conducted on the symbol bits. The symbol bits after IDFT are changed from parallel to serial and transmitted. In UWB OFDM receivers, the received symbols are first changed from serial to parallel, then processed with N-point discrete-Fourier-transform (DFT). The DFT output is then fed to detector to make bit decisions. The decided bits are changed from parallel to serial and sent to data sink.

The BER performance analysis usually starts from the output signal from DFT. Let us denote the SNR of the DFT output signal by γ . A general symbol error rate (SER) formula of OFDM systems can be expressed as

$$SER = \int_0^{\infty} P_e(\gamma) p(\gamma) d\gamma \quad (2.24)$$

If one symbol represents k information bits, the overall bit error rate of the OFDM communication system [Proa01] is

$$BER = \frac{2^{k-1}}{2^k - 1} SER \quad (2.25)$$

In equation (2.24), $P_e(\gamma)$ is the symbol error rate of the specific modulation used in symbol mapping. For instance, if the BPSK modulation is used, then the error probability function is $P_e(\gamma) = 0.5\text{erfc}(\sqrt{\gamma})$. Appendix A lists the error probability functions for some other modulation types. The SNR probability distribution function $p(\gamma)$ is determined by communication channel characteristics, transmitter and receiver distortion, receiver channel estimation, synchronization, etc. The OFDM performance in nonlinear AWGN channels are studied in [BaCa00], [CaLe91] and [CaLe91]. The effects of nonlinear distortion and imperfect parameter estimation on OFDM system performance are investigated in [ZhYa04]. The OFDM performance in Rayleigh fading channel is analyzed in [ChSu02].

2.4 Summary

In this chapter, three most often used pulses in UWB literature, Gaussian pulse, Gaussian monocycle, and Gaussian double, are investigated. Some latest solid-state pulse generation technologies are also briefed. Several types of UWB modulation, such as TH-PPM, TH-BPAM, DS-BPAM, and OFDM, are scrutinized. Finally, two BER analysis methods, GA method and CF method, are introduced and compared. It is demonstrated in both theoretic analysis and simulation study that the CF method is more accurate than the GA method is.

3 UWB Channel Modeling and RAKE Receiver

Since UWB signals take ultra wide frequency bandwidth, they can achieve very fine time and range resolution. The capacity and performance of UWB communication systems can also be improved by taking advantage of RAKE receivers, which collect the signals coming from different paths and form a combined signal with better SNR. However, this SNR improvement or UWB communication system performance improvement by RAKE receiver is dependent upon the characteristics of the UWB propagation channel. So the characteristics of UWB propagation channel are very interesting to UWB researchers. Since M -ary orthogonal keying (MOK) and M -ary bi-orthogonal keying (MBOK) signals are often used in UWB PPM systems, the performance analysis of M -ary orthogonal and M -ary bi-orthogonal signals with RAKE receivers under realistic UWB channel environments are of great interest to both practitioners and researchers. This chapter starts with a thorough study of UWB channel modeling. Then a RAKE receiver performance simulation model is proposed, in which instantaneous SNR rather than average SNR is used to represent the instantaneous performance of the RAKE receiver. Finally, the instant MBOK performance is studied.

The average MBOK signal performance is found to be jointly determined by the modulation type, RAKE receiver, and the UWB channel characteristics.

The rest of this chapter is organized as follows. Section 3.1 studies the UWB channel characteristics. Section 3.2 investigates RAKE receivers. Section 3.3 analyzes the performance of MBOK UWB signals with RAKE receiver and under realistic UWB channel environments. Section 3.4 concludes the chapter.

3.1 UWB Channel Model

A considerable amount of research has been conducted in modeling UWB signal propagation channels so far. Some representative models are Intel model [Inte02], Δ -K model [Suzu77], Win-Cassoli model [WiCa01], Chassemzadeh-Greenstein model [ChGr01], Pendergrass-Beeler model, [PeBe01], ray-tracing models, and so on.

[LeHa00] first employs a two-ray model for characterizing the fading of UWB propagation channels. Later on [YaGo03] applies the time domain uniform theory of diffraction (UTD) into UWB channel analysis. This method opens a ground for applying traditional ray-tracing method into UWB signal attenuation and distortion calculation. The advantages of ray-tracing model in developing site-specific channel predictions were demonstrated in [SeRa94], [LaMc94], and [FeRa93]. [JaBo96] and [ChDo99] also investigated UWB diffraction in the presence of buried object. [SiBe03], [SiPe01] and [SiMc04] described a median UWB multi-path propagation model which is based on free space propagation and shadowing variation. [PrCh02] analyzed the spatial correlation of the UWB signal when the receiver is moving inside a residential environment and found out that spatial correlation is present within a range of 0.05-0.15m for both LOS and NLOS channel environments.

In Win-Cassoli model [WiCa01], the magnitude of multi-paths is modeled as a Nakagami-m distribution. Since Nakagami-m distribution has one more degree of freedom than Rayleigh distribution, it fits measurement data better than Rayleigh distribution does. Even though the measurement data used in [WiCa01] were collected in the frequency range from 1.5 GHz to 3 GHz, this model shed some lights into UWB channel characteristics.

Δ -K model was first proposed in [Suzu77], its goodness of fit to empirical indoor propagation data was reported in [Hash93]. In this model, multi-paths are grouped into bins of width Δ . The probability of having a path in bin l is defined as P_l . If there is a path in the $(l-1)$ th bin, then the probability of having a path in the current bin l is $P_l = K\lambda_l$. Otherwise, $P_l = \lambda_l$. The empirical bin occupancy rate of bin l is defined as r_l .

Notation λ_l is given by $\lambda_1 = r_1$ and $\lambda_l = \frac{r_l}{(K-1)r_{l-1} + 1}$. If $K > 1$, the multi-paths tend to

arrive in clusters. If $K < 1$, the multi-paths tend to be spread out evenly. The path amplitude is modeled as a lognormal distribution with an exponentially decaying multi-path intensity profile. Since it only has one exponential decaying slope, this model can't fit mean excess delay and rms delay of UWB experimental data simultaneously. In later research, [ZhWu02] suggested a combination of a two-state Markov model and the Δ -K model for estimating the arrival of the multi-path components, and a Gamma distribution for assessing the signal power of each ray. By increasing the model's freedom as well as the complexity, the goodness of fit of empirical data to the analytical model is certainly incrementing.

The Intel model [FoLi02] originates from the Saleh-Valenzuela model [SaVa87] and the only difference between the two is that the Intel model uses a lognormal distribution rather than Rayleigh distribution to template the multi-path gain distribution. In the Intel model, the arrival rays are grouped into clusters, and in each cluster all the rays share both the arrival time distribution and the amplitude distribution. There are two Poisson

distributions in this model. The first one is used to model the arrival time of the clusters and the second one is used to delineate the arrival time of the rays in each cluster. The gain magnitude of each individual is modeled as a lognormal distribution. Following the paradigm of Intel and Saleh-Valenzuela models, the Intel model can be organized into two parts: (1) multi-path free channel loss model and (2) ray amplitude and arrival model.

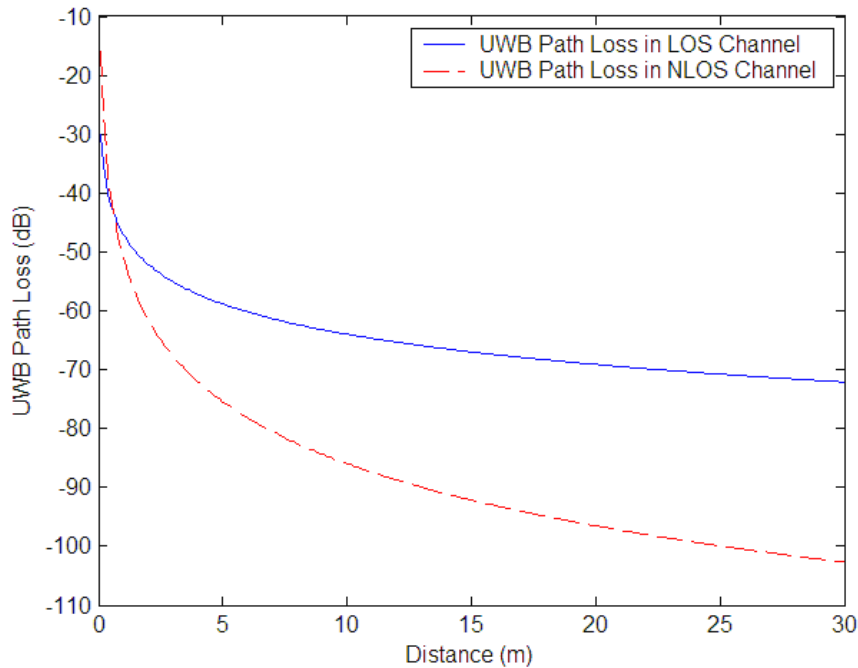


Figure 3.1 UWB Path Loss vs. Distance in LOS and NLOS Channels

In the multi-path free UWB path loss model, the overall UWB signal path loss, PL , can be expressed as

$$PL = A_{1m} - 10 * n * \log(D) \quad (3.1)$$

Notation A_{1m} is a reference path loss at 1 meter reference distance. Notation n is a constant exponent of power loss. It is 2 for free space propagation, greater than 2 for non-line of sight (NLOS) channel, and less than 2 for line of sight (LOS) over short distance [GhTa03]. Notation D denotes the distance between transmitter and receiver. According

to [BeGi04], A_{1m} is equal to -47dB and n is set to 1.7 for short range LOS UWB channels. For NLOS UWB channels, A_{1m} is equal to -51dB and n is equal to 3.5. The UWB Path Loss vs. Distance in LOS and NLOS Channels is shown in Figure 3.1.

In the UWB ray amplitude and arrival model, the UWB channel paths or rays, $h(t)$, is modeled as:

$$h(t) = \sum_{l=1}^L \sum_{k=1}^{K_l} p_{k,l} \beta_{k,l} \delta(t - T_l - \tau_{k,l}) \quad (3.2)$$

Notation L is the number of clusters, and K_l is the number of rays inside the l -th cluster. The sign determinant $p_{k,l}$ can only be taken from two equally probable nominal values, i.e., 1 or -1. The magnitude gain of each ray $\beta_{k,l}$ has a lognormal distribution, which can be described in equation (3.3).

$$20 \log(|\beta_{k,l}|) \propto \text{Normal}(\mu_l, \sigma^2) \quad (3.3)$$

The expectation of the squared value of $\beta_{k,l}$ can be expressed as

$$E[\beta_{k,l}^2] = \Omega_0 e^{-T_l/\Gamma} e^{-\tau_{k,l}/\gamma} \quad (3.4)$$

In equation (3.4), notation Ω_0 is the mean power of the first ray of the first cluster, Γ is the cluster decay factor, and γ is the ray decay factor. The mean value μ_l can then be calculated as

$$\mu_l = \frac{10 \ln(\Omega_0) - 10T_l/\Gamma - 10\tau_{k,l}/\gamma - \sigma^2 \ln(10)}{\ln(10)} \quad (3.5)$$

In equation (3.5), notation T_l is the first ray arrival time in the l -th cluster, and $\tau_{k,l}$ is the delay of the k -th ray within the l -th cluster relative to the first ray arrival time. Both T_l and $\tau_{k,l}$ have Poisson distributions which are described in equations (3.6) and (3.7).

$$p(T_l) = \lambda_c \exp(-\lambda_c T_l) \quad (3.6)$$

$$p(\tau_{k,l}) = \lambda_r \exp(-\lambda_r \tau_{k,l}) \quad (3.7)$$

Notation λ_c is the cluster arrival rate, and λ_r is the ray arrival rate within each cluster.

In IEEE 802.25.3a working group, the UWB channel is further classified into four models. Channel model 1 (CM1) represents LOS and distance from 0 to 4 m UWB channel, while channel model 2 (CM2) represents NLOS and distance from 0 to 4 m UWB channel. Distance from 4 m to 10 m and NLOS UWB channel is modeled as CM3 and distance over 10 m NLOS UWB channels are all classified into the extreme model CM4. The simulation parameter settings for all the four channel models are listed in Table 3.1.

Table 3.1 Parameter Settings for IEEE UWB Channel Models [BeGi04]

Scenario	Λ (1/ns)	λ (1/ns)	Γ (1/ns)	γ (1/ns)	σ_ξ (dB)	σ_ζ (dB)	σ_g (dB)
CM 1 LOS (0-4m)	0.0233	2.5	7.1	4.3	3.3941	3.3941	3
CM 2 NLOS (0-4m)	0.4	0.5	5.5	6.7	3.3941	3.3941	3
CM 3 NLOS (4-10m)	0.0667	2.1	14	7.9	3.3941	3.3941	3
CM 4 Extreme NLOS	0.0667	2.1	24	12	3.3941	3.3941	3

With the exact channel parameters listed in Table 3.1, the UWB channels for all the four channel scenarios are simulated using the Intel UWB channel model. The simulated channel impulse responses for CM1, CM2, CM3, and CM4 are shown in Figure 3.2, 3.4, 3.6, and 3.8 respectively. The power delay profiles for CM1, CM2, CM3, and CM4 are plotted in Figure 3.3, 3.5, 3.7, and 3.9 respectively.

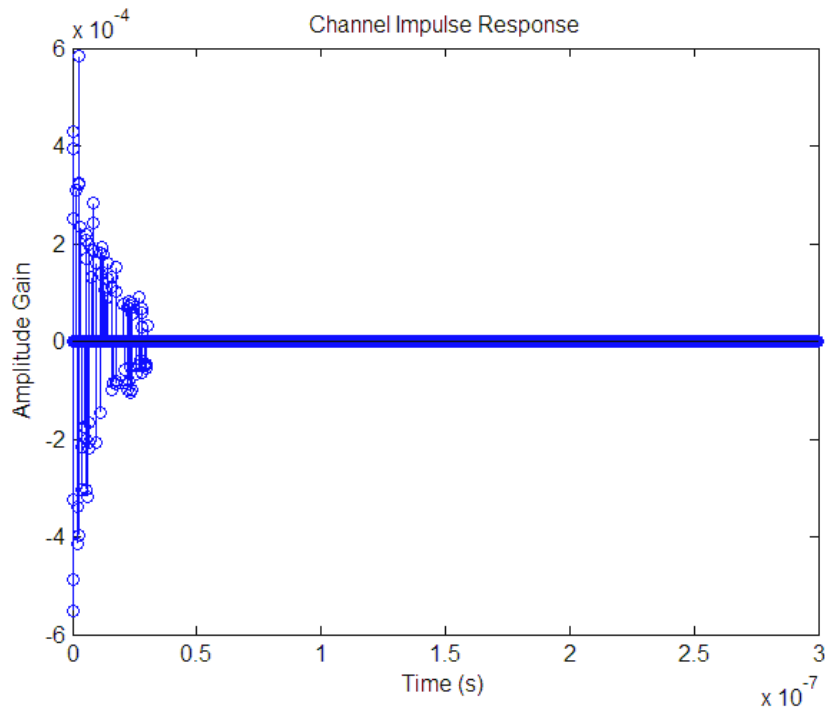


Figure 3.2 Impulse Response of CM1 Channel

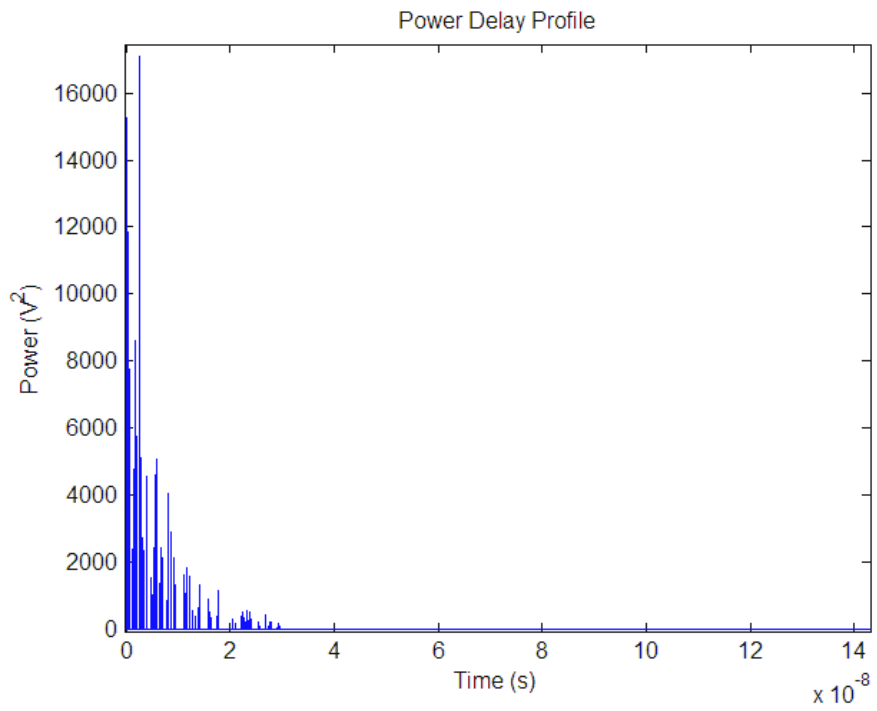


Figure 3.3 Delay Profile of CM1 Channel

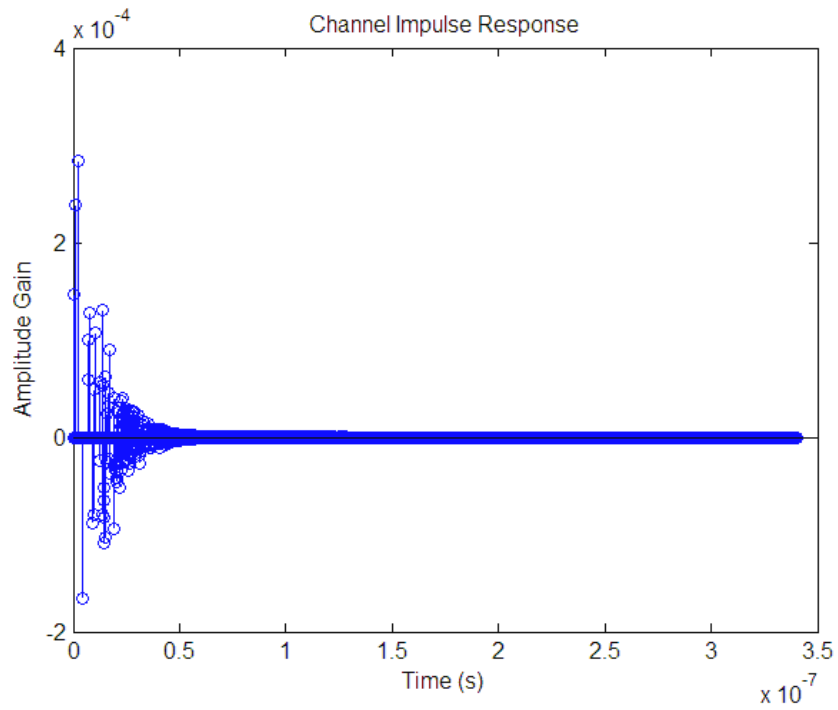


Figure 3.4 Impulse Response of CM2 Channel

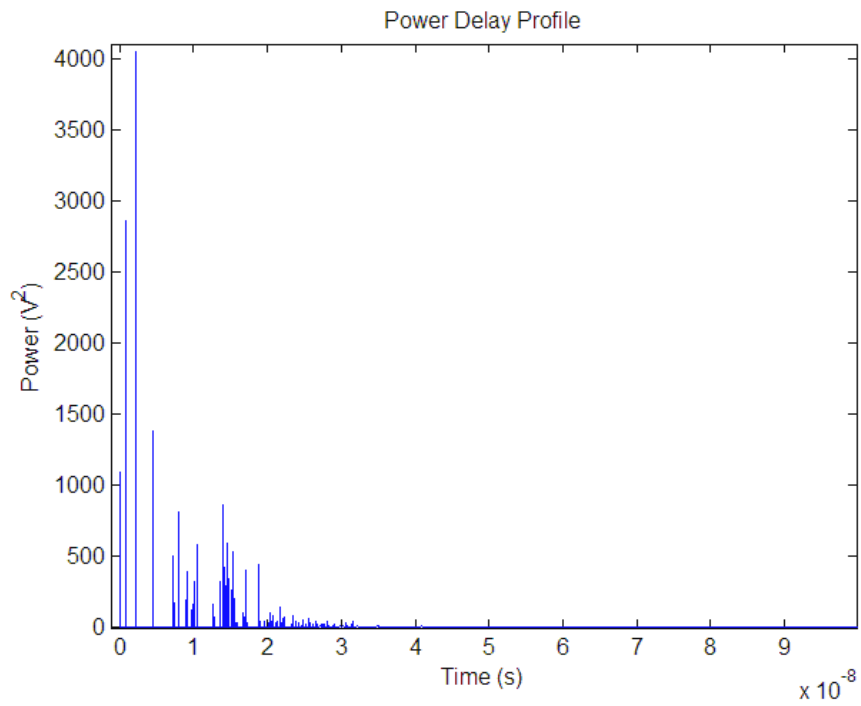


Figure 3.5 Delay Profile of CM2 Channel

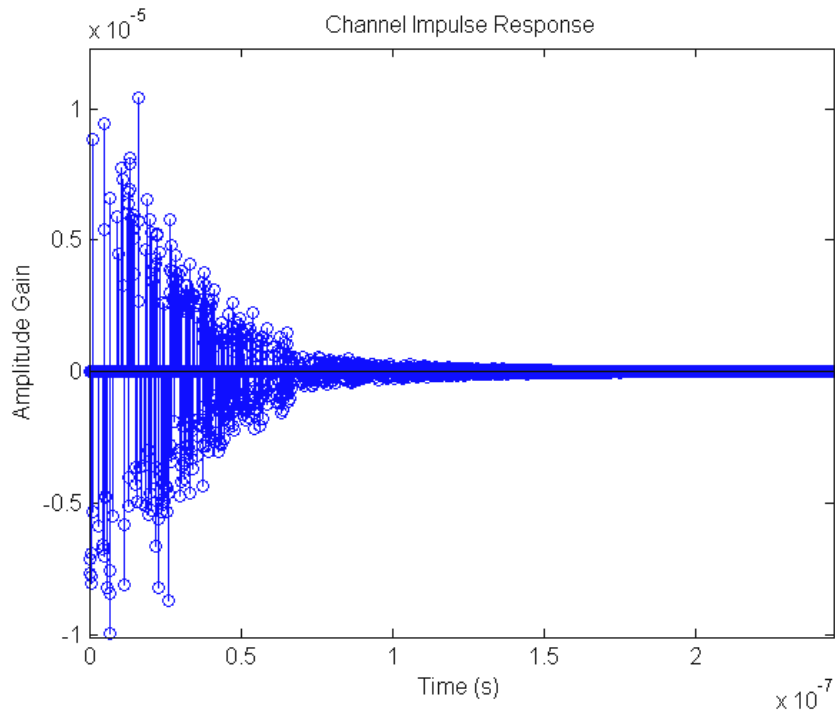


Figure 3.6 Impulse Response of CM3 Channel

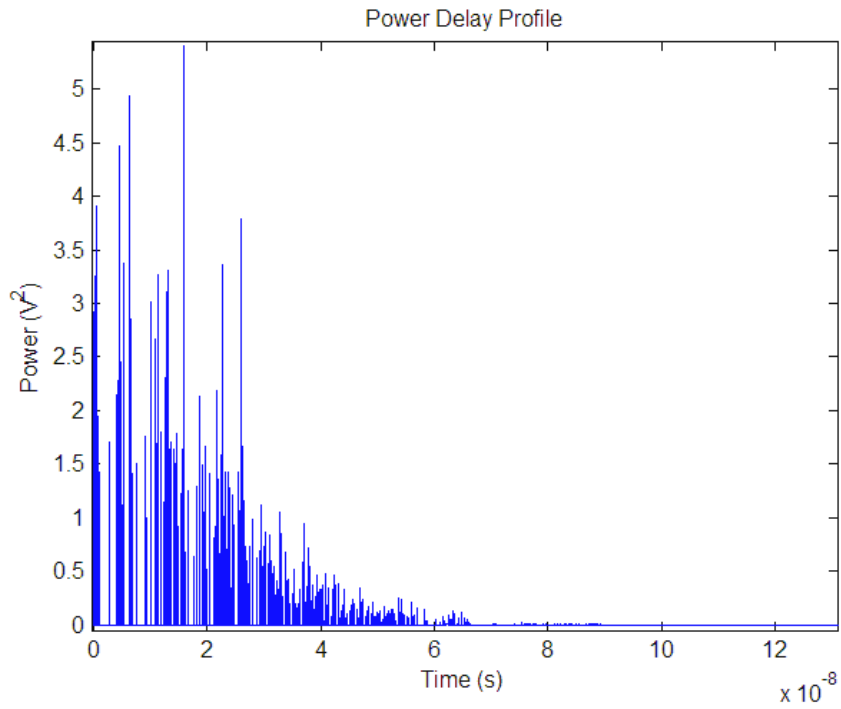


Figure 3.7 Delay Profile of CM3 Channel

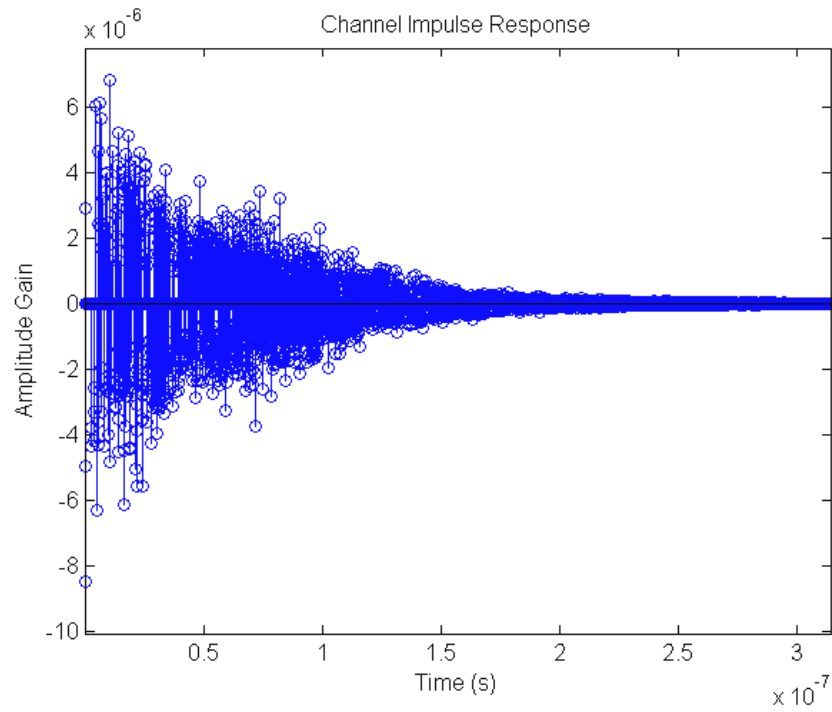


Figure 3.8 Impulse Response of CM4 Channel

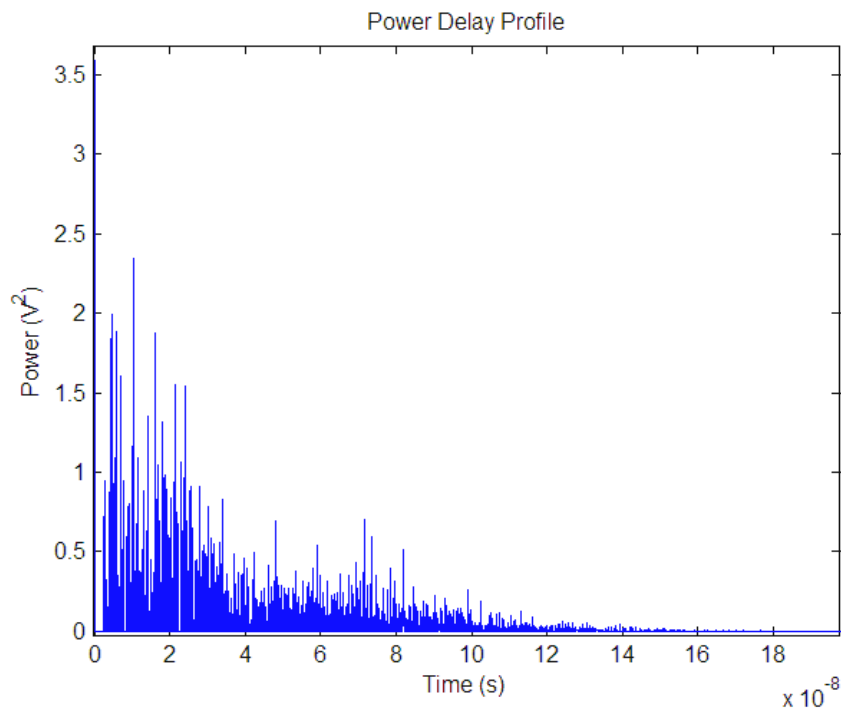


Figure 3.9 Delay Profile of CM4 Channel

The time dispersion of UWB channels can be quantified by their mean excess delay time and rms (root mean square) delay spread [Rapp02]. The mean excess delay is the first moment of the power delay profile and can be defined as

$$\bar{\tau} = \frac{\sum_k h_k^2 \tau_k}{\sum_k h_k^2} \quad (3.8)$$

The rms delay spread σ_τ is defined as the square root of the second central moment of the power delay profile, i.e.,

$$\sigma_\tau = \sqrt{\tau^2 - \bar{\tau}^2} \quad (3.9)$$

where

$$\tau^2 = \frac{\sum_k h_k^2 \tau_k^2}{\sum_k h_k^2} \quad (3.10)$$

If the coherence bandwidth is the bandwidth over which the frequency correlation function is above 0.5, then the coherence bandwidth is approximately [Rapp02]

$$B_c \approx \frac{1}{5\sigma_\tau} \quad (3.11)$$

As listed in Table 3.2, the coherence bandwidths of CM1, CM2, CM3, and CM4 simulation are 27 MHz, 26 MHz, 10.6 MHz, and 5.9 MHz respectively.

Table 3.2 Coherence Bandwidth of UWB Channels

	CM 1	CM 2	CM 3	CM 4
Mean Excess Delay $\bar{\tau}$ (ns)	7.4	7.7	18.9	34
Delay Spread σ_τ (ns)	7	7.3	17	28
Coherence Bandwidth B_c (MHz)	27	26	10.6	5.9

If the symbol rate is less than the channel coherence bandwidth, the inter-symbol interference (ISI) won't be a problem for the communication system. However, when the symbol rate is above the channel coherence bandwidth, signals of multi-paths will

cause ISI at receivers. The highest UWB coherence bandwidth, which is about 27 MHz, is far less than the expected UWB symbol rates, which are usually above hundreds of mega hertz. Therefore, ISI issues will be persistent with UWB communications. Similar results have also been found in [SiBe03].

3.2 RAKE Receivers

RAKE receivers, which were first proposed in [PrGr58], use the tapped delay line structure to collect the signal energy from all the received signal paths within the span of the delay line. According to ways of combining, RAKE receivers can be categorized into either equal gain combining (EGC) RAKE receivers or maximal ratio combining (MRC) RAKE receivers. Equal gain combiner simply sums up signal from all multipaths, i.e., the RAKE receiver taps are all equal to unit. On the other hand, in maximal gain combiner, the RAKE receiver tap weights are chosen to be the complex conjugate of the channel gain, i.e., the channel phase shift is compensated and the signal is enhanced by a factor that is proportional to the signal strength [Bren59]. If the channel attenuation and phase shift can be perfectly estimated or known, maximal ratio combiner is the optimal combiner [Proa03].

According to ways of selection, RAKE receivers can also be categorized into either selective combiners or non-selective combiners. In selective combiners, only the L strongest paths out of the total N ($N > L$) paths are combined. In non-selective combiners, all N received paths are combined together.

For maximal ratio gain combiner, the combined signal SNR [Proa03] γ can be expressed as

$$\gamma = \frac{E_p}{N_0} \sum_{k=1}^L h_k^2 \quad (3.12)$$

The SNR of individual path γ_k is

$$\gamma_k = \frac{E_p}{N_0} h_k^2 \quad (3.13)$$

The combined SNR from multiple paths equals to the sum of SNR from each individual path, i.e.,

$$\gamma = \sum_{k=1}^L \gamma_k \quad (3.14)$$

If the symbol error rate for a certain type of modulation is denoted as $P_s(\gamma)$, the average symbol error rate P_{avg} using RAKE receiver is the expected value of $P_s(\gamma)$, i.e.,

$$P_{avg} = \int_0^{\infty} P_s(\gamma) p(\gamma) d\gamma \quad (3.15)$$

The symbol error rate formulas for commonly used modulation types are summarized in Appendix A. The probability distribution of a SNR value out of a RAKE receiver is related to the characteristics of the propagation channel. For Rayleigh channel model, the probability distribution function of the SNR from each individual path is

$$p(\gamma_k) = \frac{1}{\bar{\gamma}_k} \exp\left(\frac{-\gamma_k}{\bar{\gamma}_k}\right) \quad (3.16)$$

Notation $\bar{\gamma}_k$ is the mean SNR over all channel paths, i.e.,

$$\bar{\gamma}_k = \frac{E_p}{N_0} E(h_k^2) \quad (3.17)$$

The characteristic function of individual path SNR γ_k is

$$\psi_{\gamma_k}(j\omega) = \frac{1}{1 - j\omega\bar{\gamma}_k} \quad (3.18)$$

The characteristic function of the combined SNR γ out of RAKE receiver can be calculated as

$$\psi_{\gamma}(j\omega) = \prod_{k=1}^L \frac{1}{1 - j\omega\bar{\gamma}_k} \quad (3.19)$$

Taking the inverse Fourier transform of the characteristic function of γ , the probability density function of γ is derived as

$$p(\gamma) = \frac{1}{(L-1)! \bar{\gamma}_k^L} \gamma^{L-1} \exp\left(\frac{-\gamma}{\bar{\gamma}_k}\right) \quad (3.20)$$

For BPSK modulation, the symbol error probability is

$$P_s(\gamma) = Q(\sqrt{2\gamma}) \quad (3.21)$$

Substituting equations (3.20) and (3.21) into equation (3.15), the average BPSK symbol error using RAKE receiver under Rayleigh fading channel [Proa03] is

$$P_{avg} = \left[\frac{1}{2}(1-\mu) \right]^L \sum_{k=0}^{L-1} \binom{L-1+k}{k} \left[\frac{1}{2}(1+\mu) \right]^k \quad (3.22)$$

where by definition

$$\mu = \sqrt{\frac{\bar{\gamma}_k}{1+\bar{\gamma}_k}} \quad (3.23)$$

For equal gain combiner (EGC) RAKE receivers, the combined signal SNR out of the RAKE receiver is

$$\gamma = \frac{E_p}{LN_0} \left(\sum_{k=1}^L h_k \right)^2 \quad (3.24)$$

The average symbol error probability using EGC RAKE receiver can be hardly calculated with equation (3.15) since the probability distribution of $\sqrt{\gamma}$ is extremely difficult to derive if it exists at all. [AnTe00] and [Zhan97] demonstrated that closed form solutions of the average symbol error probability can be derived with the characteristic functions of the channel models such as Rayleigh, Rician, Nakagami-q, and Nakagami-m channels. Even though the derivation of close-form solutions is quite clumsy. The main idea of this kind of method is to project the probability density function domain into the characteristic function domain, coincidentally the calculation in characteristic function domain may be easier to accomplish, and then project the results back into probability domain. For instance, if the square root of the SNR out of RAKE

receiver is denoted by x , and $x = \sqrt{\gamma}$, the average SER of EGC RAKE receiver can be calculated as

$$P_{avg} = \frac{1}{2\pi} \int_0^{\infty} FT[P_s(x)]\psi_x^*(w)dw \quad (3.25)$$

Notation $\psi_x^*(\cdot)$ denotes the complex conjugate of the characteristic function of x . $FT[\cdot]$ denotes Fourier transform, which is consistent with the definition of characteristic function.

[WiWi01] proposed a virtual branch analysis method for hybrid selective/maximal ratio combining in Rayleigh fading channel. This method doesn't make Gaussian assumption but can only have solutions to relatively simple channel model such as Rayleigh, Ricean, and Nakagami channels [WiMa02]. For a channel model as complicated as UWB realistic channel, the derivation of symbol error probability using this method is also extremely complicated. Furthermore, this method left no room for considering inter-symbol interference caused by RAKE receiver.

For the realistic UWB channel model, the derivation of close-form average SER for either MRG or EGC RAKE receiver will be difficult no matter with probability distribution function domain method, or characteristic function domain method, or virtual branch method. A practical way to assess the performance of a RAKE receiver will be through simulation [RaSo03]. The transmitted UWB signal can be generally expressed as

$$s(t) = \sqrt{E_p} \sum_{m=-\infty}^{\infty} b_m g(t - mT_c) \quad (3.26)$$

Notation b_m denotes the bi-polar information symbols, and $g(t)$ is the normalized UWB pulse function in time domain. The received signal under multi-user and a realistic UWB channel can be generally expressed as

$$r(t) = \sqrt{E_p} \sum_{m=-\infty}^{\infty} b_m \sum_{k=0}^{K-1} h_k g(t - \tau_k - mT_c) + \sqrt{E_p} \sum_{i=1}^{N_u} b_i \sum_{k=0}^{K-1} H_k g(t - \tau_i) + n(t) \quad (3.27)$$

Let's assume the 0-th symbol is the target symbol for detection, the k -th path of the received signal corresponding to the target symbol is

$$y_k = \sqrt{E_p} b_0 h_k + \sqrt{E_p} \sum_{\substack{m=-\infty \\ m \neq 0}}^{\infty} b_m h_{k-mN} + \sqrt{E_p} \sum_{i=1}^{N_u} b_i \sum_{k=0}^{K-1} \mathbf{H}_k g(t - \tau_i) + n_{0,k} \quad (3.28)$$

The output of the RAKE receiver is

$$r_0 = \mathbf{c}^T \mathbf{y} \quad (3.29)$$

The RAKE coefficient vector is $\mathbf{c}^T = [c_0, c_1, \dots, c_{K-1}]$. After some manipulation, the RAKE receiver output turns out to be

$$r_0 = \sqrt{E_p} b_0 \mathbf{c}^T \mathbf{h} + \sqrt{E_p} \sum_{\substack{m=-Q \\ m \neq 0}}^F b_m \mathbf{c}^T \mathbf{h}^{-m} + \sqrt{E_p} \sum_{i=1}^{N_u} b_i \mathbf{c}^T \mathbf{H} + \mathbf{c}^T \mathbf{n} \quad (3.30)$$

The received instantaneous signal power is

$$Sig = E_p [(\mathbf{c}^T \mathbf{h}^0)^2] \quad (3.31)$$

The received instantaneous noise power is

$$Noise = \sum_{i=0}^{K-1} c_i^2 \frac{n_0}{2} \quad (3.32)$$

The received instantaneous ISI power is

$$ISI = E_p \left[\left(\sum_{\substack{m=-Q \\ m \neq 0}}^F b_m \mathbf{c}^T \mathbf{h}^{-m} \right)^2 \right] \quad (3.33)$$

The received instantaneous MAI (Multiple Access Interference) power is

$$MAI = E_p \left[\left(\sum_{i=1}^{N_u} b_i \mathbf{c}^T \mathbf{H} \right)^2 \right] \quad (3.34)$$

The overall received instantaneous signal-to-interference-and-noise (SINR) is

$$\gamma = SINR = \frac{Sig}{ISI + MAI + Noise} \quad (3.35)$$

If the number of simultaneously active users is large and the path losses of users other than the target user are relatively high, the MAI can be assumed to be similar to white Gaussian noise according to the central limit theorem.

3.3 Performance of M -ary Bi-Orthogonal Keying (MBOK) and M -ary Orthogonal Keying (MOK) UWB Signals with RAKE receiver

Let's denote a M -ary orthogonal keying (MOK) signal vector set as $\{\mathbf{s}_m\}$, and the transmitted symbol energy as E_s . For equal energy and equally probable orthogonal signals, the optimal detector selects the signal with the largest cross correlation between the received vector \mathbf{r} and the signal vectors $\{\mathbf{s}_m\}$.

The received signal vector \mathbf{r} is

$$\mathbf{r} = [\sqrt{E_s} + n_1, n_2, \dots, n_M] \quad (3.36)$$

Notations, n_1, n_2, \dots, n_m , are mutually independent m -dimension white Gaussian noises with double side noise density $\frac{1}{2}N_0$.

Correlating the received signal vector \mathbf{r} with each signal vector \mathbf{s}_m , we get

$$\text{corr}(\mathbf{r}, \mathbf{s}_1) = \sqrt{E_s}(\sqrt{E_s} + n_1) \quad (3.37)$$

$$\text{corr}(\mathbf{r}, \mathbf{s}_m) = \sqrt{E_s}n_m \quad m = 2, \dots, M \quad (3.38)$$

The probability density function (PDF) for the first correlator is

$$P_1(x) = \frac{1}{\sqrt{\pi N_0}} \exp\left[-\frac{(x - \sqrt{E_s})^2}{N_0}\right] = \frac{1}{\sqrt{2\pi}} \exp\left[-\frac{\left(x - \sqrt{\frac{2E_s}{N_0}}\right)^2}{2}\right] \quad (3.39)$$

The PDF for the rest correlators are

$$P_m(x) = \frac{1}{\sqrt{\pi N_0}} \exp\left[-\frac{x^2}{N_0}\right] \quad m = 2, \dots, M \quad (3.40)$$

The probability of a correct decision of MOK signal [Proa01] is

$$P_{c_mok} = \frac{1}{\sqrt{2\pi}} \int_{-\infty}^{\infty} \left[\frac{1}{\sqrt{2\pi}} \int_{-\infty}^{\sqrt{2E_s/N_0}} \exp(-x^2/2) dx \right]^{M-1} \exp\left[-\frac{1}{2} \left(y - \sqrt{\frac{2E_s}{N_0}} \right)^2\right] dy \quad (3.41)$$

On the other hand, for M -ary bi-orthogonal keying (MBOK) signals, the received signal vector is

$$\mathbf{r} = [\sqrt{E_s} + n_1, n_2, \dots, n_{M/2}] \quad (3.42)$$

The sign of the correlation output is used to decide whether \mathbf{s}_m or $-\mathbf{s}_m$ was transmitted. According to the optimal decision rule, the probability of correct decision of MBOK signals [Proa01] is

$$P_{c_mbok} = \frac{1}{\sqrt{2\pi}} \int_{-\sqrt{2E_s/N_0}}^{\infty} \left(\frac{1}{\sqrt{2\pi}} \int_{-(v+\sqrt{2E_s/N_0})}^{v+\sqrt{2E_s/N_0}} \exp(-x^2/2) dx \right)^{M/2-1} \exp(-v^2/2) dv \quad (3.43)$$

For both MOK and MBOK signals, the probability of symbol error, P_s , is

$$P_s = 1 - P_c \quad (3.44)$$

The number of binary bits which are needed to represent a M -ary signal, is denoted by k , and $k = \log_2 M$. The probability of bit error P_b is

$$P_b = \frac{2^{k-1}}{2^k - 1} P_s \quad (3.45)$$

If the a MBOK signal consists of N_p pulses, the received symbol signal to noise ratio will be N_p times the received pulse signal to noise ratio, i.e., $\frac{E_s}{N_0} = N_p \gamma$. The

instantaneous SER of MOK UWB signals is

$$P_{s_mok}(\gamma) = 1 - \frac{1}{\sqrt{2\pi}} \int_{-\infty}^{\infty} \left[\frac{1}{\sqrt{2\pi}} \int_{-\infty}^{\sqrt{2N_p\gamma}} \exp(-x^2/2) dx \right]^{M-1} \exp\left[-\frac{1}{2} \left(y - \sqrt{2N_p\gamma} \right)^2\right] dy \quad (3.46)$$

By the same logic, the instantaneous SER of MOK UWB signals is

$$P_{s_mbok} = 1 - \frac{1}{\sqrt{2\pi}} \int_{-\sqrt{2N_p\gamma}}^{\infty} \left(\frac{1}{\sqrt{2\pi}} \int_{-(v+\sqrt{2N_p\gamma})}^{v+\sqrt{2N_p\gamma}} \exp(-x^2/2) dx \right)^{M/2-1} \exp(-v^2/2) dv \quad (3.47)$$

For both MOK and MBOK signals, the average SER of UWB signal using a RAKE receiver is the expected value of the instantaneous SER, i.e.,

$$P_{avg} = \int_0^{\infty} P_s(\gamma) p(\gamma) d\gamma \quad (3.48)$$

The average bit error rate (BER) is calculated as

$$P_b = \frac{2^{k-1}}{2^k - 1} P_{avg} \quad (3.49)$$

For the realistic UWB channel, the path power distribution is hard to derive, and the close-form solution of the average symbol error rate is extremely difficult to get.

Simulation approach is relatively easy and widely used in UWB performance evaluation. In the following MBOK UWB performance simulation, the Intel channel model is employed. When the number of the RAKE taps is fixed to 20, the MBOK performances of different M values with MRC RAKE receivers are compared in Figure 3.10. As M increases, the BER performance gets better. The MBOK performances of different M values with EGC RAKE receivers are demonstrated in Figure 3.11. Though the BER performance gets better as M increases, the MBOK performance with EGC RAKE receiver is noticeably worse than the MBOK performance with MRC RAKE receiver. This is because that MRC RAKE can achieve the best instantaneous SNR while EGC RAKE sacrifices its combined SNR for computation simplicity.

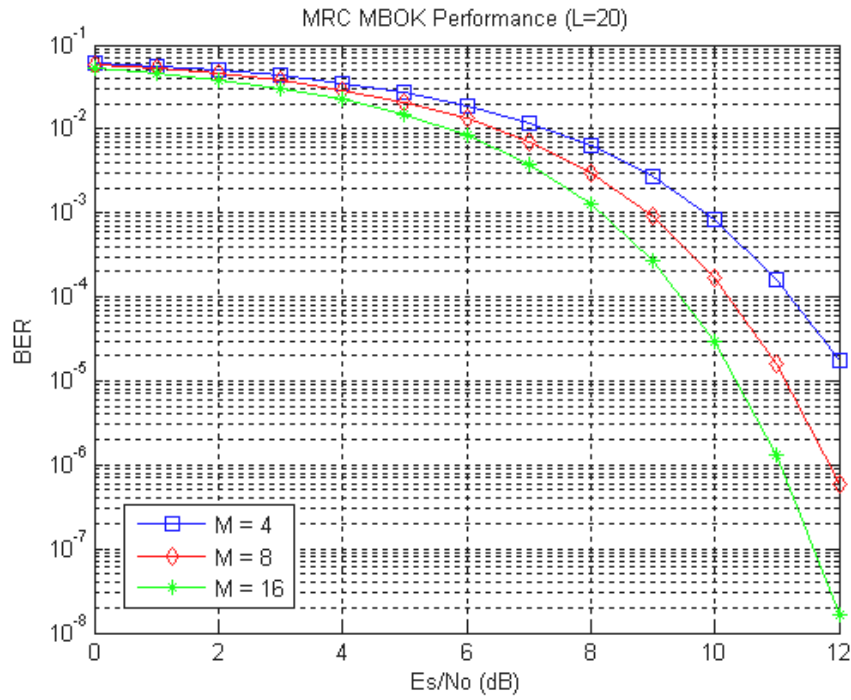


Figure 3.10 MBOK Performances in MRC RAKE Receivers with Different M Values

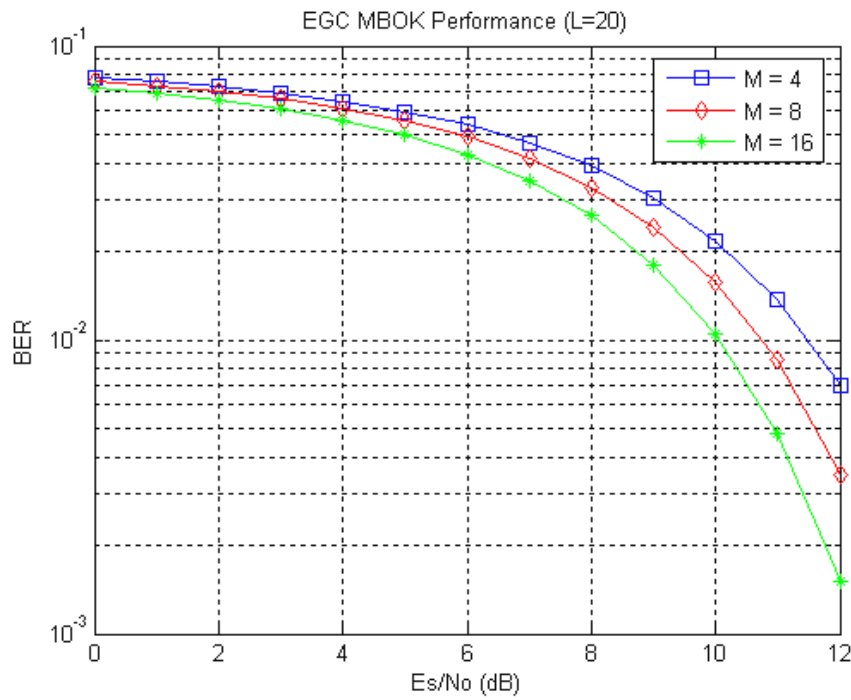


Figure 3.11 MBOK Performances in EGC RAKE Receivers with Different M Values

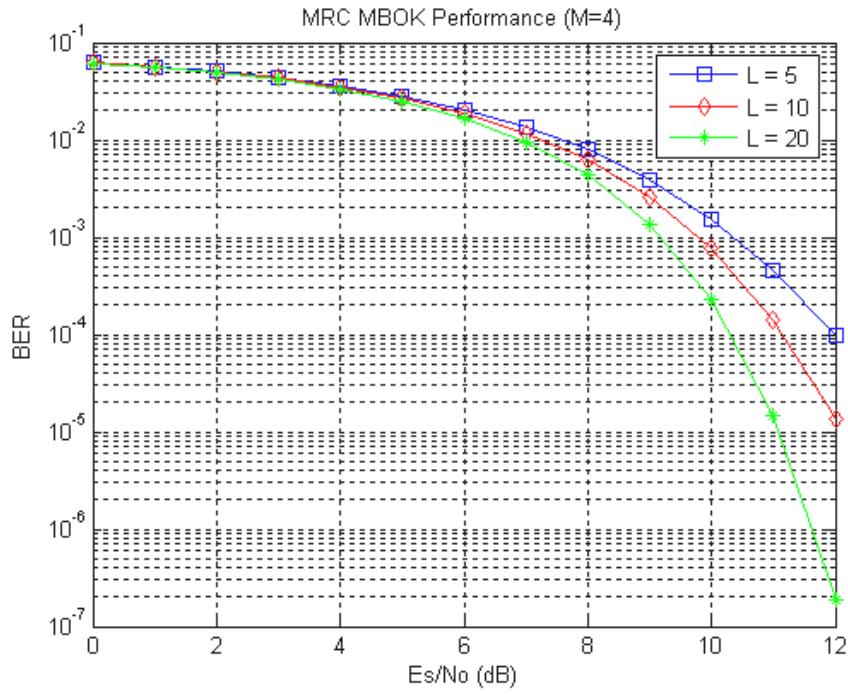


Figure 3.12 MBOK Performances in MRC RAKE Receivers with Different L

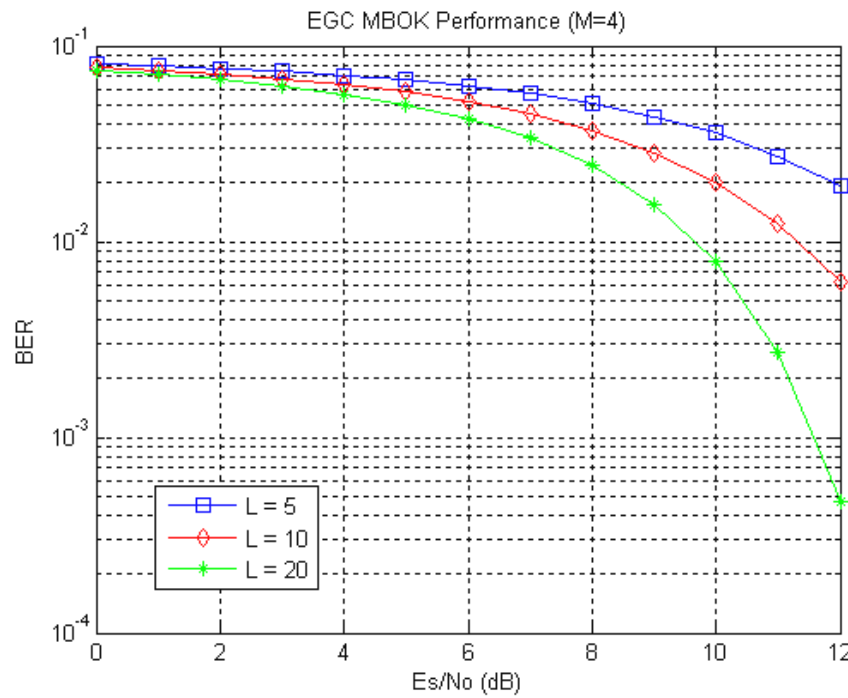


Figure 3.13 MBOK Performances in EGC RAKE Receivers with Different L

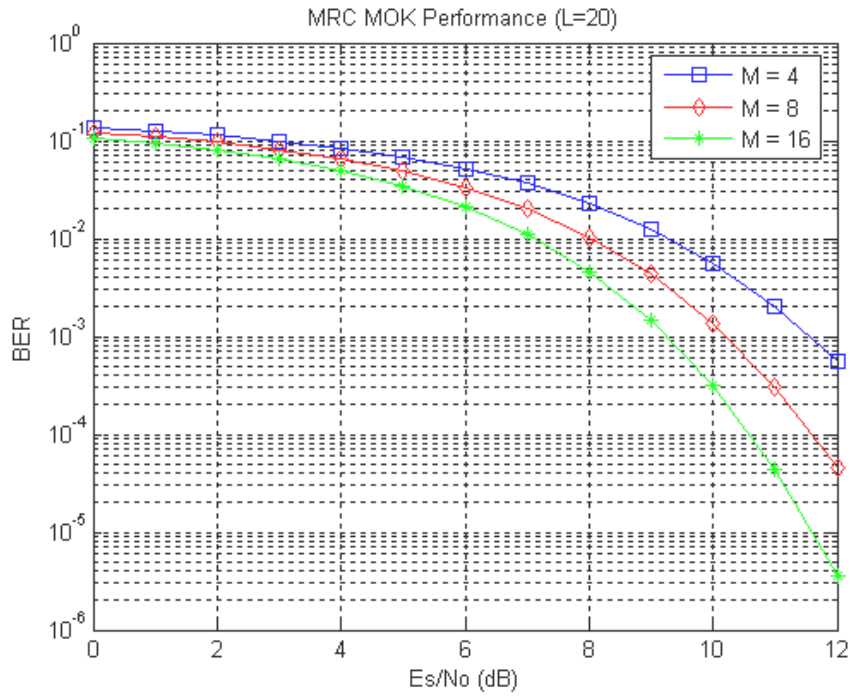


Figure 3.14 MOK Performances in MRC RAKE Receivers with Different M Values

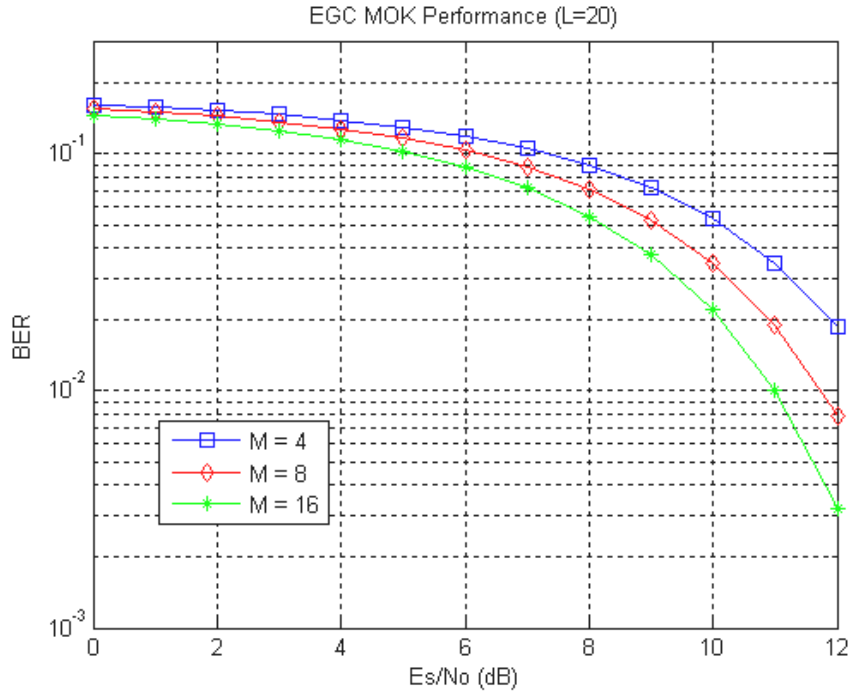


Figure 3.15 MOK Performances in EGC RAKE Receivers with Different M Values

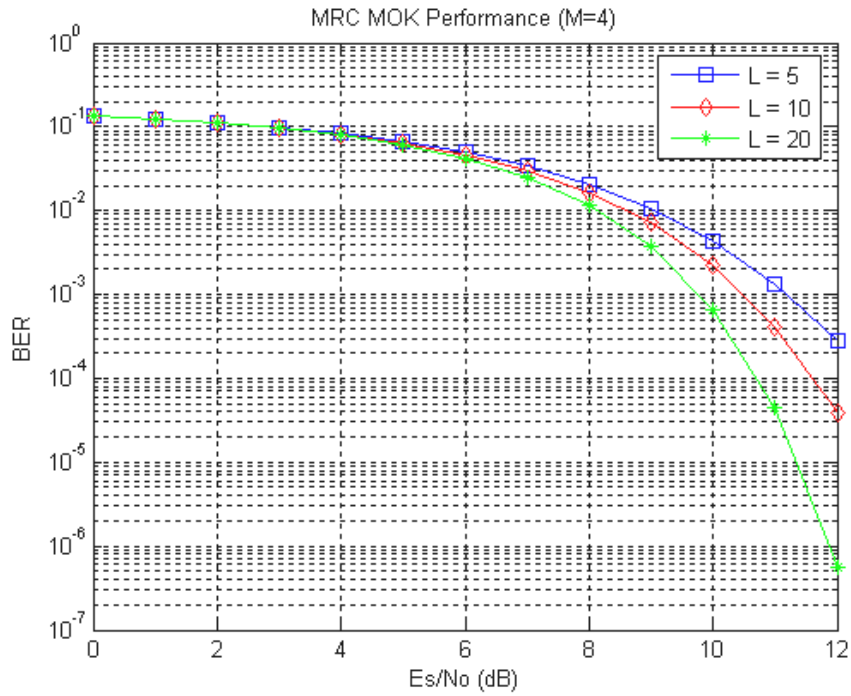


Figure 3.16 MOK Performances in MRC RAKE Receivers with Different L

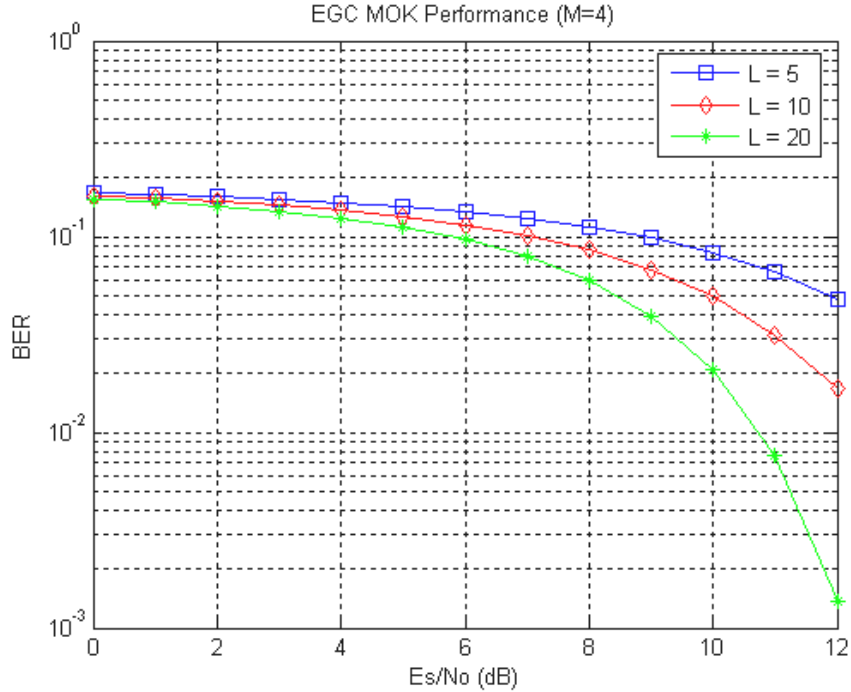


Figure 3.17 MOK Performances in EGC RAKE Receivers with Different L

When the value of M is fixed to 4, the MBOK performances of MRC RAKE and EGC RAKE receivers with different number of RAKE taps ($L = 5, 10, 20$) are plotted in Figure 3.12 and Figure 3.13 respectively. As the number of RAKE taps increases, the performance of both MRC and EGC RAKE receivers are getting better. With other conditions the same, MRC RAKE receivers outperforms EGC RAKE receivers. The MOK performances of different M values with MRC RAKE and EGC RAKE receivers are shown in Figure 3.14 and Figure 3.15 respectively. The MOK performances of MRC RAKE and EGC RAKE receivers with different number of RAKE taps ($L = 5, 10, 20$) are plotted in Figure 3.16 and Figure 3.17 respectively. MBOK signals outperform MOK signals in all conditions since MBOK signals have half the noise dimensions as MOK signals have.

3.4 Summary

In this chapter, the contemporary UWB channel modeling methods are briefly reviewed and the IEEE 802.15.3a standard UWB channel model is studied in detail. Through both analytical and simulation studies, it has been found out that the UWB channel coherence bandwidth is generally less than 30 MHz. Comparing to hundreds of mega hertz of the data rate that UWB devices try to accomplish, the UWB channel coherence bandwidth is severely less than the UWB symbol rate. This will result in ISI in UWB communication systems.

The use of RAKE receivers in UWB communication systems is also investigated. A new simulation method for performance assessment is proposed, which is based on [RaSo03]. Comparing to the model in [RaSo03], the improvements of the proposed model are (1) the old model uses average SNR to assess the RAKE receiver performance, while the proposed model uses instantaneous SNR and the UWB channel

properties to assess the RAKE performance (2) the proposed model includes MAI while the old model doesn't. So the proposed model simulates the reality more precisely.

With the proposed simulation model, the performances of MBOK and MOK UWB signals are simulated for both MRC and EGC RAKE receivers under various conditions. For both MBOK and MOK UWB communications, MRC RAKE receivers outperform the EGC RAKE receivers in all conditions.

4 FIR Pulse Shaping Filter

Due to its wide bandwidth, UWB can convey bigger data throughput than conventional narrow band signals. In the coming IEEE802.15.3a standard, which adopts the UWB techniques, the data rate can achieve up to 480 Mbps. With other merits such as flexible implementation, base band processing (for impulse radio only), and relatively simple hardware, UWB has been shown to be promising for short-range wireless communications, such as wireless video playing, and home entertainment, etc. Since UWB signal bandwidth is ultra wide, how to control its interference to existing narrow-band systems has drawn increasing research interest. FCC Report and Order issued in February 2002, states that indoor UWB signals should meet a power transmission mask shown in Figure 1.3 [FCC02]. However, the spectra of the UWB pulses, which often appeared in the UWB literature, such as Gaussian pulse, Gaussian monocycle, and Gaussian doublet [WiSc00] [WiSc97], either don't meet the FCC requirement or don't use the given spectrum effectively. How to design a UWB pulse shape that not only satisfies FCC spectral mask, but also has the best performance becomes an important research issue.

Pulse shaping filter [WuZ02] is a useful means to control the signal spectrum and to avoid interference of UWB to other legacy narrow band signals. In [WuZh02], pulse shaping is performed in frequency domain to produce a carrier interferometry waveform such that the receiver can fully exploit frequency diversity by decomposition and recombination of the received signal. In [WuNa01], carrier interferometry chip shaping technique is developed in order that UWB DS-CDMA can operate over non-adjacent frequency bands. Our work shares the basic idea of pulse shaping with the early work, but carrier interferometry is not our research focus. Instead, with a certain transmission signal spectral constraint, this research is set to approach the best received signal quality and the highest multiple access interference suppression by optimizing transmitting and receiving pulse shaping filters jointly.

Paper [LuYa03] designs a transmission pulse shaping filter using Chebyshev approximation, and also addresses several other issues such as single band UWB, multi-band UWB, clock and frequency effects, and narrow band interference. Paper [Sele02] talks about an optimal finite impulse response (FIR) filter design approach, which can be easily adapted to devise either transmitting or receiving pulse shaping filter for the UWB systems. Both paper [LuYa03] and [Sele02] treat the pulse-shaping filter as an individual filter design problem. The advantage of this kind of method is that the filter design is isolated from other system factors (e.g., multiple access interference), and so the design problem is relatively easy to analyze. However, since the filter optimization is either at the transmitter or at the receiver side, this method also has its own disadvantage that it may not be optimal from a systematic perspective. From UWB communication system point of view, an optimal transmitting and receiving filter co-design would be a better approach to achieve the best system performance. Through the method proposed in this chapter, UWB transmitting pulse shaping filter is optimally designed to meet FCC transmission spectral mask, and meanwhile the receiving filter is also optimized to suppress the multiple access interference to the lowest level and best recover the transmitted signal as well. The transmission pulse shaping filter

optimization of the proposed joint method is developed on the basis of the algorithm described in [Sele02]. The major motivation of this research is to initiate the joint transmitting and receiving pulse shaping filter co-design method in UWB system design research.

The remainder of this chapter is organized as follows. In Section 4.1, a general SINR optimization problem is analyzed. This optimization problem is then partitioned into two sub-optimization problems, i.e., transmitting pulse shaping filter optimization and receiving filter optimization. In Section 4.2, a transmitting shaping filter optimization problem is formulated and a close-form solution to this problem is provided. In Section 4.3, a receiving pulse shaping filter optimization problem is analyzed and solved with a numeric quasi-Newton method. In Section 4.4, the proposed joint optimization method is compared with a conventional one-stage optimization method in terms of signal to noise ratio (SINR) and bit error rate (BER) through simulation. With the Intel channel model, a comparative BER simulation is performed under both line of sight (LOS) and non-line of sight (NLOS) channel environments. All simulation results confirm that the proposed method excels in terms of SINR and BER performances. Finally, Section 4.5 summarizes the findings of this research and concludes the chapter.

4.1 Optimization Problem Formulation

Time-hopping pulse position modulation (TH-PPM) impulse radio is built upon position shift of pulses with a certain shape in time domain. A system with TH-PPM could accommodate multiple simultaneous users by assigning appropriate hopping sequence to each user. The impulse radio signal from the k -th transmitter can be expressed as

$$s_k(t) = \sum_{i=0}^{\infty} \sum_{j=0}^{N_s-1} \delta(t - jT_f - c_{k,j}T_c - iT_b - b_i\Delta) \otimes g(t) \quad (4.1)$$

Notation $g(t)$ is the transmission pulse shape, and notation \otimes represents convolution operation. The delta function $\delta(t)$ is defined as $\begin{cases} \delta(t)=1, & t=0 \\ \delta(t)=0, & t \neq 0 \end{cases}$. The term $\delta(t - jT_f - c_{k,j}T_c - iT_b - b_i\Delta) \otimes g(t)$ indicates that the j -th pulse transmitted by the k -th user starts at time epoch $t - jT_f - c_{k,j}T_c - iT_b - b_i\Delta$. In equation (4.1), the sequence set $\{c_{k,j}\}$ is a pseudo-random time-hopping sequence for user k , and the range of $c_{k,j}$ is between 0 and the number of hopping positions N_h . In UWB systems with multiple users, each user has a distinct pseudorandom sequence to distinguish one from the others. Notation T_c is the chip duration and T_f is the frame duration, which is greater than or equal to $N_h T_c$. The ratio of $N_h T_c$ over T_f , i.e., $R_{frac} = N_h T_c / T_f$, represents the fraction of time over which time hopping sequence occupies. Notation b_i is information bit sequence of 1s and 0s and notation Δ is the time position difference between pulse 0 and pulse 1. The information bit duration is represented by T_b , the number of hops in each bit duration is designated by N_s , and T_b equals N_s times frame duration T_f , i.e., $T_b = N_s T_f$. If there are totally N_u active users in this system, the composite received signal at the output of the receiver antenna is given by

$$\begin{aligned} r(t) &= \sum_{k=1}^{N_u} A_k s_k(t) + z(t) \\ &= \sum_{k=1}^{N_u} A_k \left[\sum_{i=0}^{\infty} \sum_{j=0}^{N_s-1} \delta(t - jT_f - \tau_k - c_{k,j}T_c - iT_b - b_i\Delta) \otimes g(t) \right] + z(t) \end{aligned} \quad (4.2)$$

where $z(t)$ is additive white Gaussian noise (AWGN). The coefficient A_k represents the magnitude gain from the k -th transmitter to the receiver. Without losing generality, we assume that transmitter 1 is the detection target and the received signal can be expressed as

$$r_1 = y_1(t) + n_{tot}(t) \quad (4.3)$$

In equation (4.3), $y_1(t)$ is the signal, which conveys the information bit from user 1, and can be expressed as

$$y_1 = A_1 \left[\sum_{i=0}^{\infty} \sum_{j=0}^{N_s-1} \delta(t - jT_f - \tau_1 - c_{1,j}T_c - iT_b - b_i\Delta) \otimes g(t) \right] \quad (4.4)$$

Notation n_{tot} is the total noise to user 1 signal and is expressed as

$$n_{tot} = \sum_{k=2}^{N_u} A_k \sum_{i=0}^{\infty} \sum_{j=0}^{N_s-1} \delta(t - jT_f - \tau_k - c_{k,j}T_c - iT_b - b_i\Delta) \otimes g(t) + z(t) \quad (4.5)$$

In equation (4.5), the first term represents multiple access interference (MAI), and the second term $z(t)$ denotes the AWGN. If we assume that the data bits transmitted from each user are balanced, i.e., having equal probability of 1 and 0, the correlation receiver will have the same performance as the maximum likelihood receiver. Alternatively, this correlation receiver can be implemented in the form of a receiving filter. A general form of the receiving filter for TH-PPM pulse is

$$v(t) = [\delta(t - \tau_1 - jT_f - c_{1,j}T_c) - \delta(t - \tau_1 - jT_f - c_{1,j}T_c - \Delta)] \otimes m(t) \quad (4.6)$$

The receive filter, $v(t)$, is composed by shifted subtraction of $m(t)$, i.e., $m(t - \tau_1 - jT_f - c_{1,j}T_c) - m(t - \tau_1 - jT_f - c_{1,j}T_c - \Delta)$. Since $m(t)$ is a component of the receiving filter, we simply call $m(t)$ the component filter.

Based on this system structure, the symbol-by-symbol decision statistic $\alpha(t)$ is:

$$\alpha(t) = l(t) + n_d(t) \quad (4.7)$$

Signal $l(t)$ and noise $n_d(t)$ are defined as

$$l(t) = A_1 \sum_{j=0}^{N_s-1} \delta(t - iT_f - \tau_1 - c_{1,j}T_c - iT_b - b_i\Delta) \otimes [\delta(t - iT_f - \tau_1 - c_{1,j}T_c) - \delta(t - iT_f - \tau_1 - c_{1,j}T_c - \Delta)] \otimes g(t) \otimes m(t) \quad (4.8)$$

$$n_d(t) = \sum_{k=2}^{N_u} A_k \sum_{j=0}^{N_s-1} \delta(t - jT_f - \tau_k - c_{k,j}T_c - iT_b - b_i\Delta) \otimes g(t) \otimes m(t) + \sum_{j=0}^{N_s-1} z(t) \otimes m(t) \quad (4.9)$$

The signal to interference and noise ratio (SINR) at the output of the receiver becomes:

$$SINR = \frac{E(|l|^2)}{E(|n_d|^2)} \quad (4.10)$$

And the decision criterion is

$$\hat{b} = 1 \text{ if } \alpha(t) > 0, \text{ and } \hat{b} = 0 \text{ if } \alpha(t) \leq 0 \quad (4.11)$$

Let $x(t)$ denote the convolution of $g(t)$ and $m(t)$, i.e.,

$$x(t) = g(t) \otimes m(t) \quad (4.12)$$

Let σ_x^2 denote the variance of $x(t)$ during a frame time T_f , i.e., $\sigma_x^2 = \int_0^{T_f} \frac{1}{T_f} x^2(t) dt$,

and let m_p represent the peak value of $x(t)$, i.e., $m_p = \max x(t)$. The AWGN power passing through the receiving filter is designated by σ_{rec}^2 . Then the signal to interference and noise ratio SINR is

$$SINR = \frac{(N_s m_p)^2}{\sum_{k=2}^{N_u} N_s A_k^2 \sigma_x^2 + \sigma_{rec}^2} \quad (4.13)$$

When σ_{rec}^2 is dominant and the MAI can be neglected, the matched filter, i.e., the flip-flopped transmitted impulse, is the best receiving filter pulse shape according to maximal SINR criterion. When the number of users N_u and the number of hops N_s are high, the interference term is dominant, matched filter may not be the best, and the maximal SINR criterion turns out to be:

$$\max \frac{(n_s m_p)^2}{\sum_{k=2}^{N_u} N_s A_k^2 \sigma_x^2} \quad (4.14)$$

Let us keep m_p constant for now, and determine what kind of shape of $x(t)$ achieves the best SINR. If the signal gains of all users are assumed constant, equation (4.14) becomes $\min \sigma_x^2$. The maximal SINR criterion is equivalent to equation (4.15).

$$\min \int_0^{T_f} \frac{1}{T_f} x^2(t) dt \quad (4.15)$$

The ideal shape of $x(t)$, which not only has a peak value of m_p but also has a minimum variance, is a pulse shape $\delta(t)m_p$.

On the transmitter side, the transmitted signal is $\delta(t-t_1) \otimes g(t)$, where $g(t)$ is the transmission pulse shape and $\delta(t-t_1)$ has the position information. On the receiver

side, the ideal output (full signal recovery) of the receiving filter should be $\delta(t + \sigma)$. The time delay σ is introduced by causal system. If $x(t)$ has a pulse shape of $\delta(t)$, then the transmitted information is fully recovered at the receiver. For a receiver with large N_s and N_u , this recovery filter may have better SINR than the conventional matched filter does, since it minimizes the multiple access interference inside the UWB communication system.

In the real world UWB system, full signal recovery is impossible to achieve. However, we can use optimization method to achieve a best solution, which minimizes the mean square error between the received the signal and the ideal signal. The ideal signal of $x(t)$ is $x_d(t)$ and we set $x_d(t) = \delta(t)$. The system optimization problem therefore is

$$\min_x J = \sum_{n=1}^N [x(n) - x_d(n)]^2 \quad (4.16)$$

subject to: $G(f) < \text{transmission mask}$.

Simultaneous optimization of equation (4.16) is generally difficult since we need to solve a constrained optimization problem. However, in order to make the problem tractable, we can decompose the constrained optimization into two distinct unconstrained optimization problems [ZeAn03]. The first problem is to optimize $G(f)$ to satisfy the transmission mask requirement. The second one is, with the optimized transmission filter, to optimize the receiving filter in order to achieve the best signal recovery. These two problems are analyzed and solved as follows.

4.2 Transmitting Filter Optimization

The first problem, i.e., the transmitting filter optimization, can be mathematically formulated as

$$\min_G \quad \varepsilon = \int_0^{f_s/2} W(f)(G(f) - D(f))^2 df \quad (4.17)$$

In equation (4.17), ε is the objective function, $W(f)$ is a nonnegative weight function, $G(f)$ is the frequency response of the actual transmission pulse, and $D(f)$ is the ideal transmission mask. Notation f_s is the sampling frequency. This optimization is performed in the frequency domain. In order to construct an optimization model, the structure of the transmission filter needs to be determined first. It is worth noting that non-recursive filter has many advantages over recursive filter, such as constant group delay, stable computation, and symmetric coefficients [Anto93]. For simplicity, the band rejection filter, $G(f)$, is modeled as a linear-phase FIR filter. The frequency response of $G(f)$ is expressed as

$$G(f) = \sum_{n=0}^{Y_n} a(n) \cos(2\pi n f) \quad (4.18)$$

where $a(0) = g(Y_n)$, $a(n) = 2 * g(Y_n - n)$, for $1 \leq n \leq Y_n$, and $Y_n = (N - 1)/2$. The filter coefficients, $g(m)$, ($1 < m < N$), are symmetric about the middle point $Y_n = (N - 1)/2$. So only Y_n variables, i.e., $a(n)$, $n = 1 \cdots Y_n$, need to be optimized. This optimization can be solved by the first derivative method. To minimize mean square error ε , we set the first derivative of ε equal to zero, i.e.,

$$\frac{\partial \varepsilon}{\partial a(k)} = 0, \quad 0 \leq k \leq Y_n \quad (4.19)$$

Through some manipulations, the following linear equations are derived.

$$\begin{pmatrix} Q(0,0) & Q(0,1) & \cdots & Q(0,Y_n) \\ Q(1,0) & Q(1,1) & \cdots & Q(1,Y_n) \\ \vdots & \vdots & & \vdots \\ Q(Y_n,0) & Q(Y_n,1) & \cdots & Q(Y_n,Y_n) \end{pmatrix} \begin{pmatrix} a(0) \\ a(1) \\ \vdots \\ a(Y_n) \end{pmatrix} = \begin{pmatrix} b(0) \\ b(1) \\ \vdots \\ b(Y_n) \end{pmatrix} \quad (4.20)$$

where

$$Q(k,n) = \frac{2}{f_s} \int_0^{f_s/2} W(f) \cos(2\pi n f / f_s) \cos(2\pi k f / f_s) df \quad (4.21)$$

$$b(k) = \frac{2}{f_s} \int_0^{f_s/2} W(f) D(f) \cos(2\pi k f / f_s) df \quad (4.22)$$

A smart way [Sele02] to construct Q matrix is to decompose Q into simple $q(n)$ functions, and $q(n)$ can be easily calculated as

$$q(n) = \frac{2}{f_s} \int_0^{\pi} W(f) \cos(2\pi n f / f_s) df \quad (4.23)$$

Then, Q matrix can be computed as

$$Q(k, n) = \frac{1}{2} (q(k - n) + q(k + n)) \quad (4.24)$$

Therefore, the FIR filter coefficients that minimize the sum of weighted squared errors can be computed as

$$a = Q^{-1}b \quad (4.25)$$

And the optimal transmission FIR filter coefficient vector g^* can be calculated as equation (4.26).

$$g^* = [a(Yn)/2, \dots, a(1)/2, a(0), a(1)/2, \dots, a(Yn)/2] \quad (4.26)$$

The order of the transmission filter is related to the desired minimum mean square error, ε_{\min} . The lower the desired minimum mean square error is, the higher order the transmission filter is, and the closer its frequency response is to the desired transmission spectrum. The weight function, $W(f)$, is used to emphasize the importance of the frequency response error at frequency f . For instance, if we want smaller error inside a frequency range between f_1 and f_2 , $W(f)$ can be set relatively bigger in this frequency range, and vice versa.

Since the ideal frequency mask is usually in the logarithmic (or dB) scale in the real world specification, optimizing mean square error in logarithmic scale makes more sense than optimizing mean square error in linear scale. By adjusting the weight vector $W(f)$ in linear scale, optimization in logarithmic scale can be achieved using the following scale conversion method. Equation (4.27) is the goal we want to achieve, and the closed form of $W(f)$ can be easily derived as equation (4.28).

$$W(f)[G(f) - D(f)]^2 = k[\log G(f) - \log D(f)]^2 \quad (4.27)$$

$$W(f) = k \left[\frac{\log(G(f)) - \log(D(f))}{G(f) - D(f)} \right]^2 \quad (4.28)$$

Let's define the linear error $e(f)$ as the difference between $G(f)$ and $D(f)$, as shown in equation (4.29). Substituting equation (4.29) into (4.28), the closed form of $W(f)$ turns out to be equation (4.30).

$$e(f) = G(f) - D(f) \quad (4.29)$$

$$W(f) = k \left[\frac{\ln\left(1 + \frac{e(f)}{D(f)}\right)}{e(f)} \right]^2 \quad (4.30)$$

When optimization is approached, it is reasonable to assume that $e(f)/D(f)$ is relatively small and close to zero. Equation (4.31) is a well-known logarithm expansion formula. Expanding equation (4.30) with equation (4.31), after some manipulation, equation (4.32) is derived.

$$\ln(1 + z) \approx z + O(z^2), \quad z \rightarrow 0 \quad (4.31)$$

$$W(f) \propto \frac{1}{D(f)^2} \quad (4.32)$$

Therefore, by choosing the weight vector $W(f)$ inversely proportional to the amplitude square of the desired frequency response, mean square error in linear scale is approximately converted to mean square error in dB scale, in condition that the relative error $e(f)/D(f)$ is close to zero.

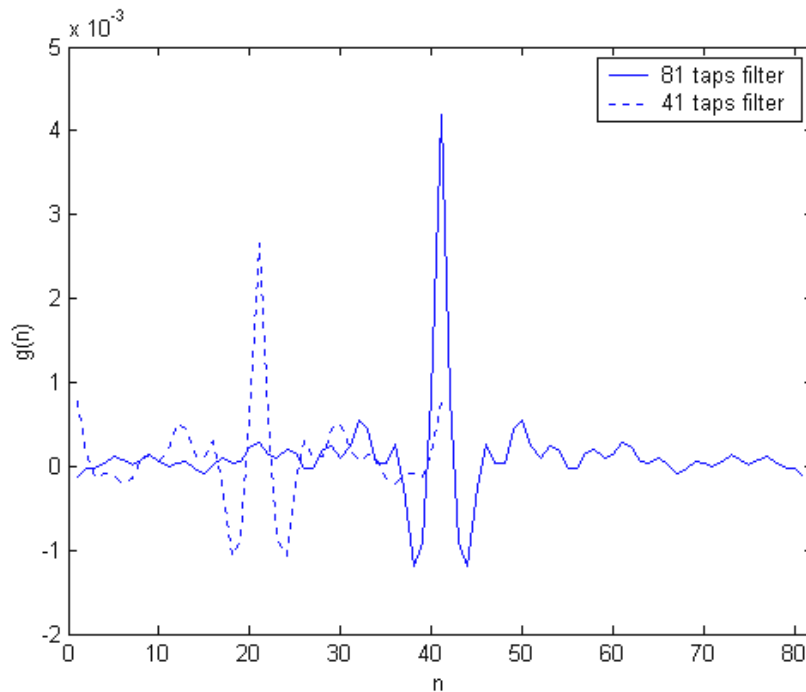


Figure 4.1 Transmission Filters (41- tap and 81-tap) Coefficients

If we set Nyquist frequency to 20 GHz, i.e., sampling frequency 40 GHz, and use the UWB indoor transmission mask in Figure 1.2 as the desired frequency mask, two FIR filters with 41 taps and 81 taps are devised following the above procedure. The coefficients of both filters are plotted in Figure 4.1.

The frequency response of the two filters with 41 and 81 taps are compared in Figure 4.2. With certain amplitude level adjustment, both the 81-tap and 41-tap filters meet the FCC indoor emission spectral mask requirement. The frequency response of the 81-tap filter is closer to the ideal spectrum mask than the 41-tap filter, and therefore the 81-tap filter can transmit more pulse power. If all other conditions are the same, the pulse power of the 81-tap filter has 2.4 dB gain higher than that of the 41-tap filter. This pulse shaping filter design method is rather a general method. It can be easily adjusted to meet literally any spectral requirements.

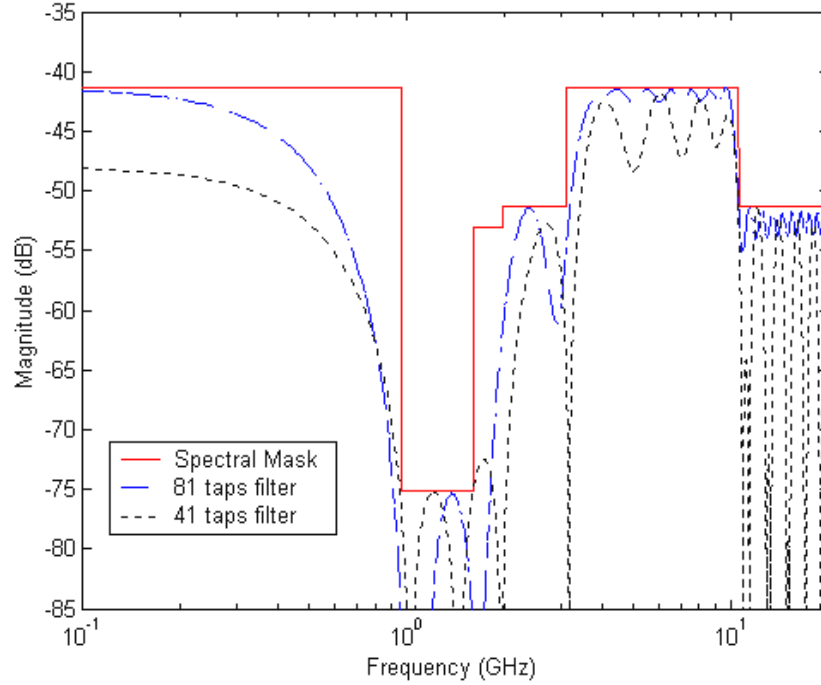


Figure 4.2 Transmission Filter Frequency Response

4.3 Receiving Filter Optimization

The second problem, i.e., the receiving filter optimization, becomes to solve a minimization problem in time domain, which is formulated as

$$\min_{m(t)} J = \int [g(t) \otimes m(t) - \delta(t)] W D(t) dt \quad (4.33)$$

The corresponding discrete problem becomes

$$\min_m J = \sum_{n=0}^{N+M-1} \{ [g \otimes m - D(n)]^2 W D(n) \} \quad (4.34)$$

Unlike the first problem, since there is a convolution operation inside the objective function, an analytical solution is difficult to derive and numerical method should be used. The objective function J is a sum of weighted square errors, therefore, it is convex and can be solved with quadratic programming [GiMu81].

This minimization problem falls into a general problem of the form

$$\min_x f(x) = \frac{1}{2} x^T H x + c^T x + b \quad (4.35)$$

The optimal solution to this general problem is well known as

$$x^* = -H^{-1}c \quad (4.36)$$

To avoid calculating Hessian matrix, H , directly, quasi-Newton method is generally preferred. A variety of Hessian matrix updating methods have been developed so far. However, the Broyden, Fletcher, Goldfarb, and Shanno (BFGS) method is considered to be the most efficient and is commonly used in engineering applications [Flet80]. The Hessian matrix updating formula given by BFGS is

$$H_{k+1} = H_k + \frac{\eta_k \eta_k^T}{\eta_k^T \gamma_k} + \frac{H_k^T \gamma_k \gamma_k^T H_k}{\gamma_k^T H_k \gamma_k} \quad (4.37)$$

where

$$\gamma_k = x_{k+1} - x_k \quad (4.38)$$

$$\eta_k = \nabla f(x_{k+1}) - \nabla f(x_k) \quad (4.39)$$

$$x_{k+1} = x_k - d H_k^{-1} \nabla f(x_k) \quad (4.40)$$

The step length, d , is determined by cubic polynomial line procedure, whose details can be found in [Flet80].

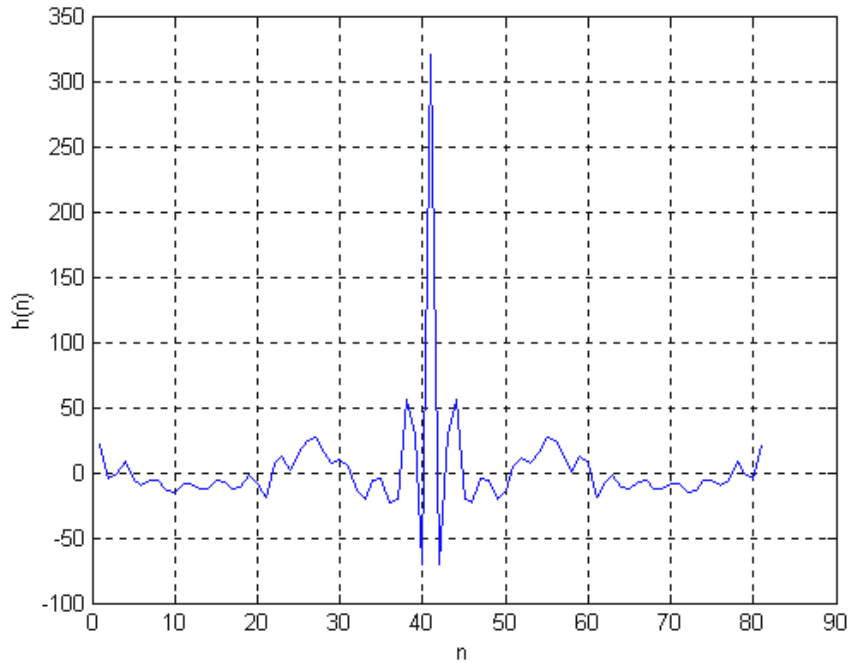


Figure 4.3 Component Filter (81-tap) Coefficients

Following the above procedure, an 81-tap FIR component receiving filter is optimized with the 81-tap transmission filter derived above. Its impulse response is demonstrated in Figure 4.3. The weight vector, $WD(n)$, is initially set to a fixed value, e.g., 1. Then, according to the output frequency response, the weight vector is slowly adjusted until the objective function value is below a certain threshold. Taking the difference of two displaced component filter constructs a receiving filter, which is actually the filter used inside the receiver.

4.4 Simulation Study

To demonstrate the interference suppression capability of the proposed joint design method, a comparative simulation study is carried out, in which the proposed joint

design method is compared with a one-stage optimization method. In the one-stage method, the receiving filter is chosen to be the same as the transmitting filter, so only one-stage optimization, i.e., the transmitting filter optimization, is needed. The proposed joint design method has a two-stage optimization, i.e., transmitting and receiving filter optimization. By joint optimization, the proposed joint design method has a superior capability in suppressing multiple access interference resulting from the TH-PPM UWB communication system.

In the real world UWB system, the signal amplitude from different users may not be the same unless perfect power control is achieved. In this simulation, the amplitude gain of each user is modeled to have a Gaussian distribution. The standard deviation of the Gaussian distribution is also called amplitude spread or power spread. To make the demonstration clear and simple, the amplitude gain of the target user is chosen to be 0 dB since other amplitude gain choices would have similar results.

Since the amplitude gain of each transmitter is a random variable, the SINR from a single time simulation may vary abruptly. So an average SINR after 1000 times of simulation is reported hereafter. When the power spread is set to 5 dB, the number of hops N_s is set to 15, the signal to AWGN ratio is kept at 40 dB, and the number of hopping positions in one frame N_h is set to 5, the relationship between the average SINR and the number of users is shown in Figure 4.4. In the one-stage optimization method, the 81-tap transmitting filter is used as both transmitting and receiving filters. In the proposed joint optimization method, the previously devised 81-tap transmitting filter and the 81-tap receiving filter are employed. In Figure 4.4, it is seen that the average SINR of joint optimization method is better than that of the one-stage optimization method, especially when the number of users is higher. The average SINR discrepancy between the one-stage optimization method and the proposed method is due to the different interference suppression capability of the two methods. As the number of user increases, the interference suppression of the joint optimization method is getting bigger and bigger, and eventually getting stable.

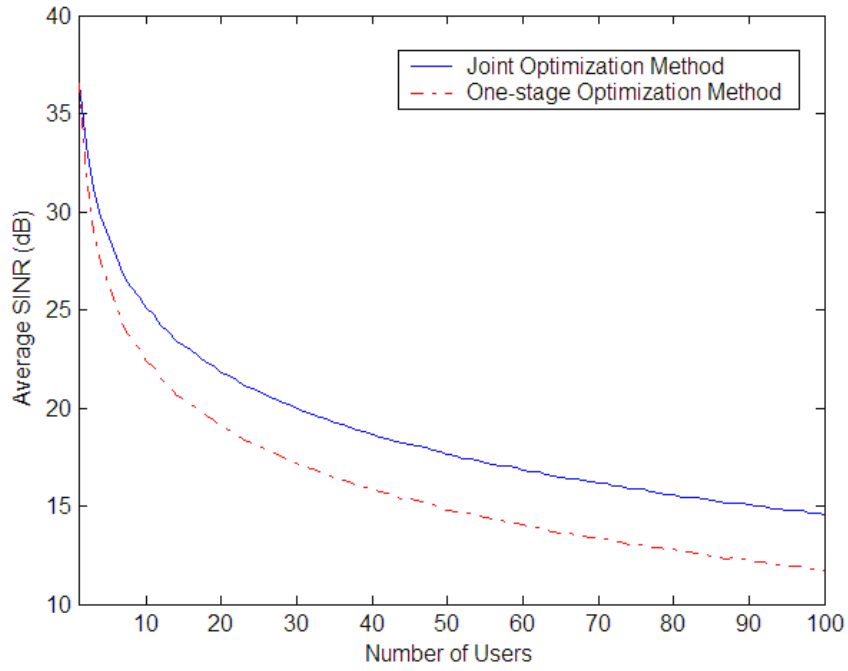


Figure 4.4 Relationship between average SINR and number of users

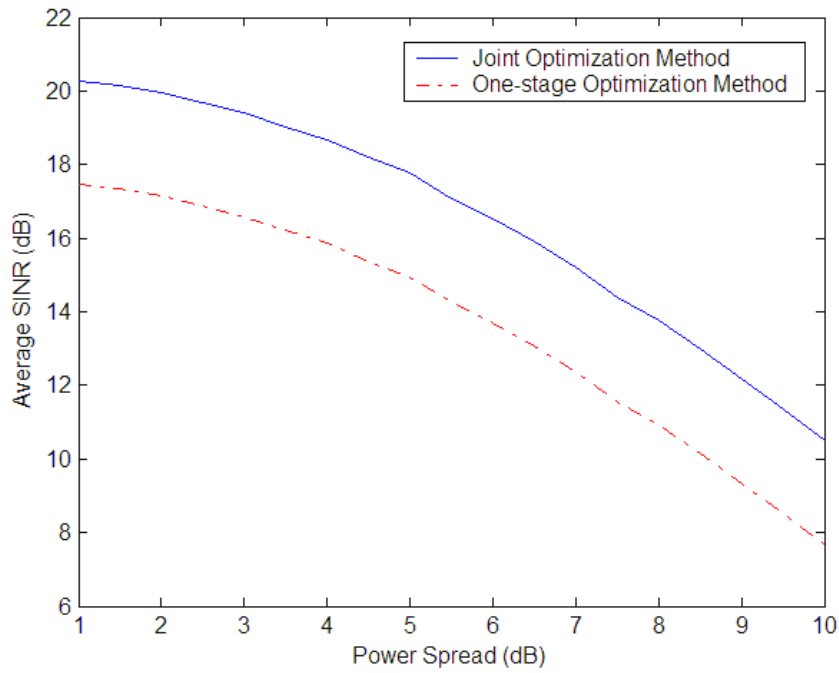


Figure 4.5 Relationship between average SINR and power spread

If the number of users is fixed to 50, the relationship of average SINR and the power spread is demonstrated in Figure 4.5. As the power spread increases, the average SINR of both methods decrease. However, the average SINR of joint optimization method is consistently better than that of the one-stage optimization method.

The parameters used in the BER simulation, such as, λ_c , λ_r , Γ , γ , σ , Ω_0 , for line of sight (LOS) and non-line of sight (NLOS) channel model are listed in Table 4.1. The receiver uses a RAKE filter to exploit the multi-path diversity, in which channel coefficients are assumed known to the receiver. Maximal-Ratio-Combining algorithm is employed to combine the signal from each finger. A 20-tap RAKE receiver is used in this simulation. The bit error rate (BER) simulation results for LOS and NLOS channel environments are demonstrated in Figure 4.6 and Figure 4.7 respectively. Again because the amplitude gain of each transmitter is a random variable, an average BER of 100 times of simulation is reported in the simulation results. In the LOS channel environment, to approach an average BER of 10^{-5} , the joint optimization method requires an Eb/No of 12 dB or better, while the one-stage optimization method needs an Eb/No of 14dB or higher. Even in NLOS channel environment, to keep an average BER of 10^{-3} , the joint optimization method requires an Eb/No of 14.5 dB or higher, which is 4 dB lower than one-stage optimization method does. In both LOS and NLOS environment, the joint optimization method outperforms the one-stage optimization method.

Table 4.1 Simulation Parameters for UWB Channel Model

Model Parameters	LOS	NLOS
λ_c (1/nsec)	1/60	1/15
λ_r (1/nsec)	1/0.6	1/0.4
Γ	20	20
γ	2	8
σ (dB)	5	5
Ω_0	1	1

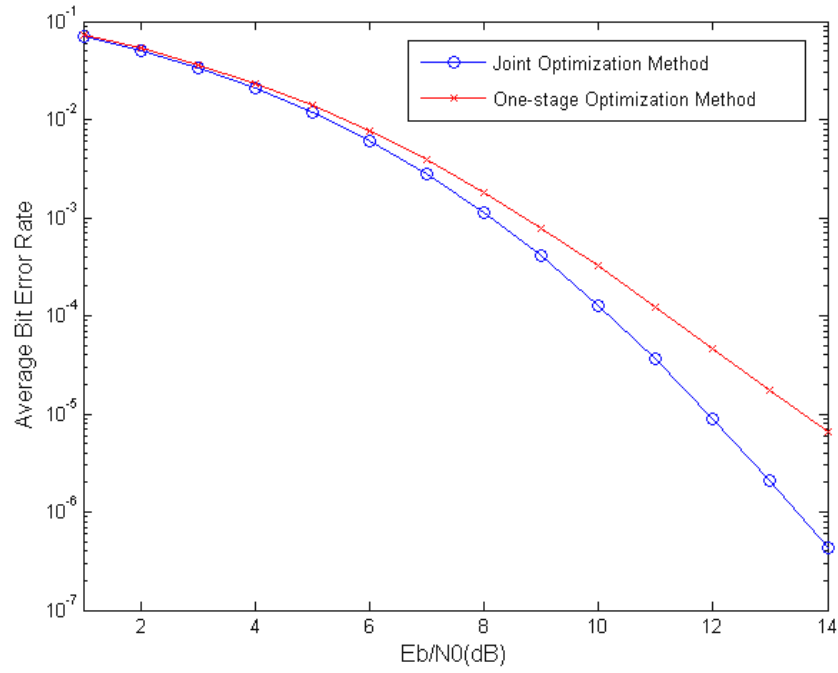


Figure 4.6 BER performance in LOS channel environment

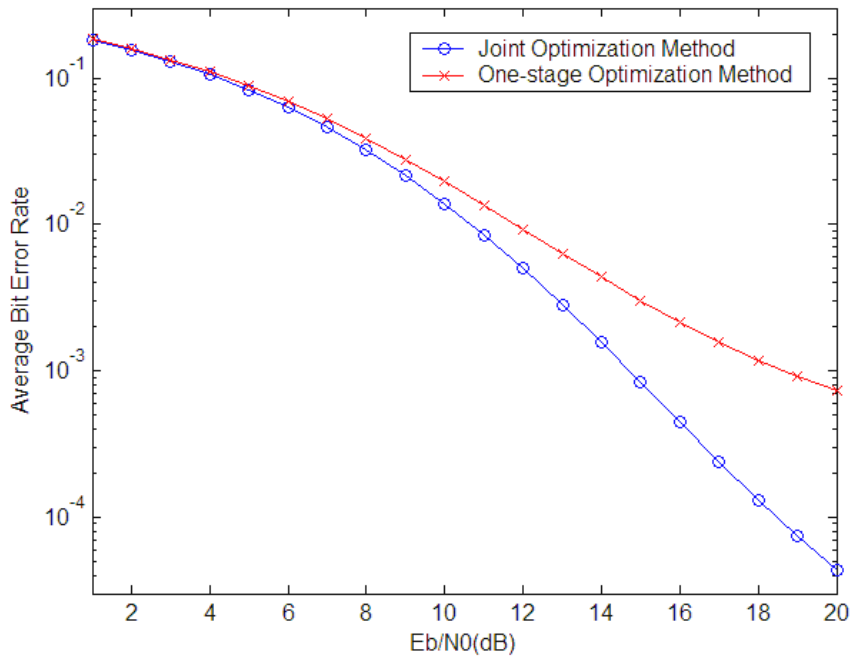


Figure 4.7 BER performance in NLOS channel environment

4.5 Conclusions

By analyzing TH-PPM UWB communication system, this chapter formulated an optimized transmitting and receiving filter design problem with a transmission power spectral mask constraint. A 2-stage solution to this optimization problem is proposed and demonstrated with an example, which satisfies the FCC indoor transmission spectral mask. In the first stage of the optimization, a closed form of optimal transmission FIR filter coefficients is demonstrated. In the second stage optimization, BFGS numerical method is shown to be an efficient tool to optimize the receiving filter. The three major advantages of the proposed joint optimization method are: (1) it has superior MAI suppression capability; (2) it can achieve the best system performance by optimizing transmitting and receiving filters jointly; (3) it can minimize the UWB interference to other narrow band systems to a tolerable level.

The interference suppression capability of the joint optimization method is demonstrated superior to that of conventional one-stage optimization method in the comparative SINR simulation study. With the Intel channel model, the BER performance of both joint optimization method and one-stage optimization method are studied under both LOS and NLOS channel environments. As noted previously, both theoretic analysis and simulation study demonstrate that the proposed joint optimization method outperforms the one-stage optimization method in terms of SINR and BER performance within TH-PPM UWB communication systems. In real world UWB applications, FIR filters require high processing power and extremely high speed sampling rate. On the other hand, IIR filters can be implemented in analog form and don't require processing power. In the next chapter, pulse shaping filters with IIR approach are discussed.

5 UWB Pulse Shaping Filter Design with IIR

In UWB system, the sampling rate and symbol rate are usually ultra high. If the pulse shaping filter is implemented in digital signal processors, e.g., with FIR digital filter, it would require extremely high speed analog-to-digital converter (ADC) and extremely powerful digital signal processors. All of these will result in expensive and complex hardware.

The key advantage of IIR filters over FIR filters is that they can usually meet the same specifications with a lower filter order, and therefore have lower computational complexity and are cheaper to implement than FIR filters. Furthermore, IIR filter can be implemented not only in digital forms, but also in analog forms. Analog IIR filters are inexpensive and don't require digital computation power at all. These are the essential merits of IIR filters, which are very attractive to UWB pulse shaping filter designers.

However, IIR filters also have their own disadvantages, i.e., IIR filters have nonlinear phases, they are more sensitive to coefficient quantization, they may have limit cycle problems, and etc. Due to the nature of infinite response of IIR filters, the signal energy tends to spread out in time domain when it passes through an IIR filter. All of these may result in SNR degradation of correlation receivers with a time-limited template.

The goal of this chapter is to design a UWB pulse shaping filter employing IIR filter to its greatest advantages and at the same time optimizing the system SNR performance by adding an optimal biquad all-pass filter. The all-pass filter is designed to adjust the phase of the incoming pulse in order to maximize the SNR of the correlation receiver.

The rest of this chapter is organized as follows. First, an elliptic filter design procedure is investigated in detail and a practical pulse shaping filter is designed following this procedure. State-space method is also employed to control limit cycles in the elliptic filter design. Second, in order to combat inconstant group delay of the pulse shaping filter, time reversal implementation and delay equalizer are studied. The effect of inconstant group delay on output SNR is also addressed. Third, in order to have the best system performance, an optimal and economic second-order all-pass pulse optimizer is proposed and demonstrated with a real world design. Finally, based on the research results, conclusions are drawn.

5.1 Elliptic Pulse Shaping Filter Design Procedure

Butterworth, Chebyshev, inverse Chebyshev, elliptic, and Bessel filters are the most commonly used IIR filters in engineering. Among them, elliptic filters are considered more efficient than the others are. So the elliptic IIR filter is employed in this research to devise UWB pulse shaping filters.

In order to design a UWB pulse shaping filter, a pass band filter specification need to be determined first. According to the FCC rulings, UWB signals can only use a frequency band from 3.1 GHz to 10.6 GHz. The UWB signal should also avoid interfering the ISM band at 5 GHz. For instance, IEEE802.11a is using this band. So a pass band filter is specified in Figure 5.1. The filter design procedure presented here is a general procedure and it is not limited to design only pass band filters.

As shown in Figure 5.1, the first stop band frequency f_{s1} of the pass band filter is 5.5 GHz, and the second stop band frequency f_{s2} is 10.5 GHz. The first pass band frequency f_{p1} is 6.0 GHz, and the second pass band frequency f_{p2} is 10 GHz. The pass band ripple A_p is selected to be 1 dB, and the stop band attenuation A_s is 40 dB. This pass band filter specification satisfies the FCC requirements and won't interfere with the ISM band applications.

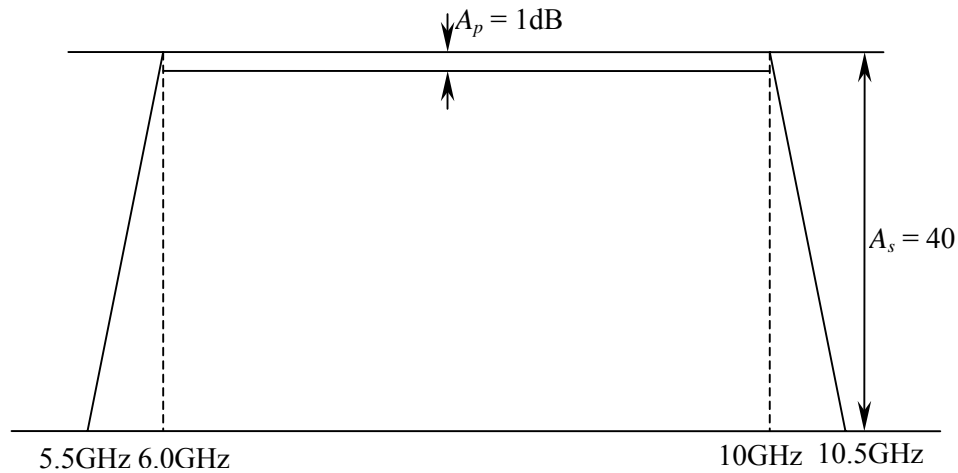


Figure 5.1 UWB Pulse Shaping Filter Specification

The general form of IIR filter is usually expressed as cascaded second-order-sections, i.e.,

$$H(s) = \frac{H_0}{D_0(s)} \prod_{i=1}^r \frac{s^2 + a_{0i}}{s^2 + b_{1i}s + b_{0i}} \quad (5.1)$$

Let n denote the order number of the filter $H(s)$. The number of second-order-sections is designated by r . The relationship between n and r is

$$r = \begin{cases} \frac{n-1}{2} & \text{for odd } n \\ \frac{n}{2} & \text{for even } n \end{cases} \quad (5.2)$$

The first-order-section term $D_0(s)$ is expressed as follows.

$$D_0(s) = \begin{cases} s + \sigma_0 & \text{for odd } n \\ 1 & \text{for even } n \end{cases} \quad (5.3)$$

Notation H_0 is a constant gain. The pole of the first-order-section, $D_0(s)$, is a complex number. The reason why second-order-sections are commonly used, is that they are tractable and easy to implement with analog parts using a cook book. In digital IIR filter implementation, second-order-sections are also easier to stabilize than direct implementation of high order transfer function.

A pass-band filter can be built with two sub-filters, one is a low pass filter and the other one is a high pass filter. The selectivity factor k is defined as the ratio of pass band frequency f_p over stop band frequency f_s for low pass filter.

$$k = \frac{f_p}{f_s} \quad (5.4)$$

For the low pass sub-filter, the selectivity factor is $k = 10\text{GHz}/10.5\text{GHz} = 0.95$. For the high pass sub-filter, the selectivity factor is $k = 5.5\text{GHz}/6\text{GHz} = 0.917$. The higher the selectivity factor, the higher order the IIR filter is. So in order to satisfy both selectivity requirements, the higher selectivity factor, i.e., $k = 0.95$, is employed to design the band-pass filter.

$$k' = \sqrt{1 - k^2} \quad (5.5)$$

$$q_0 = \frac{1(1 - \sqrt{k'})}{2(1 + \sqrt{k'})} \quad (5.6)$$

$$q = q_0 + 2q_0^5 + 15q_0^9 + 150q_0^{13} \quad (5.7)$$

$$D = \frac{10^{0.1A_a} - 1}{10^{0.1A_p} - 1} \quad (5.8)$$

$$n \geq \frac{\log 16D}{\log(1/q)} \quad (5.9)$$

Following equations (5.5) – (5.9), it is calculated that the minimal order n is 5 and the minimal order required by the high pass sub-filter is 4. For simplicity, order number 5 is chosen for both high pass and low pass sub-filters. So the band pass filter will have a total order number of 10. The low pass sub-filter is designed first. A general design procedure of a low pass sub-filter can be found in [Anto93]. Some key formulas of elliptic filter coefficients calculation are summarized in Appendix B for a quick reference. Then, we can either transform this low-pass sub-filter to a high-pass sub-filter and combine them together to form a pass band filter, or transform the low pass sub-filter to band pass filter directly.

The low pass filter can be transformed into a high pass filter by

$$s = \frac{\lambda}{\bar{s}} \quad (5.10)$$

Notation λ is a constant, which is adjusted to make the cutoff frequency to approach the desired value.

Or the low pass filter can also be transformed into a band pass filter directly by equation (5.11).

$$s = \frac{1}{B} \left(\bar{s} + \frac{w_0^2}{\bar{s}} \right) \quad (5.11)$$

Notations B and w_0 are constants. By adjusting B and w_0 , the pass band edge frequency and stop band edge frequency requirements can be satisfied. This direct method is adopted in the following study.

Following the above procedure, an analogue pass band filter is devised. The zero-pole-gain coefficients of the designed analog band pass IIR filter are listed in Table 5.1. The amplitude and phase responses of this analogue band pass filter are shown in Figure 5.2.

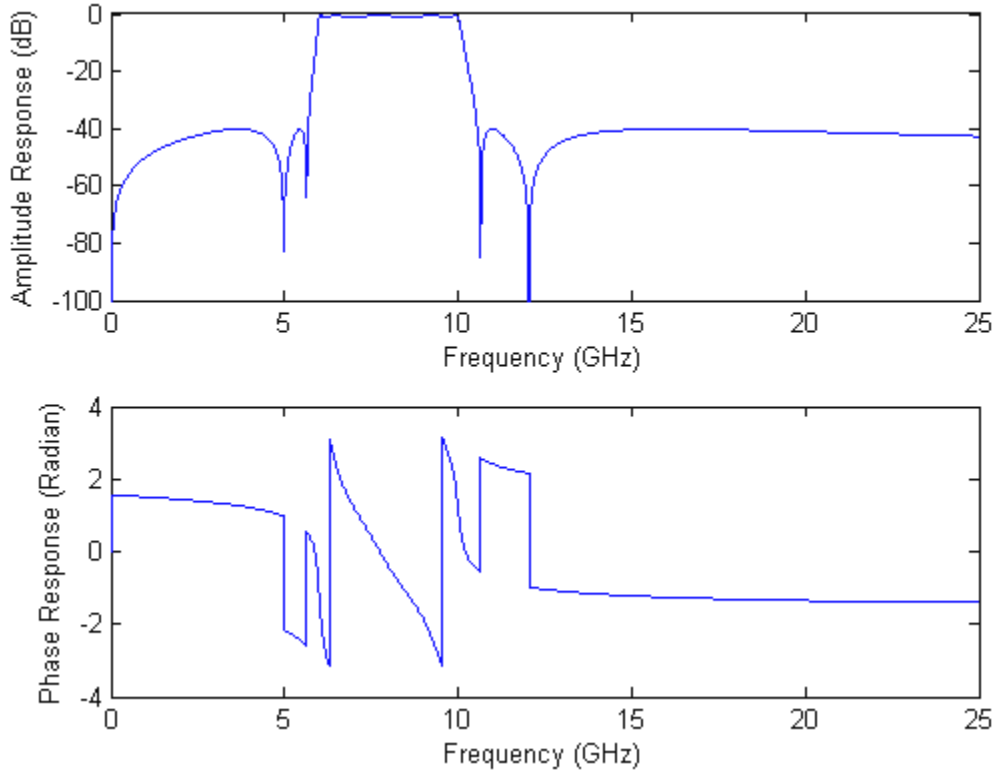


Figure 5.2 Amplitude and Phase Response of Analogue Band Pass Filter

Table 5.1 Zero-Pole-Gain Table of the Analogue Band-Pass Filter

Zeros	$1.344667409283233e-014 + 7.565115278447408e+001i$ $1.344667409283233e-014 - 7.565115278447408e+001i$ $-1.482399682156286e-015 + 6.691157736930541e+001i$ $-1.482399682156286e-015 - 6.691157736930541e+001i$ $-2.417159411619676e-015 + 3.131089175877799e+001i$ $-2.417159411619676e-015 - 3.131089175877799e+001i$ $7.998256769531378e-015 + 3.540052632727277e+001i$ $7.998256769531378e-015 - 3.540052632727277e+001i$ $-4.062780449389836e-015$
Poles	$-7.838632662293463e-001 + 6.279988089016717e+001i$ $-7.838632662293463e-001 - 6.279988089016717e+001i$ $-3.271534880189968e+000 + 5.879056809584539e+001i$

	-3.271534880189968e+000 -5.879056809584539e+001i -4.842423387323454e+000 +4.842784314833092e+001i -4.842423387323454e+000 -4.842784314833092e+001i -2.235138615785460e+000 +4.016618309365726e+001i -2.235138615785460e+000 -4.016618309365726e+001i -4.707236328183997e-001 +3.771242938245684e+001i -4.707236328183997e-001 -3.771242938245684e+001i
Gain	1.180673580791830e+000

It can be seen from Figure 5.2 that the designed elliptic filter amplitude response meets the pass-band filter specifications shown in Figure 5.1. So far, an analogue filter has been designed, the corresponding digital form can also be derived from it easily. There are several filter digitization methods to transform analog filters into digital filters, e.g., invariant impulse response method, bilinear transform method, invariant step response method, etc.

The invariant impulse response transform can be formulated as

$$H(z) = T \cdot Z\{L^{-1}[H_a(s)]|_{t=nT}\} \quad (5.12)$$

where T is the sampling period, and $H_a(s)$ is the transfer function of analog filter. Notation $Z(\cdot)$ denotes Z-transform, and notation $L^{-1}(\cdot)$ denotes inverse Laplace transform. The transfer function of the transformed digital filter is $H(z)$.

The invariant step response transform can be expressed as

$$\frac{1}{1-z^{-1}}H(z) = Z\left\{L^{-1}\left[\frac{1}{s}H(s)\right]|_{t=nT}\right\} \quad (5.13)$$

And the bilinear transform can be expressed as

$$H(z) = H_a(s)|_{s=C(1-z^{-1})/(1+z^{-1})} \quad (5.14)$$

Notation C is a constant, which can be adjusted to keep the digital filter frequency edge the same as that of analog filter. This is also called pre-warping. If the analogue filter cut off frequency is f_c , in order for the digital filter to keep the same cut off frequency, the constant C in the bilinear transform should be

$$C = 2\pi f_c \arctan(\pi f_c T) \quad (5.15)$$

Among all these three methods, the bilinear transform is the most accurate and commonly used method. Therefore, the bilinear transform method is employed to transform the above analog filter to digital filter in this research.

Digital second-order-sections (SOS) have many good properties, such as easy implementation, easy stability control, minimal coefficient quantization effect, and easy overflow control. Therefore, digital IIR filters are almost always implemented in cascaded SOS form, which can be shown in equation (5.16).

$$H(z) = \prod_{j=1}^r \frac{b_{j0} + b_{j1}z^{-1} + b_{j2}z^{-2}}{a_{j0} + a_{j1}z^{-1} + a_{j2}z^{-2}} \quad (5.16)$$

Since the order number of the analogue filter is 10, it can be broken down into 5 SOSs. Through polynomial analysis, the analogue filter transfer function is first transformed into analogue SOSs. The coefficients of the analogue SOSs are shown in the reference coefficients column of Table 5.2. Then, the reference coefficients are quantized with IEEE Q15 format. Each coefficient has totally 16 bits, the MSB is a sign bit, and the rest 15 bits represent a integer number. With two's-complement format, the integer range from -32768 to 32767 denotes a fractional range from -1 to 1. The quantized coefficients are also listed in Table 5.2.

Table 5.2 Filter Coefficients of Direct Form II Transposed Second-Order-Sections

		Quantized Coefficients	Reference Coefficients
Section 1	Numerator	0.743133544921875 0.000000000000000 -0.743133544921875	0.743143144522945050 0.00000000000012211 -0.743143144522948380
	Denominator	0.500000000000000 -0.503387451171875 0.409973144531250	0.500000000000000 -0.503400141772916370 0.409967372294259220
Section 2	Numerator	0.999969482421875 -0.205230712890625 0.999969482421875	0.999969482421875000 -0.205228830984015120 0.999969482421876550

	Denominator	0.999969482421875 -0.709808349609375 0.885009765625000	0.999969482421875000 -0.709814478231608370 0.885017473004768520
Section 3	Numerator	0.500000000000000 -0.815429687500000 0.500000000000000	0.500000000000000 -0.815422186125675190 0.499999999999991170
	Denominator	0.500000000000000 -0.659637451171875 0.454589843750000	0.500000000000000 -0.659647294896824610 0.454579005275244420
Section 4	Numerator	0.999969482421875 -0.481506347656250 0.999969482421875	0.999969482421875 -0.481502825320562430 0.999969482421878330
	Denominator	0.999969482421875 -0.610382080078125 0.972381591796875	0.999969482421875000 -0.610382497344458820 0.972389316637473410
Section 5	Numerator	0.500000000000000 -0.761749267578125 0.500000000000000	0.500000000000000 -0.761762822901048460 0.5000000000000009330
	Denominator	0.500000000000000 -0.721466064453125 0.490020751953125	0.500000000000000 -0.721469447166698360 0.490030315129091900
Overall Scaling Factor		0.0078125	

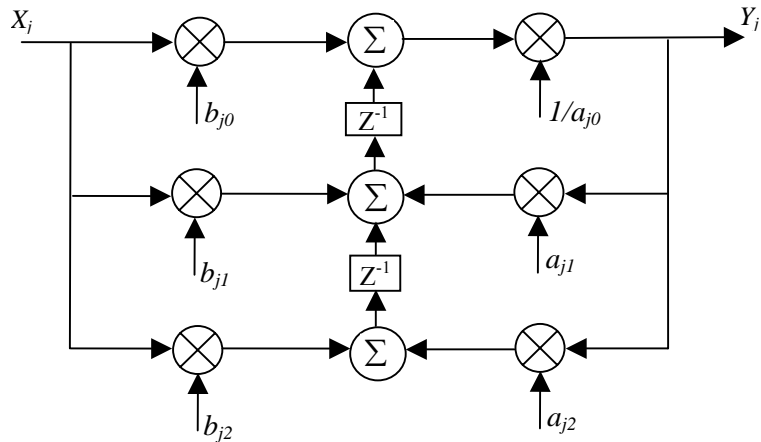


Figure 5.3 Direct Form II Transposed Implementation of SOS

Many realization methods of digital second-order IIR filters have been proposed so far [Anto93], e.g., direct form I, direct form II, direct form I transposed, direct form II

transposed, and etc. It is generally agreed upon that the direct form II transformed method is the most efficient realization [Tran03]. The direct form II transposed realization of the j -th SOS is shown in Figure 5.3, where notations X_j and Y_j are the input and output samples to the j -th SOS. The delay factor is denoted by Z^{-1} . The coefficients, a_{j0} , a_{j1} , and a_{j2} , are the numerator coefficients of the j -th SOS. The coefficients, b_{j0} , b_{j1} , and b_{j2} , are the denominator coefficients of the j -th SOS.

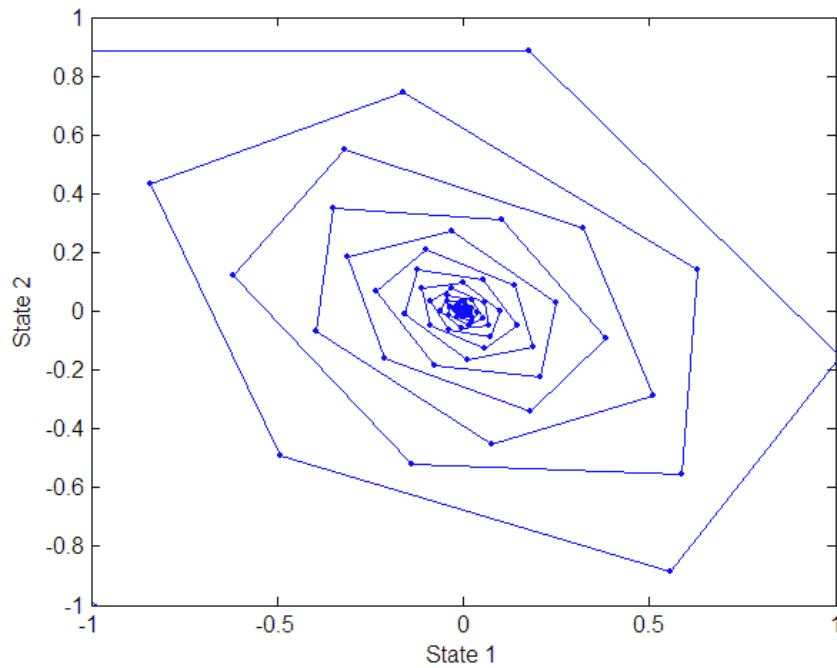


Figure 5.4 Diagram of Granular Zero-Input Limit Cycles

The zero-input limit cycle diagram of overall 5-SOS filter is shown in Figure 5.4. The dark area at the origin demonstrates that granular limit cycles may present in the filter. Then the zero-input limit cycles are checked for each of the five SOSs. The second SOS is found out to have zero-input limit cycles. Constant-input limit cycles can be eliminated by the techniques described in [Meer76], [DiAn86], [Turn83], [Tayl83], and [Verk77]. [Meer76] proposed a limit cycle free realization of second-order recursive

filters, which employs a state-space structure. A general transfer function of a second-order recursive filter can be expressed as

$$H(z) = \frac{z^2 + b_1z^1 + b_2}{z^2 + a_1z^1 + a_2} \quad (5.17)$$

The state-space structure can be generally described in equations (5.18) and (5.19).

$$\mathbf{q}(n+1) = \mathbf{A}\mathbf{q}(n) + \mathbf{B}x(n) \quad (5.18)$$

$$y(n) = \mathbf{C}^T \mathbf{q}(n) + x(n) \quad (5.19)$$

The notations, **A**, **B**, **C**, are coefficient matrixes of the state-space structure. And **q(n)** is the state vector. Following the method described in [Tayl83], the calculated coefficient matrix, **A**, **B**, and **C**, are as follows.

$$\mathbf{A} = \begin{bmatrix} 7.098361407114885e-001 & -8.850444824189049e-001 \\ 1.000000000000000e+000 & 0 \end{bmatrix}$$

$$\mathbf{B} = \begin{bmatrix} 1 \\ 0 \end{bmatrix}$$

$$\mathbf{C} = [5.046010464494503e-001 \quad 1.149555175810967e-001]$$

It has been shown that this state-space structure is free of constant-input limit cycles. The detail proof is described in [Meer76] and [Anto93]. Refurnishing the second SOS with state-space implementation, the limit cycle diagram of the overall 5-SOS IIR filter is shown in Figure 5.5. It can be seen that the states spiral down into the origin clearly and there is no dark area at the origin. This means that the granular limit cycle has been eliminated successfully.

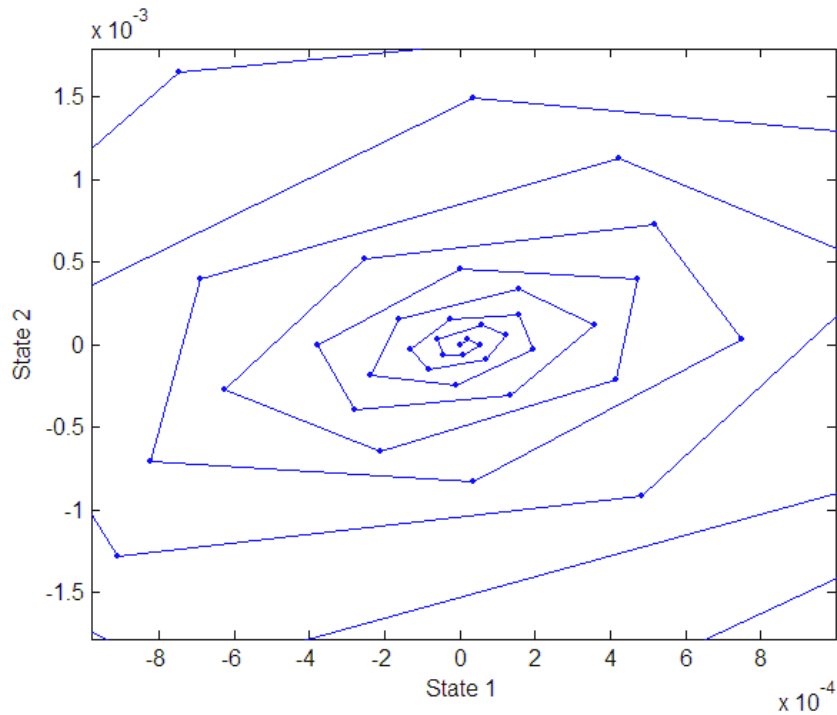


Figure 5.5 Limit Cycle Free Diagram for State-Space Implementation of SOS

5.2 Pulse Shaping Filter with Zero Phase Implementation

Unlike FIR filters, IIR pulse shaping filters neither have constant group delay, nor have linear phase response. This may be troublesome for coherent detection UWB receivers in some circumstances. This section is set to introduce a digital zero phase implementation of IIR pulse shaping filters for UWB communication systems.

For analogue filters, the phase summation of two cascaded analogue filters, $H(s)$ and $H(-s)$, is zero. As demonstrated in Figure 5.6, the filter of transfer function $H(-s)$ is a time-reversed version of the filter with transfer function $H(s)$.

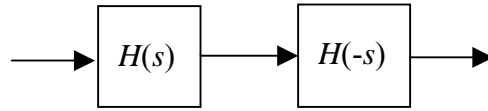


Figure 5.6 Theoretical Analog Zero-Phase Filter Structure

For digital filters, $H(z^{-1})$ is the time-reversed version of the transfer function $H(z)$. The phase of the two cascaded digital filters, as shown in Figure 5.7, is zero.

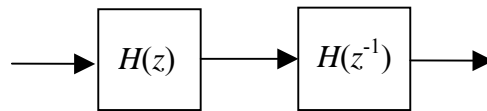


Figure 5.7 Theoretical Digital Zero-Phase Filter Structure

The theoretical analog zero-phase filter can't be implemented in real-world applications. The reason is that $H(s)$ and $H(-s)$ can't be both causal at the same time. If $H(s)$ is causal, then its time reversed version $H(-s)$ is not causal, and vice versa. On the other hand, if $H(s)$ has all poles on the left plane, then $H(-s)$ must have all poles on the right plane. Consequently, $H(s)$ and $H(-s)$ can't be stable simultaneously.

However, in digital applications, this dilemma can be overcome by time reversal of incoming samples instead of time reversal of the filter itself. As demonstrated in Figure 5.8, the output of each filter is reversed in time domain. Since two identical filters are used, the time reversal needs to be conducted twice altogether.

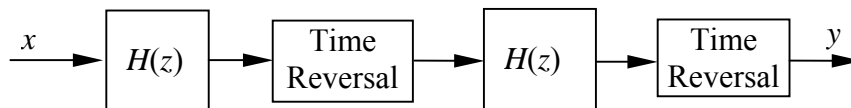


Figure 5.8 Theoretic Zero Phase Digital Filter Implementation

The filter implementation structure shown in Figure 5.8 demonstrates a theoretical possibility of digital filter of zero phase response. However, it suffers long sample delay. [PoCh91] first proposed a technique for realizing linear phase IIR filters, and later on [KuMi03] made a truncation improvement of the impulse response on the basis of [PoCh91]. The implementation architecture of zero phase filter proposed in [PoCh91] is demonstrated in Figure 5.9.

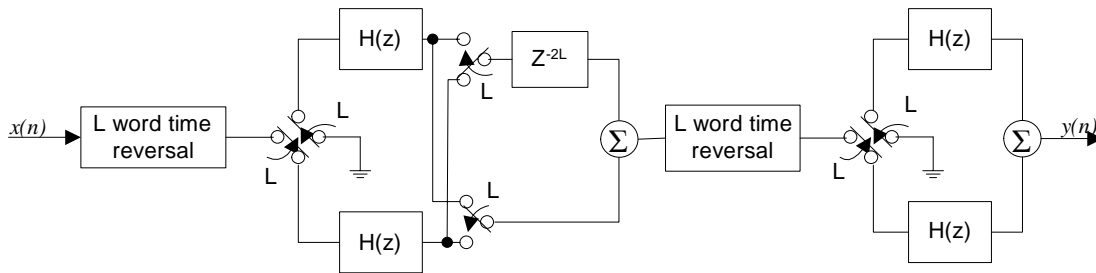


Figure 5.9 Practical Zero Phase Digital Filter Implementation [PoCh91]

The sub-filter $H(z)$ can be any type digital IIR filter, e.g., Butterworth, Chebyshev I, Chebyshev II, elliptic, Bessel, etc. If the $H(z)$ satisfies that its stop band attenuation is A_s dB and its pass band attenuation is A_p dB, then the theoretical pass band and the stop band attenuation of the overall zero-phase filter will be $2 * A_p$ dB and $2 * A_s$ dB respectively. The factor of 2 comes from the cascade of two filters with identical amplitude response.

Instead of reversing the filter coefficients, the time reversal is conducted on the incoming signal samples. This is implemented with a last-in-first-out (LIFO) memory. After L samples arriving into the LIFO, the time reversed samples are read out to next filter, for instance, the last sample is read out first and the second last sample is read out second. There are totally two kinds of input sources to the two parallel filters. One input is the time-reversed signal and the other input is zero. If one sub-filter takes time-reversed signal, the other sub-filter must take zero input and vice versa. Every L samples, the sub-filters will switch their input samples, either from zeros to time

reversed signal or from time reversed signal to zero. When switching from zeros to time-reversed signal, the sub-filter must reset all its states. This is equivalent to truncate the impulse response of $H(z)$ to L samples. After truncation, the IIR filter $H(z)$ is actually changed to a FIR filter. So some bad properties of IIR, such as limit cycles, will automatically disappear.

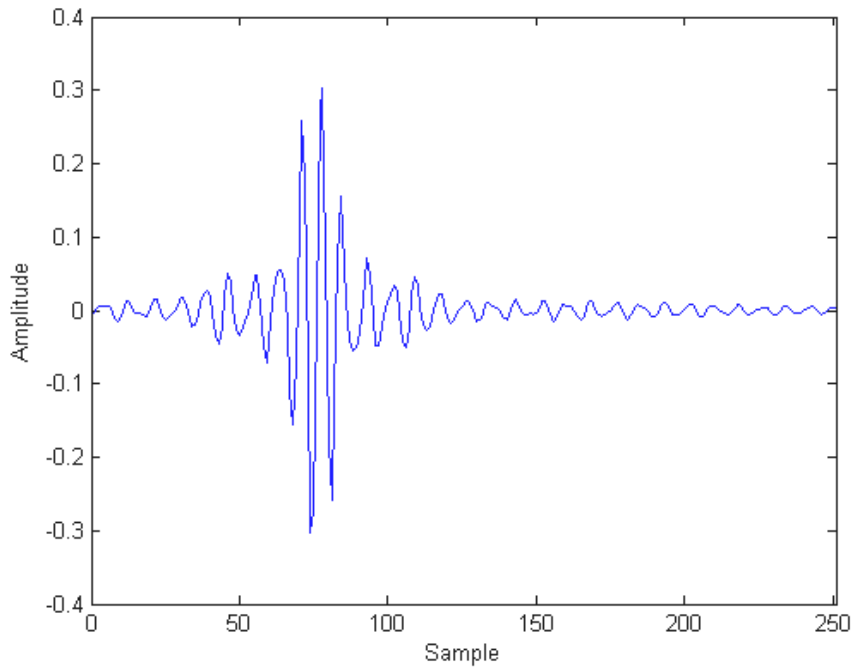


Figure 5.10 Filtered Monocycle by Zero-Phase Filter Implementation

The outputs of the two sub-filters are added up and then time reversed again to form the input signal to the next filter $H(z)$. For the reason of symmetry, this second filter is truncated the same way as the first filter and this also results in the immunity of limit cycles.

The filtered monocycle pulse shape by zero-phase filter implementation is shown in Figure 5.10, while the filtered monocycle pulse shape by two identical filters of $H(z)$ is demonstrated in Figure 5.11. Comparing the two figures, it is obvious that the pulse

shape filtered by the zero-phase filter implementation is more symmetrical and its energy is more centralized than the monocycle filtered by two identical filters.

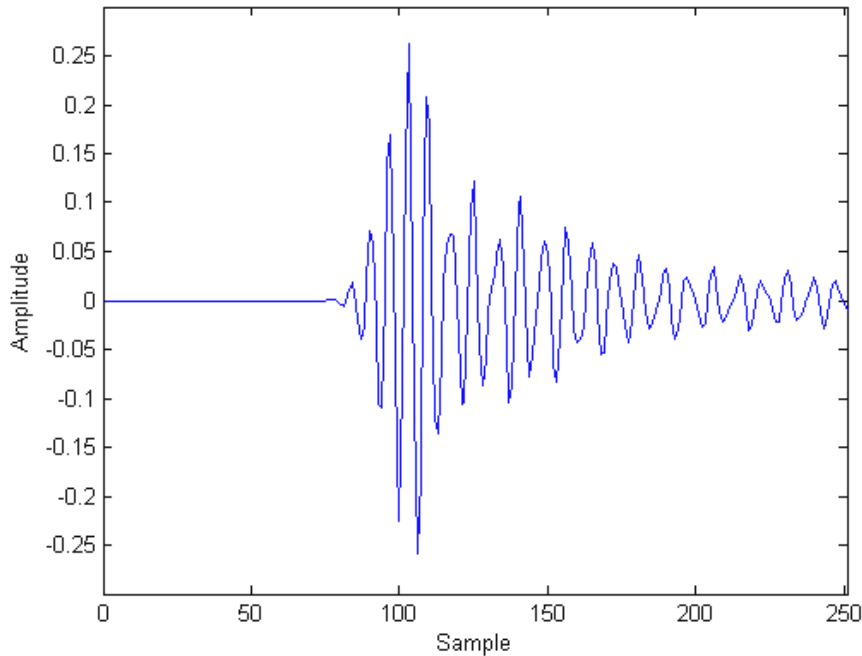


Figure 5.11 Filtered Monocycle by Two Identical Filters of $H(z)$

5.3 Pulse Shaping Filter with Constant Delay through Delay Equalizer

It is possible to design an all-pass filter, i.e., delay equalizer, to equalize the group delay of any IIR filter to any desired accuracy over a band of frequency. It is also worth to note that optimal FIR equalizer is more efficient than IIR all-pass filter in equalizing the group delay [RaGo75]. In order to equalize the same amount of phase shift, IIR all-pass filter will take many biquadratic sections, while a FIR equalizer with relatively short length will be able to do so. More detail comparison and explanation of why FIR

approach is more efficient than IIR approach in group delay equalization are explicated in [RaGo75]. Even though the optimal FIR filter is generally more effective than IIR delay equalizer in terms of mitigating the inconstant group delay, IIR delay equalizer is still useful in analogue filter implementation. Since FIR filter can only be implemented in digital form, it takes the computation power of the digital signal processor. On the contrary, IIR delay equalizer can be implemented in analogue devices in order to save the computation power. In the following, the design procedure and characterization of the all-pass IIR delay equalizer is studied.

A general form of all-pass filter, which consists of several cascaded SOSs, is shown in equation (5.20).

$$H_E(z) = \prod_{j=1}^M \frac{c_{2j} + c_{1j}z^{-1} + z^{-2}}{1 + c_{1j}z^{-2} + c_{2j}z^{-2}} \quad (5.20)$$

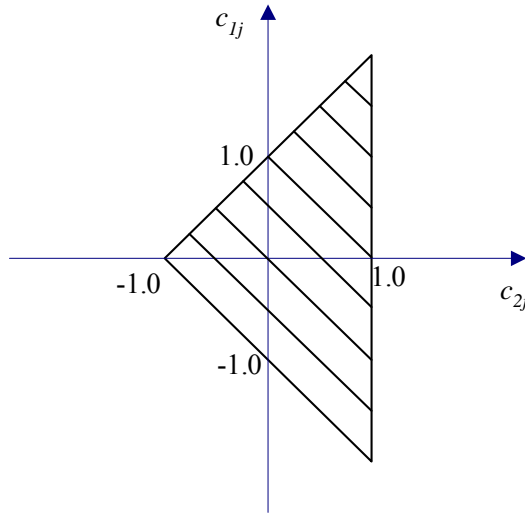


Figure 5.12 Stable Region in (c_{1j}, c_{2j}) Plane

The equalizer is stable if and only if the transfer function coefficients satisfy all the following three conditions: (1) $c_{2j} < 1$ (2) $c_{1j} - c_{2j} < 1$ (3) $c_{1j} + c_{2j} > -1$. The stable

region of the biquadratic coefficients of a single SOS is then illustrated as the shaded area in Figure 5.12.

Let us define coefficients vector c as $c = [c_{11} \ c_{21} \ c_{12} \ c_{22} \ \cdots \ c_{2M}]$. And the intermediate variables $D_j(w)$ and $C_j(w)$ are defined as

$$D_j(w) = 1 - c_{2j}^2 + c_{1j}(1 - c_{2j})\cos(wT) \quad (5.21)$$

$$C_j(w) = (1 - c_{2j})^2 + c_{1j}^2 + 2c_{1j}(1 + c_{2j})\cos(wT) + 4c_{0j}\cos^2(wT) \quad (5.22)$$

The phase response $\theta_E(c, w)$ of the equalizer $H_E(e^{jwT})$ is

$$\theta_E(c, w) = \text{angle}(H_E(e^{jwT})) \quad (5.23)$$

The equalizer group delay $\tau_E(c, w)$ is defined as

$$\tau_E(c, w) = -\frac{d\theta_E(w)}{dw} \quad (5.24)$$

Substituting equations (5.21) and (5.22) into equation (5.24), the group delay $\tau_E(c, w)$ of the equalizer becomes equation (5.25).

$$\tau_E(c, w) = 2T \sum_{j=1}^M \frac{D_j(w)}{C_j(w)} \quad (5.25)$$

The combined group delay of both the filter and equalizer is

$$\tau_{FE}(c, w) = \tau_F(w) + \tau_E(c, w) \quad (5.26)$$

By adjusting coefficient vector, c , the maximum error between combined filter group delay, τ_{FE} , and the maximum group delay of the original filter, τ_0 , should be minimized. The equalizer optimization problem can be formulated as equation (5.27).

$$\min_c [\max_{1 \leq i \leq K} |\tau_{FE}(c, w_i) - \tau_0|] \quad (5.27)$$

Subject to:

$$c_{2j} < 1$$

$$c_{1j} - c_{2j} < 1$$

$$c_{1j} + c_{2j} > -1$$

This is a constrained optimization problem. Even though it is not known whether the evaluation function, $\tau_{FE}(c, w_i) - \tau_0$, is convex or not, the first derivatives of this evaluation function can be derived. With the information of these first derivatives, the optimization problem can be solved. Luckily, there exists software, MATLAB, which can be used to solve the group delay equalizer problem. With MATLAB, a five biquadratic delay equalizer is devised. The coefficients of the equalizer are listed in Table 5.3. The phase response and group delay of the equalized filter are shown in Figure 5.13 and Figure 5.14, respectively. The zero-pole diagram of the equalizer is shown in Figure 5.15. It is observed that the phase of the equalized filter is closer to linear than the filter without equalizer. The group delay in the pass band of the equalized filter is approximately constant albeit with small ripples. The monocycle pulse shape filtered by the equalized filter is shown in Figure 5.16. This filtered monocycle is not as symmetric as the monocycle filtered by time-reversed implementation. This fact also confirms that group delay equalizer is not an excellent means to mitigate the inconstant group delay, but it saves computation power. With some performance compromise, delay equalizer is still an inexpensive tool to mitigate the non-constant group delay effects of the UWB pulse shaping filters.

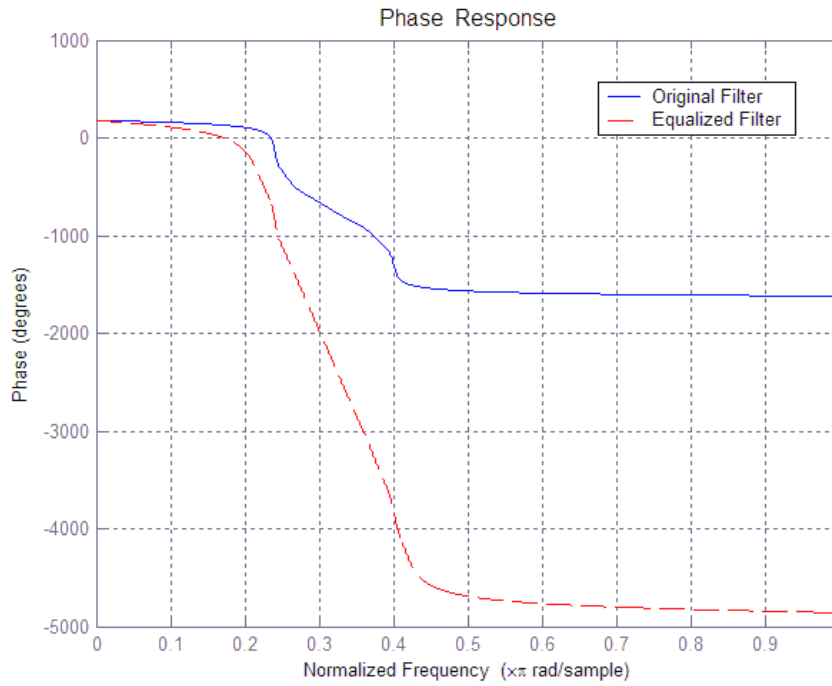


Figure 5.13 Phase Response of the Equalized filter

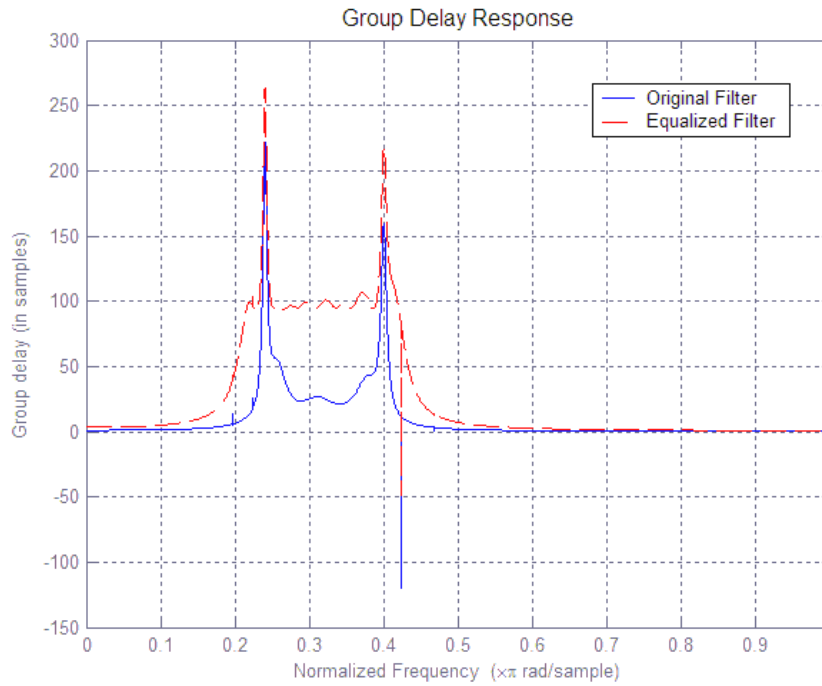


Figure 5.14 Group Delay Response of the Equalized Filter

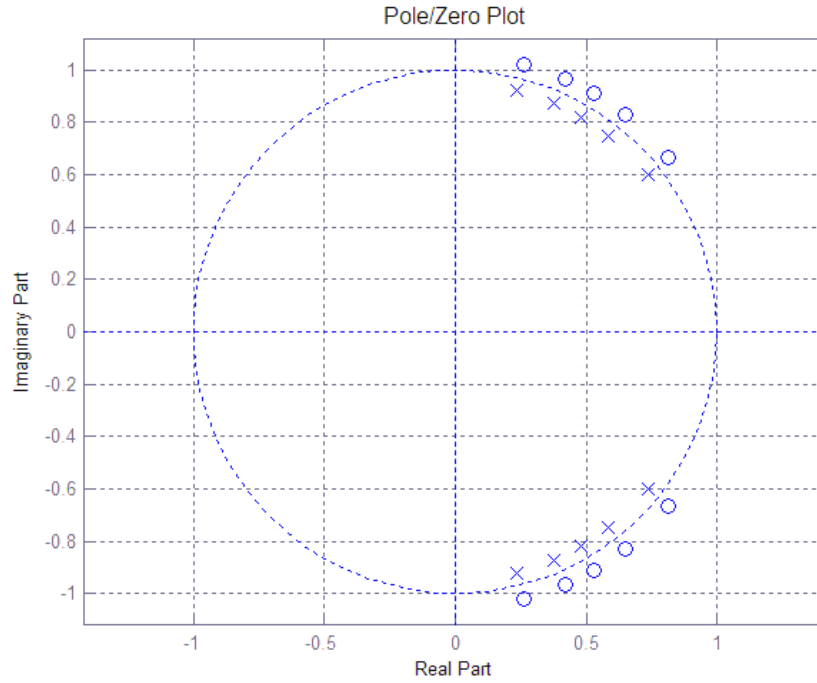


Figure 5.15 Zero-Pole Diagram of the Equalizer

Table 5.3 Filter Coefficients of the Equalizer

		Quantized Coefficients	Reference Coefficients
Section 1	Numerator	0.598724365234375 -0.635040283203125 0.663391113281250	0.598718667237059240 -0.635034492369859200 0.663400185305499490
	Denominator	0.999969482421875 -0.957214355468750 0.902465820312500	0.999969482421875000 -0.957212745364971250 0.902472457883299660
	Scaling Factor	1	
Section 2	Numerator	0.500000000000000 -0.261871337890625 0.553985595703125	0.499984741210937500 -0.261877047945403450 0.553999713253206520
	Denominator	0.999969482421875 -0.472686767578125 0.902465820312500	0.999969482421875000 -0.472688071540906310 0.902472457885482250
	Scaling Factor	2	
Section 3	Numerator	0.500000000000000 -0.814453125000000 0.554016113281250	0.500000000000000 -0.814466793115065310 0.554016620498734350

	Denominator	0.500000000000000 -0.735046386718750 0.451263427734375	0.500000000000000 -0.735056280785825410 0.451249999999898230
	Scaling Factor	1	
Section 4	Numerator	0.500000000000000 -0.647705078125000 0.554016113281250	0.500000000000000 -0.647717786920140370 0.554016620497958190
	Denominator	0.500000000000000 -0.584564208984375 0.451263427734375	0.500000000000000 -0.584565302697755310 0.451250000000673390
	Scaling Factor	1	
Section 5	Numerator	0.500000000000000 -0.419464111328125 0.553985595703125	0.499984741210937500 -0.419455672526934780 0.553999713252499080
	Denominator	0.999969482421875 -0.757110595703125 0.902465820312500	0.999969482421875000 -0.757117488914737960 0.902472457887298020
	Scaling Factor	2	

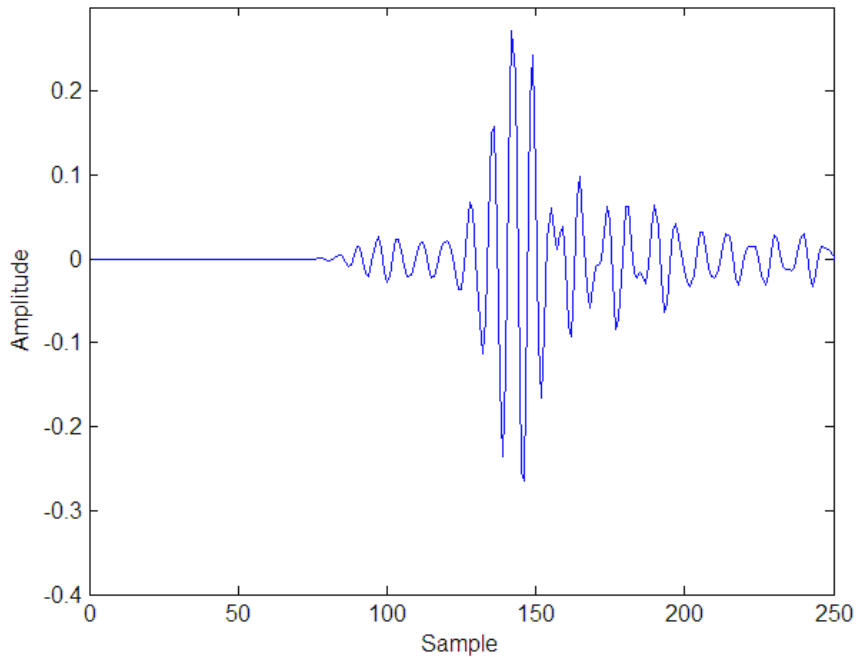


Figure 5.16 Monocycle Pulse Shape Filtered by Delay Equalizer

5.4 UWB Receiver with Sinusoidal Template

Similar to all other narrow band receivers, the UWB receiver is actually a correlation receiver, which is illustrated in Figure 5.17. The received signal is denoted as $x(t)$, and the output of the correlation receiver is $y(t)$. The sampling period of the correlation receiver is Δt . The template signal is designated by $v(t)$.

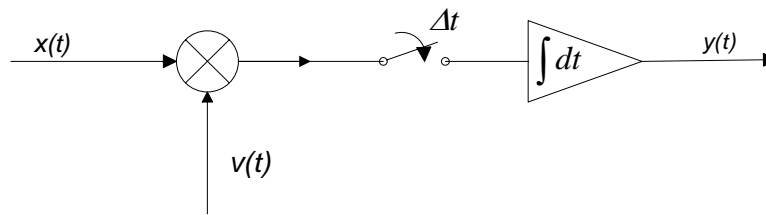


Figure 5.17 UWB Correlation Receiver

After passing through two identical pass band filters, i.e., the transmission and receiver pulse shaping filters, the filtered Gaussian pulse, monocycle, and doublet waveforms, are demonstrated in Figure 5.18. It is obvious that no matter what pulses are used in UWB transmitter, the received signals after the band-pass filters are all similar. Due to the nature of IIR filters, the received signals tend to spread out in time domain. As the signals spread away, the signal envelope magnitude tapers and the signal waveforms tend to be irregular. The conundrum, so far, is that designing a template closely matched to the received signal will be very difficult, if not impossible, due to the irregularity at the tail of the received signal. In order to avoid locally generating the exactly matched receiving template, transmitted-reference method has been proposed for UWB communication systems [GiWi04] [ChSc04]. In transmitted-reference method, the current received pulse is correlated with the previous received pulse.

Similar to differential demodulation methods, the received noise is doubled in the transmitted-reference receivers. In the following sections, a pulse shaping optimizer is proposed to improve the performance of coherent UWB receivers with simplified receiving template.

Since the received pulse shape in the energy concentrated area is close to sinusoidal waveform, some researchers proposed to use sinusoidal template in the UWB receivers [Lee02]. A close-in look of the filtered doublet and sinusoidal wave are shown in Figure 5.19. In practice, sinusoidal wave is easy to generate and the cost of the oscillator is also relatively inexpensive. It will be economical to use sinusoid waveform as the receiving template signal. Now that the energy of the transmitted pulse is spread out in time domain at the receiver, longer template will be beneficial to collecting more signal energy.

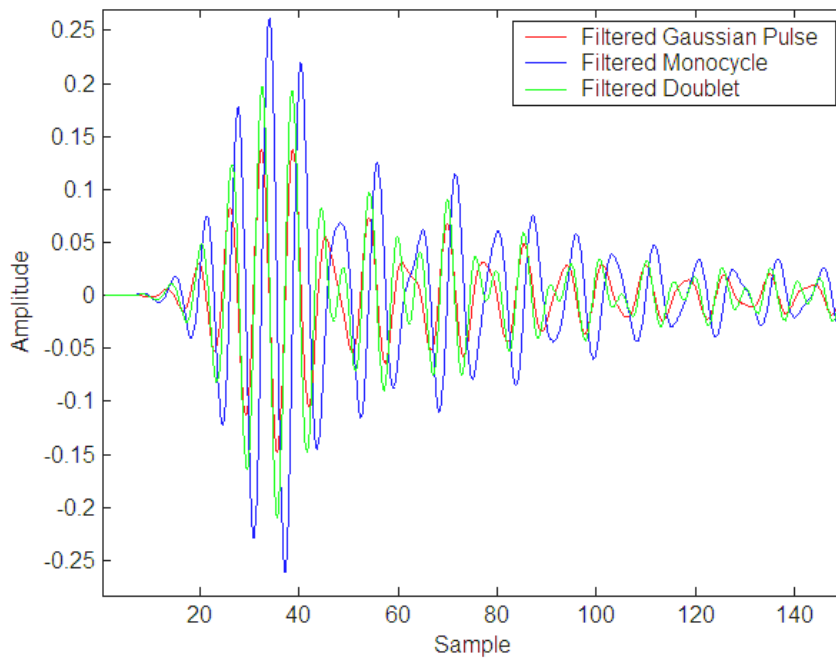


Figure 5.18 Filtered UWB Pulses

Unlike traditional narrow band receivers, using sinusoidal template in the UWB receiver gives rise to another problem, i.e., the SNR degradation of the received signal due to the unmatched receiving template.

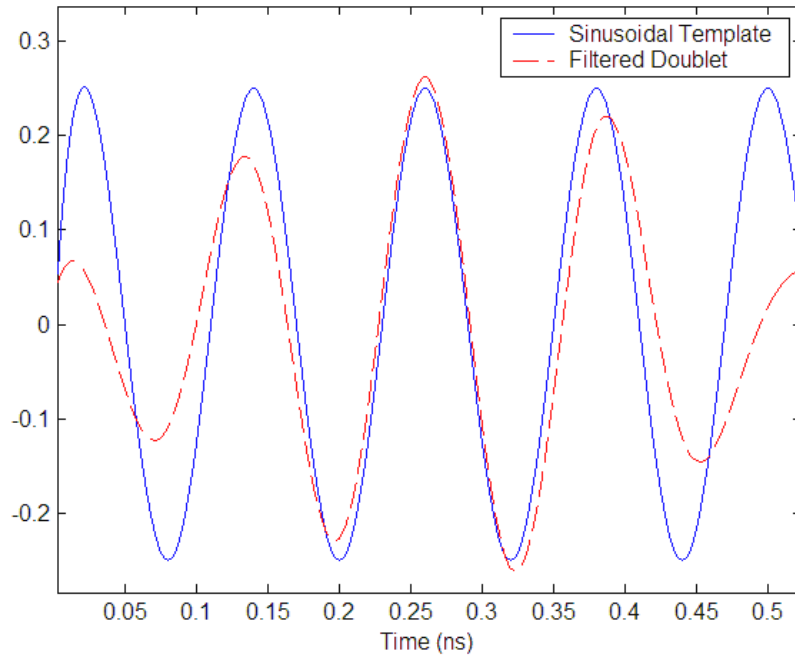


Figure 5.19 Filtered Doublet and Template Wave

In the UWB correlation receivers, the incoming signal $w(t)$ is first correlated with a template signal $v(t)$, then integrated and sampled. The input signal to correlation receiver, $x(t)$, can be expressed as

$$x(t) = \sqrt{E_p} w(t) + n(t) \quad (5.28)$$

In equation (5.28), E_p is the pulse energy, and $n(t)$ is the received thermal noise. The thermal noise density is designated by N_0 , i.e.,

$$N_0 = kT \quad (5.29)$$

Thermal noise density, N_0 , is the product of Boltzmann coefficient, k , and the absolute environment temperature, T , in Kelvin. The noise autocorrelation, $R_{nn}(t_1, t_2)$, is calculated as

$$R_{nn}(t_1, t_2) = N_0 \delta(t_1 - t_2) \quad (5.30)$$

The correlation $R_{wv}(\tau)$ of the input signal $w(t)$ and the sinusoidal template $v(t)$ is formulated in equation (5.31), in which the symbol Δt denotes the sampling period.

$$R_{wv}(\tau) = \int_0^{\Delta t} w(t) \cdot v(t - \tau) dt \quad (5.31)$$

The autocorrelation of the template signal itself is

$$R_{vv}(\tau) = \int_0^{\Delta t} v(t) \cdot v(t - \tau) dt \quad (5.32)$$

The total noise power N of the thermal noise $n(t)$ can be calculated as

$$N = N_0 R_{vv}(0) \quad (5.33)$$

Therefore, the SNR of the received signal is

$$SNR = \frac{E_p}{N_0} \cdot \frac{R_{wv}^2(\tau)}{R_{vv}(0)} \quad (5.34)$$

Symbol τ denotes the time offset of the template relative to the received pulse. Under the ideal conditions, i.e., the time offset is zero and the template is the same as the clean incoming impulse, the SNR is maximal [Thom68]. However, when the template is not the same as the clean incoming impulse, the SNR will degrade. In the following section, a pulse shape optimizer is proposed to combat this SNR degradation problem.

5.5 Pulse Shape Optimizer

In this section, a pulse shape optimizer is proposed to achieve better receiver SNR. This pulse shape optimizer is located right before the correlation receiver and after the band-pass filter in a common UWB transceiver system, as shown in Figure 5.20.

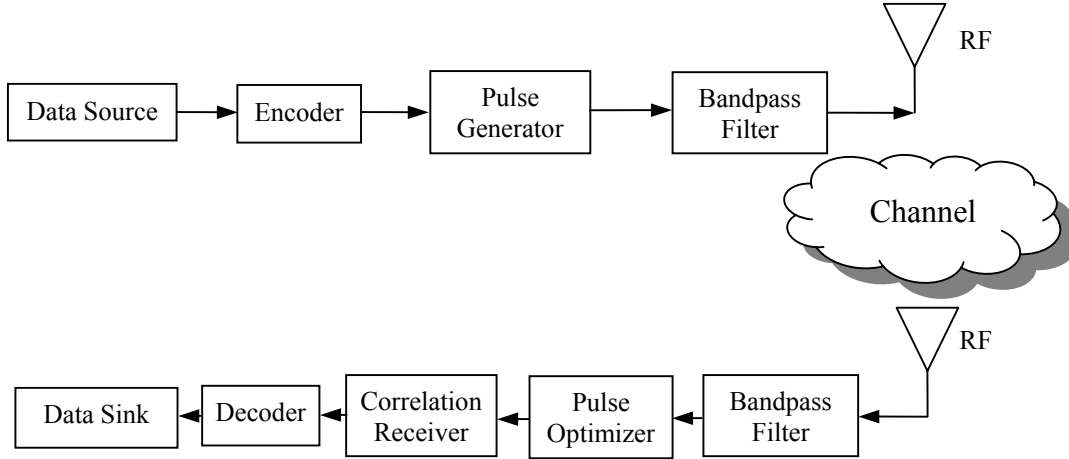


Figure 5.20 The Proposed UWB Transceiver System

The pulse optimizer, which is used to maximize the correlation receiver output SNR, is actually an all-pass filter. The all-pass filter is first designed in digital domain and then transformed into analog domain, as analog all-pass filter is an economic way to implement the pulse optimizer in the real world.

The general digital form of the optimizer is expressed as

$$H_p(z) = \prod_{j=1}^M \frac{c_{2j} + c_{1j}z^{-1} + z^{-2}}{1 + c_{1j}z^{-2} + c_{2j}z^{-2}} \quad (5.35)$$

The constrained optimization problem is formulated as

$$\max_c \frac{E_p}{N_0} \cdot \frac{R_{vv}^2(\tau)}{R_{vv}(0)} \quad (5.36)$$

Subject to

$$c_{2j} < 1$$

$$c_{1j} - c_{oj} < 1$$

$$c_{1j} - c_{2j} > -1$$

If perfect synchronization is assumed, i.e., the time offset τ is assumed to be zero, the problem of maximizing SNR is equivalent to maximizing $R_{vv}(0)$. Therefore, the design problem of pulse optimizer becomes

$$\max_c R_{vv}(0) \quad (5.37)$$

Subject to:

$$c_{2j} < 1$$

$$c_{1j} - c_{oj} < 1$$

$$c_{1j} - c_{2j} > -1$$

If only one SOS is used, i.e., $M=1$, the pulse optimizer transfer function is simplified to

$$H_p(z) = \frac{c_2 + c_1 z^{-1} + z^{-2}}{1 + c_1 z^{-2} + c_2 z^{-2}} \quad (5.38)$$

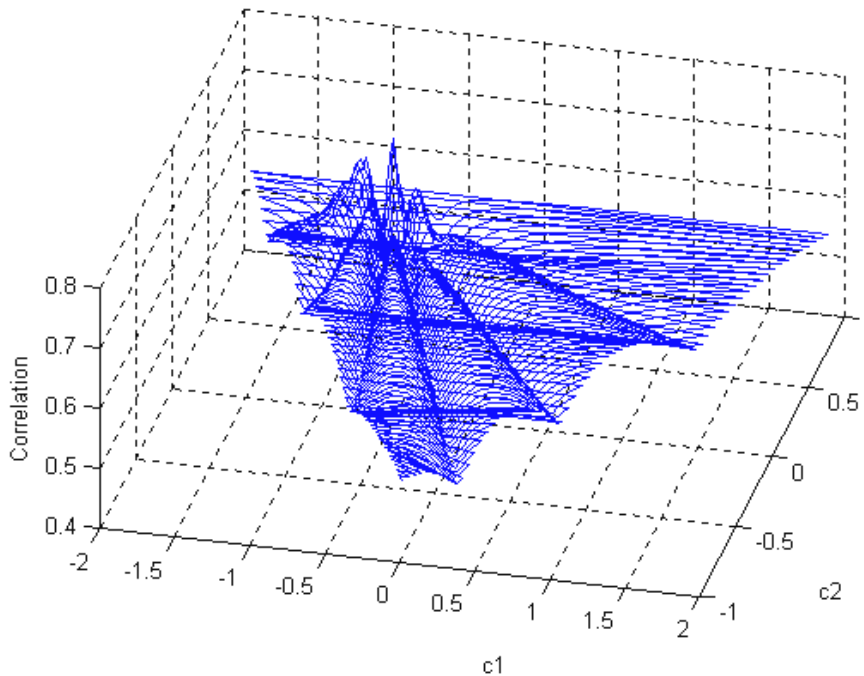


Figure 5.21 Relationship between Correlation and Biquad Coefficients c_1 and c_2 .

As demonstrated in Figure 5.21, the objective function of a single SOS pulse optimizer has multiple maxima. Many traditional optimization methods, which use gradients or higher derivatives, don't work well with this kind of objective function. Instead of searching from point to point, genetic algorithms search from a group of points, i.e., genes, to a new group of points through evolution, in which the genes with better objective function values are more likely to be inherited [Liu99] and [Koza94]. Even though the genetic algorithms may not be the most efficient algorithms for some problems, but it can find a globally optimal solutions when the evolution times approach infinity. Especially when the objective function has irregular shape, such as this problem, genetic algorithm is an effective approach.

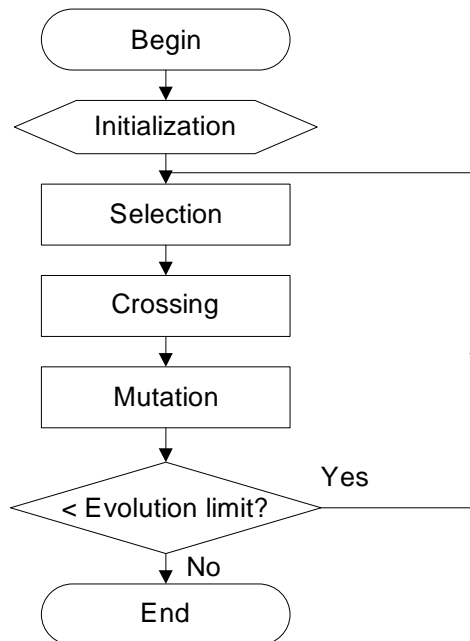


Figure 5.22 General Genetic Algorithm Flow Chart (adapted from [Liu99])

Generally speaking, genetic algorithms have two major parts, i.e., initialization part and evolution part. A general genetic algorithm flow chart, which is adapted from [Liu99], is shown in Figure 5.22. In the initialization stage, a group of N input argument vectors, V_i , $i=1\dots N$, are randomly selected such that they all satisfy the constraints. For a

second-order-section, an argument vector, V_i , equals $[c_1, c_2]$. The evolution part is an iteration of three actions, which are selection, crossing, and mutation.

In the selection process, the genes are ordered from maximum to minimum according to their objective function values. Then an evaluation function q_i for each gene is calculated as follows.

$$q_i = eval(V_i) = \sum_{j=1}^i alpha * (1 - alpha)^{j-1}, \text{ for } i = 1, 2, \dots, N. \quad (5.39)$$

Notation *alpha* could be any number between zero and one, in this study *alpha* is set to 0.1. Now a random number in the range of $(0, q_N]$ is generated. If the random number is between q_i and q_j , then V_j is selected to form a new group of genes. Repeating this step for N times, a new group of N genes are created. The computation complexity of selection is N multiplications and one addition.

Next the genes are under crossing process. A probability of crossing, Pc , is arbitrarily selected, for instance we can set Pc equal to 0.2. Then N random numbers of r_i in the range of $[0, 1]$ are generated. If r_i is less than Pc , then V_i is selected for crossing. The selected genes are randomly paired up. If the number of the selected genes is odd, one gene is simply ignored. If the pair of selected genes are V_i and V_j , after crossing the new genes V_i' and V_j' are created as

$$V_i' = g * V_i + (1 - g) * V_j \quad (5.40)$$

$$V_j' = (1 - g) * V_i + g * V_j \quad (5.41)$$

The notation g is a random number between 0 and 1. Then new genes must satisfy the constraints in equation (5.37). If not, random number g should be regenerated until the new genes are inside the constrained area. After all the pairs of genes are crossed, the crossing process is finished. The computation complexity of crossing is $2N$ multiplications and $(2N+1)$ additions.

Similar to crossing process, in mutation process, a probability of mutation, P_m , should be determined in advance. For in stance, we can choose P_m equal to 0.8. Then N random numbers, r_i , are generated. If r_i is not greater than P_m , then V_i is updated by

$$V_i = V_i + M_L * d \quad (5.42)$$

Notation M_L is a randomly generated step length, and d is also a randomly selected direction. The rule of thumb here is that the selection of M_L and d must make the new V_i inside the constrained area. The complexity of mutation is N multiplications and N additions.

So far one cycle of evolution is finished. The evolution cycle is repeated until either the number limit of evolution is reached or the optimum is within the range of tolerance. The overall computation complexity of $N_{Evolution}$ times of evolution is $4N * N_{Evolution}$ multiplications and $(3N + 2) * N_{Evolution}$ additions.

When the number of genes in one evolution is set to 100, and the limit of evolution times is set to 50, the convergence of the optimized correlation vs. the evolution times is demonstrated in Figure 5.23. After about twenty times of evolution, the optimum is approached. The genetic algorithm is therefore a reasonably efficient means to solve pulse optimizer problem.

The 1-SOS pulse optimizer transfer function, which is calculated using the above genetic algorithms, is

$$H_p(z) = \frac{0.9386 - 0.9715z^{-1} + z^{-2}}{1 - 0.9715z^{-1} + 0.9386z^{-2}} \quad (5.43)$$

The pulse optimizer calculated by the genetic algorithms using two SOSs is

$$H_p(z) = \frac{0.8 - 0.9z^{-1} + z^{-2}}{1 - 0.9z^{-1} + 0.8z^{-2}} \cdot \frac{0.9 - 0.95z^{-1} + z^{-2}}{1 - 0.95z^{-1} + 0.9z^{-2}} \quad (5.44)$$

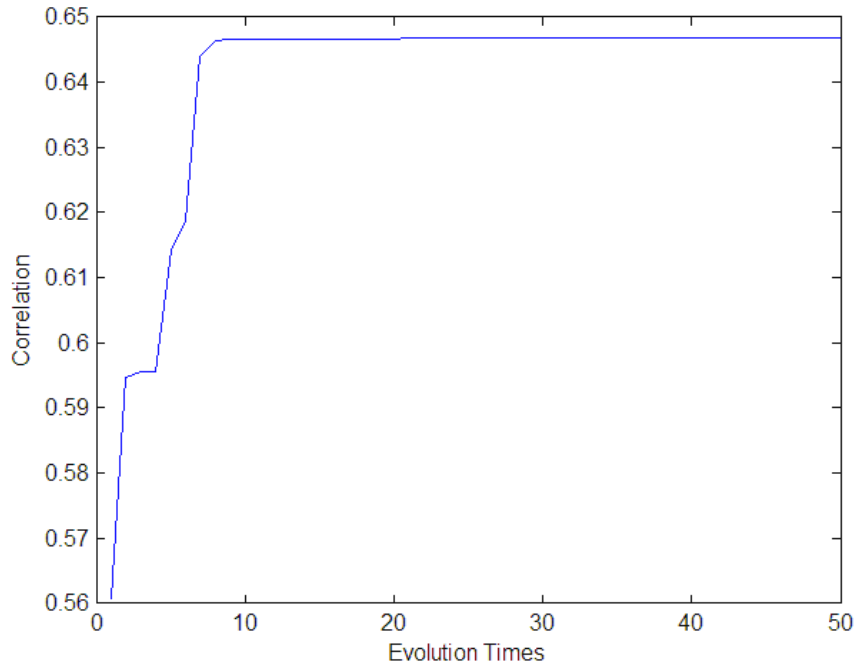


Figure 5.23 Convergence Process of Optimized Correlation vs. Evolution Times

The correlation values of the received signals with two band pass filters only, with two band pass filters and time-reversal implementation, with two band pass filters and a delay equalizer, with two band pass filters and a 1-SOS pulse optimizer, with two band pass filters and a 2-SOS pulse optimizer, are compared in Table 5.4. The time reversal implementation and delay equalizer don't improve the correlation peak value, in other words they are of little use in improving the correlation values. The 1-SOS pulse optimizer improves the correlation by 1.47 dB comparing to the correlation with two band pass filters only. The improvement of 2-SOS pulse optimizer over 1-SOS pulse optimizer is not very much, only 0.06dB.

Table 5.4 Correlation Comparison for Different Types of Filters

	Two Band-pass Filters Only	With Time Reversal	With Delay Equalizer	With 1-SOS Optimizer	With 2-SOS Optimizer
Correlation	0.5461	0.4322	0.3113	0.6468	0.6513

So far the procedure of an optimal digital pulse optimizer has been devised. However, in practice, an analogue implementation is more economical and convenient. The bilinear transform, also named as Tustin and Trapezoidal transform, can be used to convert digital filter to analogue filter [Amba99] [Bahe90]. The bilinear transform can be derived from the basic fact, i.e.,

$$z = e^{sT} = \frac{e^{sT/2}}{e^{-sT/2}} \quad (5.45)$$

In equation (5.45), the symbol T denotes the sampling period. The exponential terms are further expanded with first order Taylor expansion and equation (5.45) turns to be

$$z = \frac{1 + \frac{sT}{2}}{1 - \frac{sT}{2}} \quad (5.46)$$

With bilinear transform, the 1-SOS pulse optimizer of equation (5.43) is transformed into analogue filter, i.e.,

$$H_b(s) = \frac{2.91s^2 - 1.227s + 9671}{2.91s^2 + 1.227s + 9671} \quad (5.47)$$

Another method to convert a digital filter to an analog filter is Pade polynomial approximation transform. By Pade polynomial approximation [PrTe95] and [Wong92], the transformed analogue filter of the 1-SOS pulse optimizer is calculated as

$$H_{pn}(s) = \frac{1.075 * 10^{-9} s^4 - 4.09 * 10^{-8} s^3 + 3.555 * 10^{-4} s^2 - 1.227 * 10^{-3} s + 0.9671}{1.075 * 10^{-9} s^4 + 4.09 * 10^{-8} s^3 + 3.555 * 10^{-4} s^2 + 1.227 * 10^{-3} s + 0.9671} \quad (5.48)$$

In the two analogue filters of equations (5.47) and (5.48), the coefficients of even order terms in both numerators and denominators are the same and the coefficients of odd order terms in the numerators are the opposite of those in the denominators. It is easy to verify that the amplitude responses of the two analogue filters are all pass, i.e., $|H(jw)|$ is always equal to unit.

However, the phase responses of the two analogue filters are different, as shown in Figure 5.24. Through bilinear transform, the order of the analogue filter is the same as

the order of the digital filter. Through Pade polynomial approximation, the order of the analogue filter is usually higher than that of the digital filter. The higher the order of Pade polynomial is, the closer the analogue filter phase response is to the digital filter phase response. As shown in Figure 5.24, the phase response of the 4-th order analogue filter with Pade polynomial approximation transform is almost the same as the digital filter phase response, while the phase response of the analogue filter by bilinear transform has a visible shift from that of the digital filter.

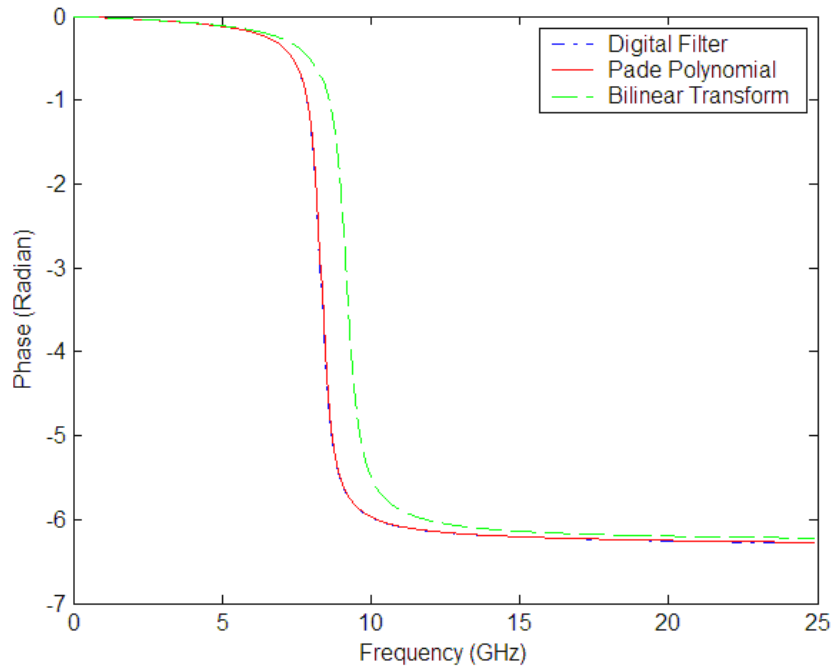


Figure 5.24 Comparison of Different Transform Methods in Terms of Phase Response

5.5.1 The Effect of Time Offset

With the 1-SOS pulse optimizer, the receiver output SNR can be calculated as equation (5.36). The effect of receiver time offset on SNR is plotted in Figure 5.25. A 25 pico

second time offset may degrade the receiver SNR by 20 dB. So UWB receiver is quite sensitive to the time offset.

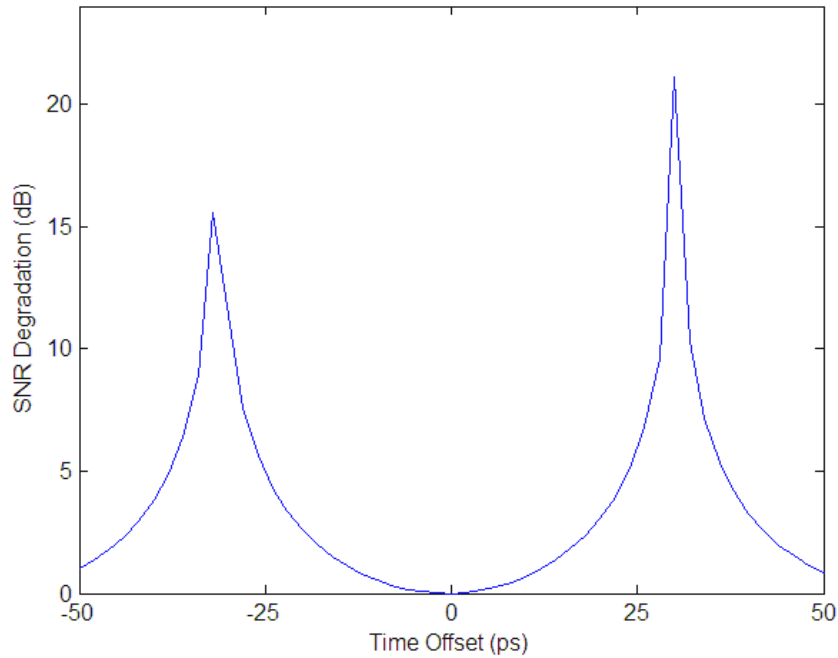


Figure 5.25 The Effect of Time Offset On SNR

5.5.2 The Effect of Frequency Offset

The receiving template frequency offset has modest effect on UWB receiver SNR. Figure 5.26 demonstrates the relationship between SNR degradation and frequency offset. A frequency offset of 100 MHz may degrade the SNR by only 0.1 dB. It seems that the UWB receiver is insensitive to the frequency offset. In other words, the requirement for the receiving template frequency offset in UWB systems is relatively low, and the building cost of such receiving template is also inexpensive.

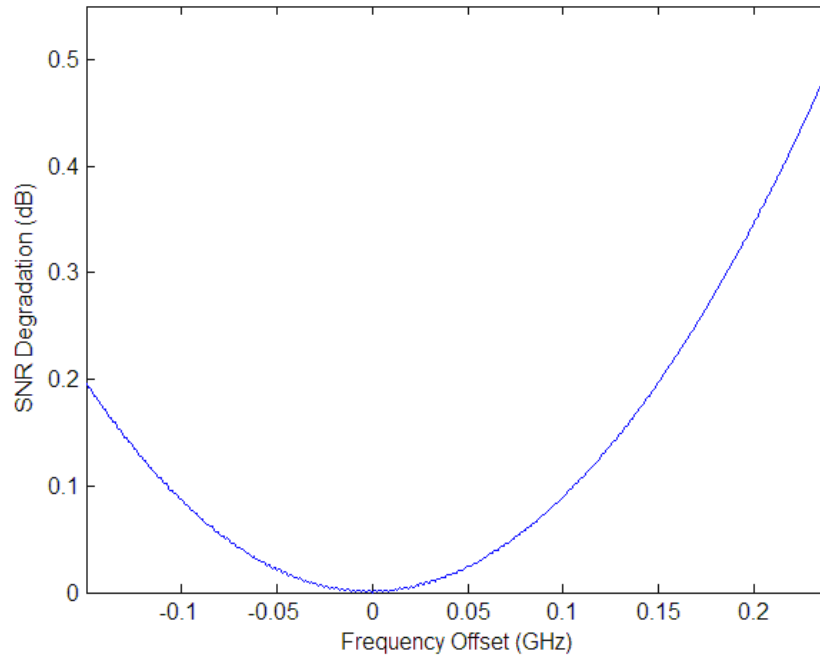


Figure 5.26 The Effect of Receiving Template Frequency Offset

5.6 Conclusions

In UWB communication systems, pulse-shaping filters are often used to control the interferences of UWB receivers to legacy narrowband systems. An elliptic band-pass pulse shaping filter design procedure has been studied in both analogue and digital forms. Limit cycles can be effectively removed using state space method in the analog elliptic filter design. The nonlinear phase of the elliptic band pass filter can be equalized with delay equalizer.

For time-limited sinusoidal template UWB receivers, a pulse shape optimizer design procedure is proposed to maximize the SNR of the received signal. The pulse shape optimizer is basically an all-pass filter, whose coefficients are designed to maximize the SNR. Through simulation study, it turns out that a second-order pulse shape optimizer

is the most efficient choice in terms of SNR maximization. Higher order pulse shape optimizers won't improve the SNR significantly. With fixed pulse optimizer, UWB receivers are quite sensitive to time offset, but are relatively insensitive to frequency offset.

6 UWB Interferences to C-band Satellite Receivers

The interference between UWB devices and the existing narrowband transceivers has drawn tremendous research attention recently. Most of the UWB interference research can be grouped into two categories. The first category of research concentrates on the interference from UWB devices to the existing narrowband transceivers, and the second category of research focus on the interference from the existing narrowband transceivers to UWB devices.

Since UWB devices transmit power over a large frequency band, UWB signals may intentionally or unintentionally interfere with narrowband devices such as wireless phones, GPS receivers, aeronautical communications, and wireless LAN, etc. [Foer02b] described a modeling method of UWB interferences on narrowband systems. [MoFr05] proposed a software approach to access UWB interference on GPS receivers. [UhMa04] studied the interferences of UWB signals on Galileo receivers. [HaHo01] investigated

the interferences of different kinds of UWB signals on UMTS/WCDMA devices. [LaFi04] talked about the UWB interference to GSM receivers. The UWB Interferences on wireless LAN devices were investigated in [ToOg03] and [ChOh03]. [ElMa04] analyzed the UWB interferences on aeronautical radios. [WiWe02] illustrated the UWB interference effects on amateur radio receivers.

On the other hand, narrow band signals may also interfere with UWB receivers. Since UWB receiver need to collect the energy through a wide frequency range, high power narrow band radios can easily saturate UWB receivers' front end. This makes UWB devices vulnerable to high power narrow band interferences. [WaWa03] investigated the interference power of narrowband jamming signal on UWB system. [ChSt02], [Foer02b] and [IaBe02] analyzed the performance of UWB spread spectrum communications under narrow band interferences. [HaTe02] examined the UWB performance under interferences from UMTS. [McBu02] proposed a narrow band rejection system for UWB communications on the basis of least mean square (LMS) method. Wireless LAN interferences on UWB devices were discussed in [FiPr03].

However, not much research has been found in the area of UWB interference to C-band satellite receivers. Satellite communications are often used to convey important information such as governmental and military video, voice and data, aeronautical and maritime voice and data, etc. International Maritime Satellite (INMARSAT) communication system, which is widely used by shippers, aircrafts, and land mobile users all over the world, uses C-band receivers at land earth station. It is very important that the UWB communication systems would not interfere with these C-band receivers. This chapter is devoted to the investigation of UWB interference to C-band satellite receivers.

The rest of this chapter is organized as follows. Section 6.1 gives an overview of C-band satellite receivers and UWB devices. Section 6.2 talks about the regulations on UWB devices and derives some preliminary separation distance requirements between

UWB devices and C-band satellite receivers. Section 6.3 analyzes the power spectrum of general UWB signals. Section 6.4 investigates the performance degradation of C-Band receiver due to UWB Interferences. Finally, Section 6.5 summarizes the findings and concludes this chapter.

6.1 C-band Receivers and UWB devices Overview

An exemplar satellite forward and reverse link diagram is shown in Figure 6.1. In the forward link, the land earth station transmits the control and data messages to the satellite using 6 GHz C-band. The satellite receives the coming-up land earth station signals in 6 GHz, down-converts them into 1.5 GHz L-band, and transmits the signal down to the mobile earth station. In the reverse link, the mobile earth station (MES) transmits control and data messages to satellite using 1.6 GHz L band. The satellite receives the 1.6 GHz L band signals, up-converts them to 4 GHz C-band, and then transmits the signal down to the land earth station (LES). In the reverse link, the LES receiver is vulnerable to the interference from UWB devices. An exemplar reverse link budget is listed in Table 6.1. In general, the C-band receivers have a link margin of about 2 dB, which can also be considered as the interference tolerance boundary of the receivers.

The FCC regulation requires that the UWB signals should use the frequency bandwidth from 3.1 GHz to 10.6 GHz only and the transmission power density must be below -41.3 dBm/MHz. Both of the two current UWB IEEE 802.15.3a proposals satisfy the FCC rules.

The first proposal [FiKo04], which is proposed by XtremeSpectrum and Motorola, is based upon direct sequence (DS) pulse position modulated pulses. In this proposal, the whole UWB bandwidth is divided into two sub-bands. The low sub-band is from 3.1 GHz to 5.15 GHz and the high sub-band is from 5.825 GHz to 10.6 GHz. So totally

three kinds of pulses, which can be generated in the system, are long pulses, mid pulses, and short pulses. The long pulse only uses the low band, the mid pulse only uses the high band, and the short pulse uses both the low band and the high band.

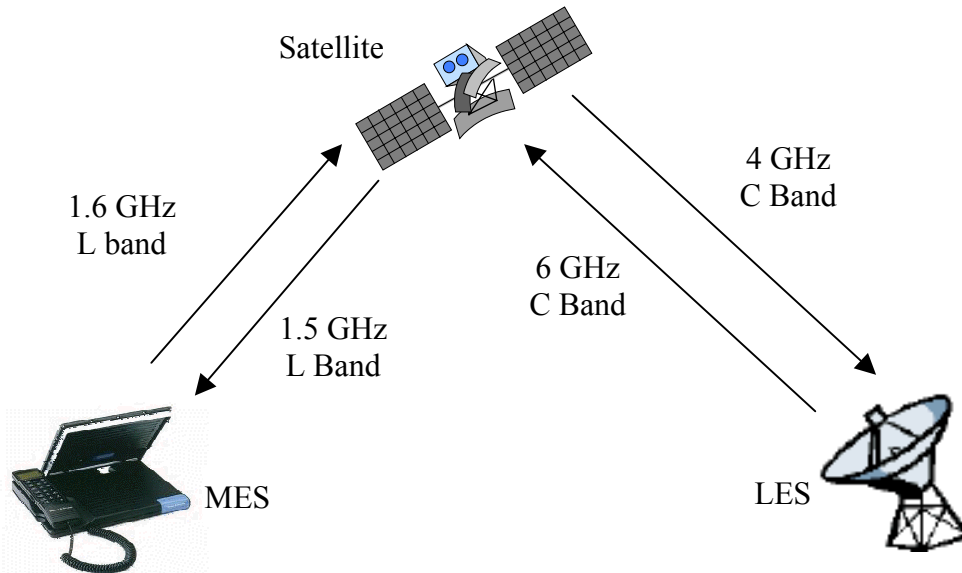


Figure 6.1 The Satellite Forward and Reverse-Link Overview

The second UWB proposal [MuOF04], which was originally proposed by Intel and TI, employs the multi-band OFDM modulation technique, and it is also called MB-OFDM proposal. In this proposal, the whole UWB frequency bandwidth is divided into 13 bands, each of which is of 528 MHz wide. These 13 bands are further grouped into 4 distinct groups, i.e., Group A, Group B, Group C, and Group D. As shown in Figure 6.3, Group A (3.1 – 4.9 GHz) has 3 bands and is intended for the 1st generation devices. Group B (4.9 – 6.0 GHz) has two bands and is reserved for future use. Group C (6.0 – 8.1 GHz) has 4 bands and is intended for devices with improved performance. Group D (8.1 – 10.6 GHz) also has 4 bands and is reserved for future use.

Both of the UWB proposals don't use the frequency band below 3.1 GHz. Although the UWB devices could have unintentional interference to L-band receivers, they won't intentionally interfere with the L-band mobile earth receiver. However, the 4 GHz C-band is used by both C-band receiver and UWB devices. UWB devices will interfere

with the return link communication at the land earth station. The interference effect from UWB devices to C-band LES receivers will be the focus of the following sections in this chapter.

Table 6.1 An Exemplar C-Band Receiver Reverse-Link Budget

MES EIRP	23 dBW (1.6 GHz)
Path loss (23k miles)	-189 dB
Absorption loss	-0.5 dB
Satellite G/T	-2.5 dB/K
Mean up-path C/N0	60 dBHz
Satellite C/IM0	69 dBHz
Transponder Gain	168 dB
Satellite EIRP	1.5 dBW (4 GHz)
Path loss	-197 dB
Absorption loss	-0.5 dB
LES G/T	30 dB/K
Down-path C/N0	63 dBHz
Interference loss	-1.6 dB
Total random loss (99%)	-2 dB
Overall C/N0	56 dBHz
Margin	2 dB

6.2 Separation Distance between UWB Devices and C-band Receivers

The FCC rules on the UWB signals are that the UWB emission power should be less than -41.3 dBm/MHz and the UWB signal frequency band should limit in the range from 3.1 GHz to 10.6GHz. If a UWB device is placed nearby a C-band receiver, the signal power emitted by the UWB device could potentially interfere with the C-band signal. This interference diagram is demonstrated in Figure 6.2.

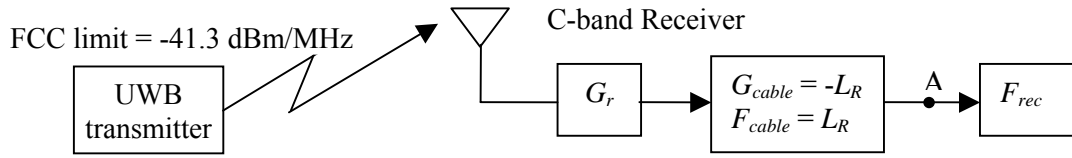


Figure 6.2 UWB Interference to C-band Receivers

The C-band receiver antenna gain to the UWB signal is denoted by G_r , the loss due to the cable running from C-band antenna to the receiver is L_R , the noise figure of the passive cable is also L_R , and the noise figure of the C-band receiver is denoted by F_{rec} .

The C-band antenna gain to the UWB signal can be generally expressed as

$$G_r = p * q * G(\theta, \phi) \quad (6.1)$$

where p = polarization efficiency, $0 \leq p \leq 1$

q = impedance mismatch factor, $0 \leq q \leq 1$

θ = elevation angle

ϕ = azimuth angle

$G(\theta, \phi)$ = C-band receiver antenna gain pattern

Since C-band receiver antenna is a high-gain directional antenna, the antenna gain in different direction is different. In the following calculation, we assume that the interferer is inside the main lobe of the antenna and a nominal gain value of 30 dB is adopted for the sake of illustration. For gain values other than 30 dB, the required path loss can be easily calculated following the same logic. It is well known that the general power spectrum of a modulated UWB signal consists of continuous part and discrete lines [Proa03]. When the UWB devices emit only random-like noise so that its power spectrum has continuous term only, the received interference power density N_r at receiver input point A can be expressed as

$$N_r = N_T - PL + G_r - L_R \quad (6.2)$$

where

N_T = UWB device emission noise power density, -41.3 dBm/MHz

PL = path loss

G_r = receiver antenna gain, 30 dB

L_R = cable loss, 3 dB

For random UWB noise emission, the tolerable received noise floor is

$$N_r = 10 \times \log(10^{Mgn/10} - 1) + N_s = N_T + MEF - PL + G_r - L_R \quad (6.3)$$

where

N_s = system noise density, -156 dBm/Hz

Mgn = C-band receiver margin, 2 dB

MEF = multiple equipment factor, 0 dB if only one device is used.

Multiple equipment factor is also the number of active UWB devices in dB, i.e., $MEF = \log_{10}(\text{number of UWB devices})$. After some manipulation of equation (6.3), the required path loss of UWB interference is

$$PL = -10 \times \log(10^{Mgn/10} - 1) - N_s + N_T + MEF + G_r - L_R \quad (6.4)$$

In line-of-sight (LOS) channel environment, the path loss of UWB signal at distance d from the transmitter can be expressed as [BeGi04]

$$PL(d) = 47 + 17 \log(d) \quad (6.5)$$

Substituting equation (6.5) into equation (6.4) and plugging all the corresponding numbers into equation (6.4), we have

$$47 + 17 \log(d) = -10 \times \log(10^{2.1/10} - 1) + 156 - 101.3 + 30 - 3 \quad (6.6)$$

The solution of equation (6.6) is $d = 144\text{m}$. In LOS channel environment, the UWB device should be at least 144 m away from the C-band satellite receivers in order not to interfere with satellite signals.

In non-line-of-sight (NLOS) channel environments, the path loss of UWB signal at distance d from the transmitter is expressed as [BeGi04]

$$PL(d) = 51 + 35 \log(d) \quad (6.7)$$

Substituting equation (6.7) into equation (6.4) and plugging in all the corresponding numbers, equation (6.8) is derived.

$$51 + 35 \log(d) = -10 \times \log(10^{2.1/10} - 1) + 156 - 101.3 + 30 - 3 \quad (6.8)$$

The solution of this equation is $d = 9$ m. In NLOS channel environment, if the power spectrum of UWB emission has only continuous part, the UWB device should be at least 9 m away from the C-band satellite receivers in order not to interfere with satellite receivers.

On the other hand, if the power spectrum of UWB signals has discrete lines and a very strong discrete line happens to collide with the return link C-band satellite signal, the single tone interference effect of UWB signal is dominant. Under the worst case when UWB devices emit no random noise and only one single tone per MHz bandwidth in the C-band and assuming the FCC emission limit applies to the single tone emission, the maximal transmitted single tone energy per symbol period E_T is:

$$E_T = P_{CW} T_s = N_T * \frac{\text{Measurement_BW}}{\text{Symbol_Rate}} = N_T + BWRG \quad (6.9)$$

where P_{CW} = the single tone power

T_s = the C-band receiver symbol period, 29.8 μ s

Measurement_BW = FCC test measurement bandwidth, 1 MHz

Symbol_Rate = symbol rate, 33.6 kHz

$BWRG$ is defined as the FCC test measurement bandwidth to C-band receiver channel bandwidth ratio gain, i.e.,

$$BWRG = \begin{cases} 10 * \log\left(\frac{\text{Measurement_BW}}{\text{Symbol_Rate}}\right) & \text{Measurement_BW} > \text{Symbol_Rate} \\ 0 \text{ dB} & \text{Measurement_BW} \leq \text{Symbol_Rate} \end{cases} \quad (6.10)$$

Substituting all corresponding numbers into the equation (6.10), $BWRG$ is calculated as $BWRG = 14.7$ dB.

In the worst case, the maximal received single tone energy per symbol period E_r becomes

$$E_r = E_T - PL + G_r - L_R = N_T + BWRG - PL + G_r - L_R \quad (6.11)$$

For single tone emission only, we have

$$N_r = 10 \times \log(10^{M_{gn}/10} - 1) + N_s = N_T + BWRG + MEF - PL + G_r - L_R \quad (6.12)$$

If the narrow band receiver uses high order modulation types, such as QPSK, D8PSK, or QAM, the single tone interference can be roughly approximated as Gaussian noise with equivalent noise density. In LOS channel environment and assuming only one UWB device is inside antenna main lobe of the C-band receiver, equation (6.13) is derived by plugging all the corresponding parameters into equation (6.12).

$$47 + 17 \log(d) = -10 \times \log(10^{2.1/10} - 1) + 156 - 101.3 + 14.7 + 30 - 3 \quad (6.13)$$

The solution of the above equation is $d = 1060$ m. In LOS channel environment and when single tone UWB interference is dominant, the UWB device should be 1060 m away from the C-band receiver in order not to degrade its performance.

In NLOS channel environment and assuming only one UWB device is inside antenna main lobe of the C-band receiver, we have

$$51 + 35 \log(d) = -10 \times \log(10^{2.1/10} - 1) + 156 - 101.3 + 14.7 + 30 - 3 \quad (6.14)$$

The solution of this equation is $d = 23$ m. In NLOS channel environment and when single tone UWB interference is dominant, the UWB device should be 23 m away from the C-band receiver in order not to degrade the C-band receiver's performance.

6.3 Power Spectral Density of UWB signals

The power spectra of UWB signals are very important in analyzing the UWB interference to narrow band receivers. This section studies the power spectrum of

general UWB signals. If an individual UWB pulse shape is denoted by $p(t)$, then a general UWB signal $s(t)$ can be expressed as [Pako03]

$$s(t) = p(t) \otimes \sum_k a_k \delta(t - T_k) \quad (6.15)$$

The data information, which is embedded in a sequence of pulses $\delta(t)$ with variant amplitude a_k and/or variant time position T_k can be formulated as

$$d(t) = \sum_k a_k \delta(t - T_k) \quad (6.16)$$

Let $S_d(f)$ denote the power spectrum of $d(t)$, then the power spectrum of $s(t)$ can be expressed as

$$S_s(f) = |P(f)|^2 S_d(f) \quad (6.17)$$

where $P(f)$ is the Fourier transform of the UWB pulse $p(t)$.

In general, UWB signals are usually assumed to be cyclostationary, i.e.,

$$s(t) = s(t + T_L) \quad (6.18)$$

Notation T_L denotes the cyclostationary period of the UWB signal. The autocorrelation of $s(t)$ is also cyclostationary, i.e.,

$$R_s(t + \tau, t) = R_s(t + T_L + \tau, t + T_L) \quad (6.19)$$

The average of $R_s(t + \tau, t)$ can be calculated as

$$\bar{R}_s(\tau) = \frac{1}{T_L} \int_0^{T_L} R_s(t + \tau, t) dt \quad (6.20)$$

The power spectrum of $s(t)$ is defined as the Fourier transform of the average autocorrelation of the signal, i.e.,

$$S_s(f) = \int_{-\infty}^{\infty} \bar{R}_s(\tau) e^{-j2\pi f\tau} d\tau \quad (6.21)$$

By the same logic, the power spectrum of $d(t)$ can also be expressed in terms of average Fourier transform of its autocorrelation, i.e.,

$$S_d(f) = \frac{1}{T_L} \sum_l R_\gamma(l) \quad (6.22)$$

where $\gamma_k(f) = a_k e^{-j2\pi f T_k}$,

$$R_\gamma(l) = \langle \gamma_k(f) \gamma_{k+l}^*(f) \rangle.$$

Notation $\langle \bullet \rangle$ denotes the time average operation. The power spectrum $S_s(f)$ turns out to be

$$S_s(f) = |P(f)|^2 \frac{1}{T} \sum_l R_\gamma(l) \quad (6.23)$$

In general time hopping UWB systems, let T_k represent the time position of the k -th pulse, let T_f denote the UWB signal frame duration, and let ε_k designate the time dithering of the k -th pulse. Then we have

$$T_k = kT_f + \varepsilon_k \quad (6.24)$$

and

$$\gamma_k(f) = a_k e^{-j2\pi f \varepsilon_k} e^{-j2\pi f k T_f} \quad (6.25)$$

A new variable $c_k(f)$ is defined as

$$c_k(f) = a_k e^{-j2\pi f \varepsilon_k} \quad (6.26)$$

Then the correlation $R_\gamma(l)$ can be expressed as

$$R_\gamma(l) = \langle c_k(f) c_{k+l}^*(f) \rangle \quad (6.27)$$

Let $\mu_c(f)$ denote the mean of $c_k(f)$, and $\sigma_c^2(f)$ represent the variance of $c_k(f)$, then equation (6.27) is equivalent to equation (6.28).

$$R_\gamma(l) = |\mu_c(f)|^2 + \sigma_c^2(f) \delta(l) \quad (6.28)$$

The power spectrum $S_s(f)$ becomes [PaKo03]

$$S_s(f) = |P(f)|^2 \left\{ \frac{\sigma_c^2(f)}{T_f} + \frac{|\mu_c(f)|^2}{T_f^2} \sum_k \delta\left(f - \frac{k}{T_f}\right) \right\} \quad (6.29)$$

The power spectrum of UWB signal is generally composed of two parts. The first part is the continuous term, i.e., $|P(f)|^2 \frac{\sigma_c^2(f)}{T_f}$, and the second part is the discrete term, i.e.,

$|P(f)|^2 \frac{|\mu_c(f)|^2}{T_f^2} \sum_k \delta\left(f - \frac{k}{T_f}\right)$. The continuous part always exists, while the discrete

lines in the power spectrum may disappear when the mean of $c_k(f)$, i.e., $\mu_c(f)$, is equal to zero.

In direct sequence time-hopping pulse position modulation (DS-TH-PPM) UWB systems, the transmitted signal is

$$s(t) = \sum_{i=0}^{\infty} \sum_{j=0}^{N_s-1} \delta(t - jT_f - c_j T_c - iT_b - b_i \Delta) \otimes p(t) \quad (6.30)$$

Let us define a new signal $v(t)$ as

$$v(t) = \sum_{j=0}^{N_s-1} \delta(t - jT_f - \eta_j) \otimes p(t) \quad (6.31)$$

The power spectrum of $v(t)$ is

$$P_v(f) = P(f) \sum_{m=0}^{N_s-1} e^{-j(2\pi f(mT_f + \eta_m))} \quad (6.32)$$

The original UWB TH-PPM signal turns out to be

$$s(t) = \sum_{i=0}^{\infty} v(t - iT_b - \Delta b_i) \quad (6.33)$$

When symbols 0 and 1 are equiprobable, the transmitted signal power spectrum [BeGi04] is

$$S(f) = \frac{|P_v(f)|^2}{T_b} \left[1 - |W(f)|^2 + \frac{|W(f)|^2}{T_b} \sum_{n=0}^{\infty} \delta\left(f - \frac{n}{T_b}\right) \right], \quad (6.34)$$

where

$$|W(f)|^2 = \frac{1}{2}(1 + \cos(2\pi f\Delta)). \quad (6.35)$$

It can be seen from equation (6.34) that the power spectral density of DS-PPM UWB signals also has both continuous and discrete components.

The continuous and discrete components in the power spectrum of UWB signals can be further demonstrated with the following simulation [BeGi04]. In this simulation, a Gaussian doublet pulse is employed as a basic pulse, whose time domain function is

$$p(t) = \left[1 - 4\pi \left(\frac{t}{\tau} \right)^2 \right] e^{-2\pi \left(\frac{t}{\tau} \right)^2} \quad (6.36)$$

The pulse shaping factor τ is set to 0.25 ns, the sampling rate is set to 50 GHz and the pulse duration is approximately 0.5 ns. The pulse shape in time domain is shown in Figure 6.3, while its Fourier transform is demonstrated in Figure 6.4.

If chip duration is set to 1 ns and the UWB signal has no PPM and no time hopping in each frame, i.e., a pulse is sent out every 1 ns periodically, the power spectrum of this pulse train consists of many uniformly distributed lines with an envelope the same as that of single pulse. It is worth to note that the power spectrum of the periodically transmitted pulse train is dominated by discrete lines, as shown in Figure 6.5.

If the frame period T_f is set to 3 ns, time shift Δ is set to 0.25 ns, and the number of pulses per bit N_s is set to 5, the hopping sequence c_j is generated by a m -sequence pseudo-random generator, the UWB signal power spectrum with PPM and time hopping is shown in Figure 6.6. The power spectrum of TH-PPM UWB signal has both discrete and continuous parts and the spectral envelope is similar to that of UWB signal without TH and PPM except that the envelope with TH-PPM is slightly lower than that with no TH and PPM. This is because that the discrete lines in the power spectrum of periodically transmitted pulse train are spread out by TH and PPM.

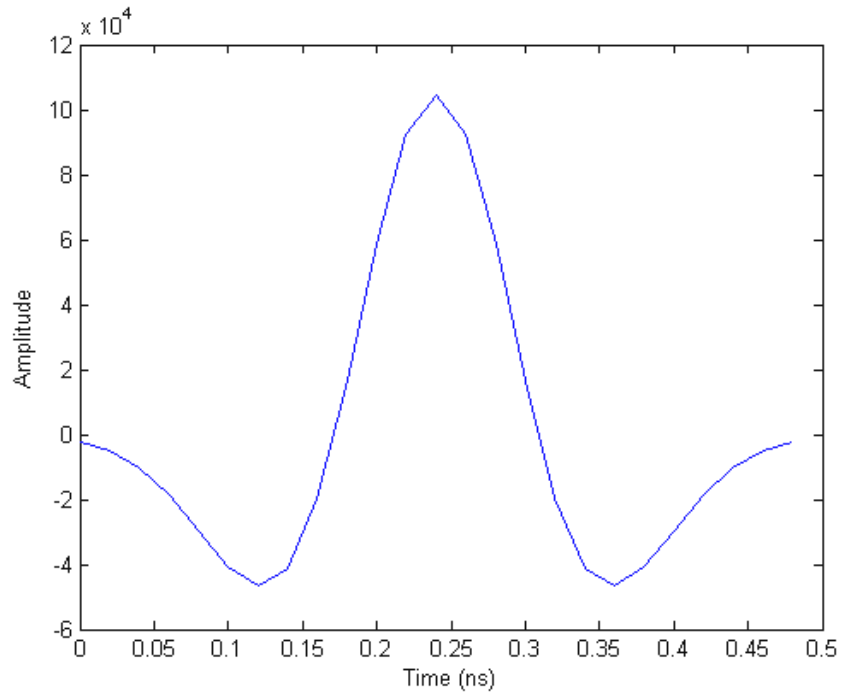


Figure 6.3 Gaussian Doublet Pulse in Time Domain

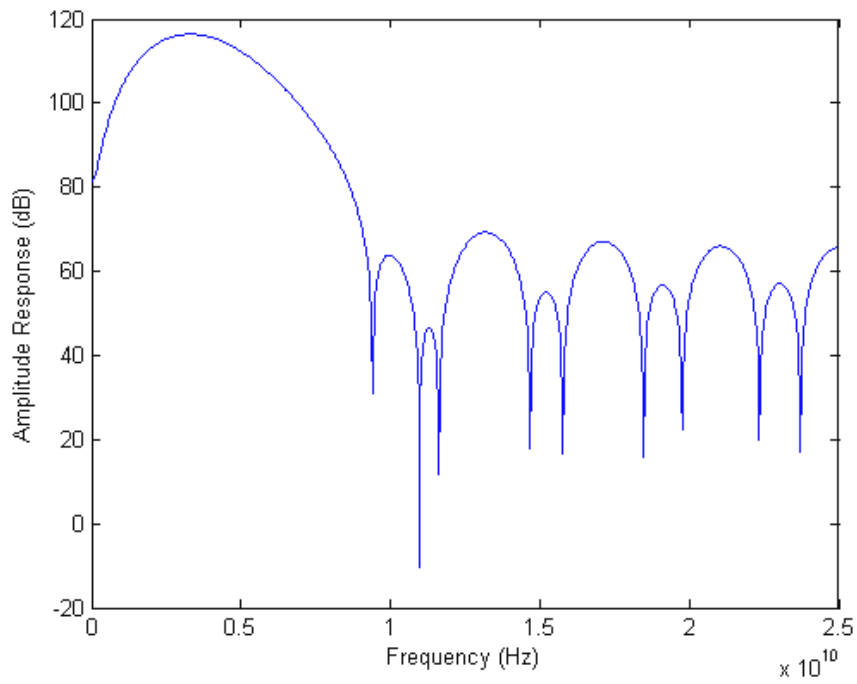


Figure 6.4 Gaussian Doublet Pulse in Frequency Domain

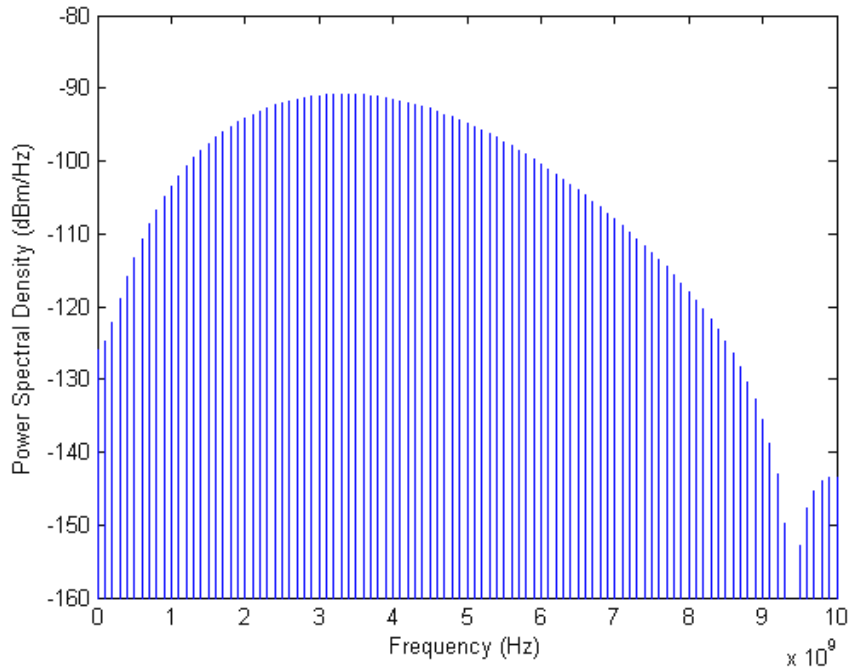


Figure 6.5 Power Spectrum of UWB Pulses without TH-PPM

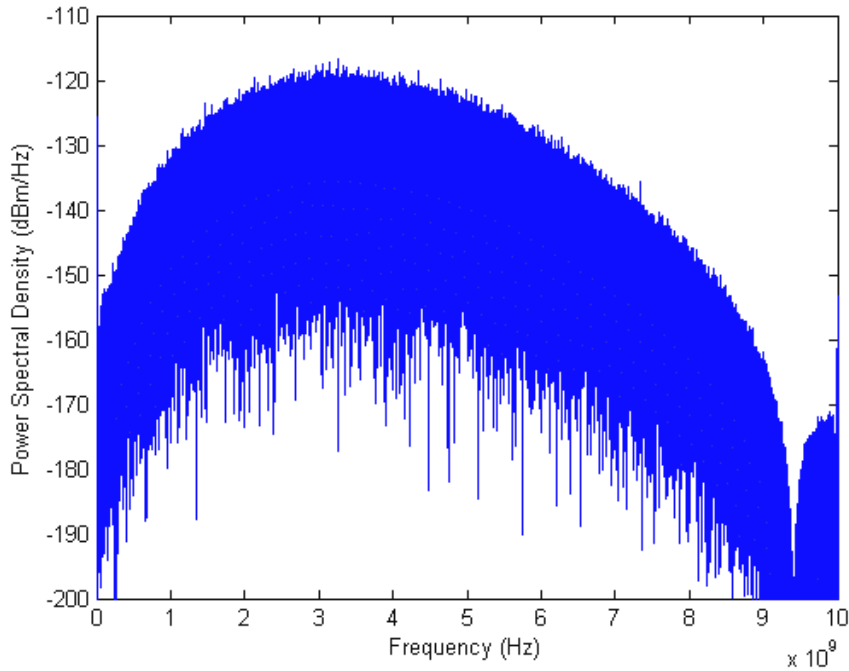


Figure 6.6 Power Spectrum of UWB Pulses with TH-PPM

The overall power spectrum of UWB signal is determined not only by the UWB pulse shape but also by its modulation scheme. With the same UWB pulse shape, randomized modulation scheme helps to reduce the overall power spectral level.

In summary, the power spectral density of general UWB signals consists of both continuous and discrete components. The discrete components can be reduced to certain level by randomizing the pulse modulation scheme.

6.4 C-Band Receiver Performance Degradation Due to UWB Interference

Since UWB devices share the bandwidth with C-band receivers, the interference of UWB devices to C-band receivers becomes an important research issue. The effect of UWB interference differs with the modulation and demodulation techniques used in the C-band transceivers. We will now only consider the UWB interference effects on a simple modulation, BPSK, to illustrate a novel analysis method in the rest of this section. The UWB interference effect to other more complicated modulation scheme can be derived following the same logic but with more complexity.

Since the UWB power spectrum generally has both discrete lines and continuous part, and since we have assumed that the UWB bandwidth is much larger than the narrowband signal/receiver of interest, the continuous part in the PSD of general UWB signals can be reasonably assumed to be constant in the frequency band of the narrowband receivers. The interference effect of the continuous part in the UWB PSD is equivalent to the effect of additive white Gaussian noise. The discrete lines in the UWB PSD are simply jamming tones to narrowband receivers. In a narrowband transceiver with BPSK modulation, the base band equivalent of the received signal mixed with UWB interference can be expressed as

$$r_i = A_s b_i + \sum_{j=1}^M A_j \cos \theta_j + z \quad (6.37)$$

where A_s = symbol amplitude

A_j = UWB jamming tone amplitude

θ_j = UWB jamming tone phase angle

z = additive white Gaussian noise with 0 mean and σ_z^2 variance

b_i = bipolar binary information bit, -1 or 1

M = number of discrete lines inside the receiving bandwidth

The noise term z consists of both thermal noise and random noise from UWB devices. There are totally M UWB jamming tones inside the C-band receiver frequency bandwidth, and for each jamming tone, the tone phase is

$$\theta_j = 2\pi(f_j - f_c) + \theta_{j0} \quad (6.38)$$

where f_j = the j -th jamming tone frequency

f_c = C-band receiver carrier frequency

θ_{j0} = initial phase of the j -th jamming tone.

To lie within the signal processing bandwidth, the difference between carrier frequency f_c and the jamming tone frequency f_j must be less than one half of symbol rate f_s , i.e., $|f_j - f_c| < f_s/2$. Otherwise, we can assume that the jamming tones lie outside the receiving bandwidth and will be significantly attenuated by RF front end and base band filters.

In general, the carrier frequency and the jamming tone frequency are not exactly the same, i.e., $f_j \neq f_c$, so the phase angle θ_j can be assumed to be uniformly distributed in the interval $(-\pi, \pi)$. The probability density function of θ_j can be expressed as

$$f_{\theta_j}(\theta_j) = \begin{cases} \frac{1}{2\pi} & |\theta_j| < \pi \\ 0 & |\theta_j| > \pi \end{cases} \quad (6.39)$$

Let us define a new random variable Y as $y = A_j \cos \theta_j$. From [Papo65], the probability density function of Y is

$$f_Y(y) = \begin{cases} \frac{1}{\pi \sqrt{A_j^2 - y^2}} & |y| < A_j \\ 0 & |y| \geq A_j \end{cases} \quad (6.40)$$

When $A_j = 1$, the curve of $f_Y(y)$ is plotted in Figure 6.7. The characteristic function $\Psi_Y(w)$ of $f_Y(y)$ is

$$\Psi_Y(w) = \int_{-\pi}^{\pi} \frac{1}{\pi \sqrt{A_j^2 - y^2}} \exp(jwy) dy = I_0(A_j w) \quad (6.41)$$

The function $I_0(\cdot)$ is the zero-order Bessel function of first kind.

Since the mean of the random variable Z , which represents the noise term in equation (6.37), is zero, i.e., $\mu_z = 0$, the probability density function of random variable Z is

$$f_Z(z) = \frac{1}{\sqrt{2\pi}\sigma_z} e^{-\frac{z^2}{2\sigma_z^2}} \quad (6.42)$$

When $\sigma_z = 1$, the curve of $f_Z(z)$ is plotted in Figure 6.8. The characteristic function of $f_Z(z)$ is

$$\Psi_Z(w) = \exp\left(jw\mu_z - \frac{1}{2}w^2\sigma_z^2\right) = \exp\left(-\frac{1}{2}w^2\sigma_z^2\right) \quad (6.43)$$

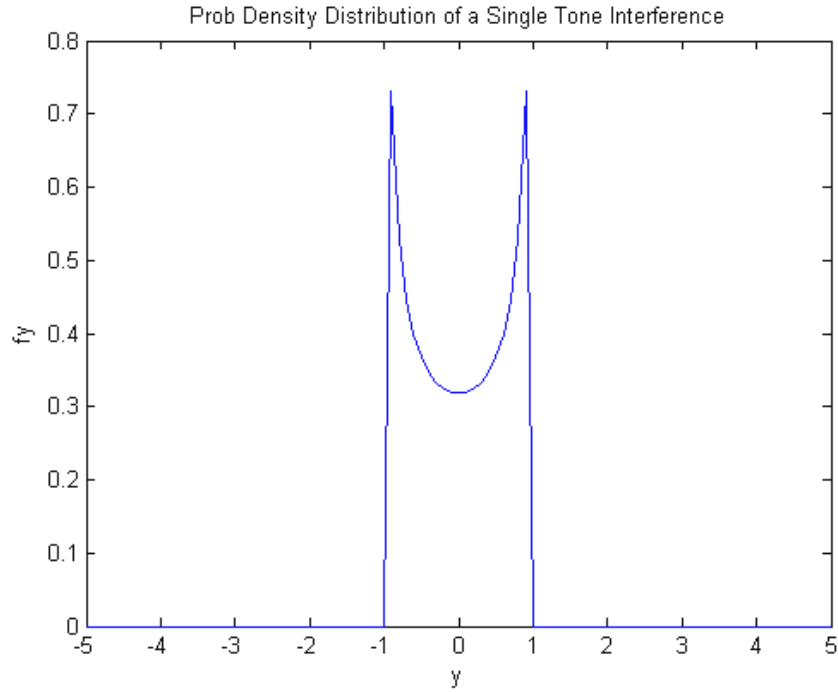


Figure 6.7 Probability Density Distribution of Single Tone Interference

Now denote the sum of y and z as a new random variable x , i.e.,

$$x = y + z \quad (6.44)$$

Variable x represents the overall interference and noise, i.e., UWB jamming tone interference, UWB additive white Gaussian interference, and narrowband receiver thermal noise. Since random variables Y and Z are independent, the probability density function of X is the convolution of the probability density functions of Y and Z .

$$f_X(x) = \int_{-\infty}^{\infty} f_Z(x-y)f_Y(y)dy \quad (6.45)$$

Substituting equation (6.42) and (6.44) into equation (6.45), we get

$$f_X(x) = \int_{-A_j}^{A_j} \frac{1}{\sqrt{2\pi\sigma_z}} e^{-\frac{(x-y)^2}{2\sigma_z^2}} \frac{1}{\pi\sqrt{A_j^2 - y^2}} dy \quad (6.46)$$

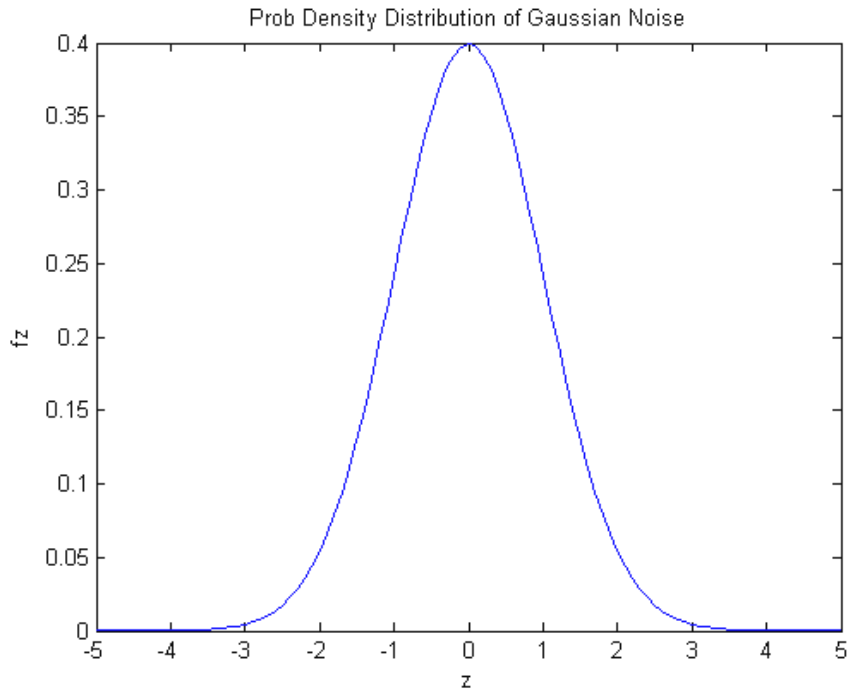


Figure 6.8 Probability Density Distribution of Gaussian Noise

When $A_j = 1$ and $\sigma_z = 1$, the curve of $f_x(x)$ is plotted in Figure 6.9. The close-form of equation (6.46) is quite clumsy to calculate, so the characteristic function of $f_x(x)$ is explored. The characteristic function of $f_x(x)$ is equal to the product of the characteristic functions of $f_y(y)$ and $f_z(z)$, i.e.,

$$\Psi_x(w) = \Psi_y(w)\Psi_z(w) \quad (6.47)$$

Substituting equation (6.41) and (6.43) into equation (6.47), we get

$$\Psi_x(w) = \exp\left(-\frac{1}{2}w^2\sigma_z^2\right)I_0(A_jw) \quad (6.48)$$

The cumulative probability distribution function (CDF) of random variable X [Papo65] is

$$F_x(x) = \frac{1}{2} + \frac{1}{\pi} \int_0^{\infty} \frac{\sin(xw)}{w} \exp\left(-\frac{w^2\sigma^2}{2}\right) I_0(A_jw) dw \quad (6.49)$$

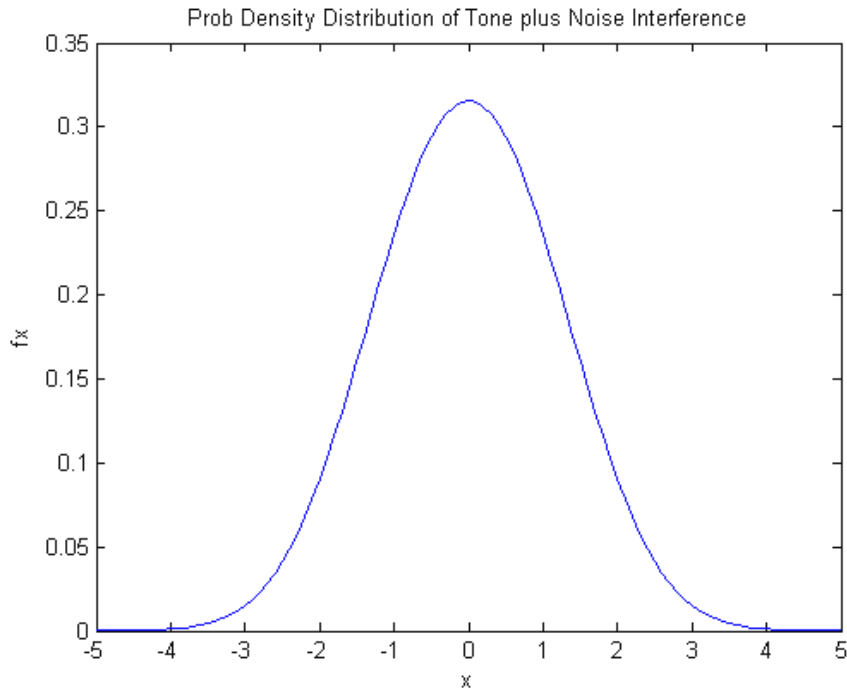


Figure 6.9 Probability Density Distribution of Tone plus Noise Interference

If there is only one jamming tone inside the receiving bandwidth, the symbol error probability turns out to be

$$P_e = 1 - F_X(x) \quad (6.50)$$

After some manipulation, the symbol error probability of BPSK, when a single tone and Gaussian noise are present, is derived as

$$P_e = \frac{1}{2} - \frac{1}{\pi} \int_0^{\infty} \frac{\sin(A_s w)}{w} \exp\left(-\frac{w^2 \sigma^2}{2}\right) I_0(A_j w) dw \quad (6.51)$$

By the same logic, if there are M jamming tones inside the receiving bandwidth and the phases of the jamming tones are independent, the symbol error probability turns out to be

$$P_e = \frac{1}{2} - \frac{1}{\pi} \int_0^{\infty} \frac{\sin(A_s w)}{w} \exp\left(-\frac{w^2 \sigma^2}{2}\right) \times \prod_{i=1}^M I_0(A_{ji} w) dw \quad (6.52)$$

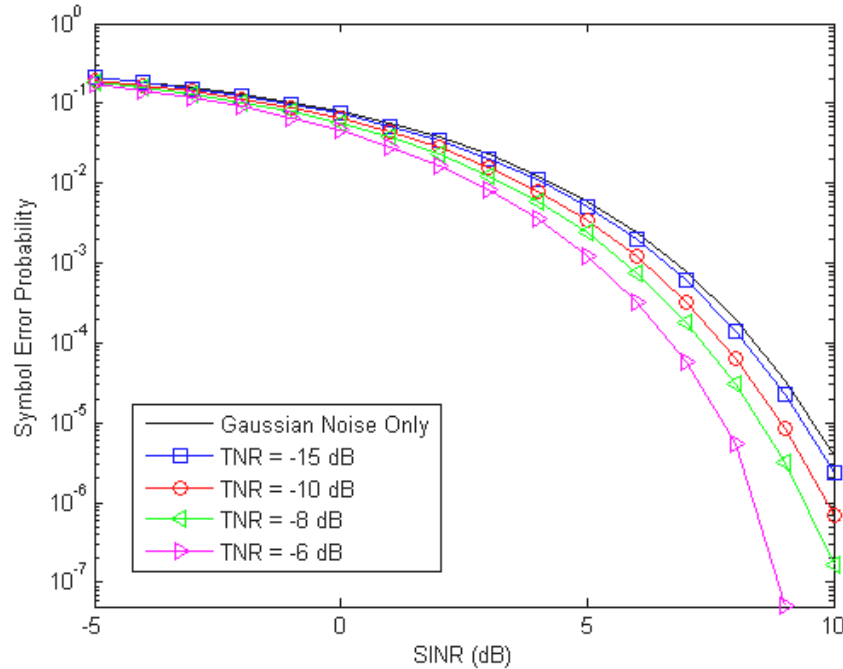


Figure 6.10 SER vs. SINR under Different TNRs

In the case that there is only one jamming tone inside the receiver bandwidth and BPSK modulation is used in the receiver, the relationships of symbol error rate (SER) and the signal to interference and noise ratio (SINR) under different interference tone to noise ratio (TNR) are calculated with the above procedure and the results are shown in Figure 6.10. The signal to interference and noise ratio (SINR) is defined as the ratio of signal power to the sum of multiple tone power and additive white Gaussian noise power. The interference tone to noise ratio (TNR) is defined as the ratio of the aggregate power of in band jamming tones to the total power of both additive white Gaussian noise from UWB signals and the thermal noise inside the narrowband receiver. For the same SINR, the SER decreases as the TNR increases. This is because that the probability distribution $f_Y(y)$ of the tone interference does not have the long tails as the Gaussian distribution has.

The previous UWB interference model, which has white Gaussian noise only, can be considered as a special case of our new model which has both Gaussian noise and jamming tones. From Figure 6.10, we can see that when tone-to-noise ratio is high, the Gaussian noise only model over estimates the SER. For pulsed UWB devices, the signal power spectrum can be designed to look as close as possible to white Gaussian noise through modulation adjustment. The interference effect of pulsed UWB devices will be close to white Gaussian noise. However, the analysis of the UWB-OFDM interference to narrow band receiver is rather difficult. A simplified model will be normalizing the OFDM power into equivalent Gaussian noise power. In this case, OFDM interference is modeled as Gaussian noise only. [CoEm05] proposed a new OFDM interference model, which combines both Gaussian noise and impulsive noise together to model OFDM interference. Through this model, it has been found out that the interference effects of UWB-OFDM to narrowband receivers are relatively more damaging than that of Gaussian noise especially when the data rate of the victim receiver is high and the number of hopping frequency band in UWB-OFDM devices is big.

6.5 Conclusions

Based on FCC regulations on UWB emission and a generic link analysis of C-band receivers, a calculation method of separation distance between UWB devices and C-band satellite receivers is presented. This method can be easily adapted to any practical situations. The power spectrum of impulse UWB signal is investigated both analytically and numerically. Generally speaking, UWB power spectrum will have both continuous part and discrete lines. The strength of these discrete lines can be reduced to a certain level by adjusting UWB pulse modulation scheme. A new analytical method of assessing the narrowband performance degradation due to UWB interferences is proposed and demonstrated with numerical results. This method models the UWB interference as a composite signal of random like noise and jamming tones. Through

this method, it has been found out that for the same SINR, the symbol error rate decreases as the power portion of jamming tones increases. This is because that the probability distribution of jamming tones doesn't have the long tails as the Gaussian noise has.

7 Summary

7.1 Contributions

This dissertation consists of seven chapters in total, and each of the previous six chapters addresses on one aspect of the UWB communication systems. The originalities and contributions of each chapter are summarized as follows.

Chapter 1 serves as an introduction to the UWB (Ultra Wide Band) technology. It first introduces the definition of UWB, then demonstrates that due to the high speed communication market pull and the latest digital technology drive, UWB is a very promising technology for the future high-speed wireless communication. The research on UWB is crucial to bringing this technique to practice. Even though tremendous fundamental framework has been accomplished, many practical issues in the UWB

system are still unsolved. The goal of this dissertation is to study some unsolved issues in UWB applications while inheriting the established theory and paradigm, and therefore to contribute to the field knowledge of UWB.

The originality of this chapter is that it proposes a three-wave historical structure of UWB research. The seminal paper of T. W. Barret, “History of ultra wideband (UWB) radar & communications: pioneers and innovators”, is a milestone of historical review of UWB literature. Paper [Barr00] lists many important achievements in the UWB development year by year. However, it lacks a structure to hold all the historical facts together. This chapter partitions the history into three waves. The first wave is from the 19th century to the World War II. Some fundamental research had been done in this period. The second wave is from 60s to 80s. In this wave, UWB research concentrated more on military or other special applications. The third wave is from 90s to now. In this wave, the UWB research is more energetic and more commercial oriented. Tremendous UWB research has been devoted to high-speed wireless communications. This chapter not only reviews the UWB research historically or horizontally, but also vertically compares the UWB as a communication technique with contemporary wireless communication standards such as Blue Tooth, IEEE 802.11a, b, and g. The outstanding characteristics of UWB technology such as high data rate, high spatial capacity, etc., are demonstrated and emphasized.

Chapter 2 talks about UWB pulses and modulation types. Impulse radio is based upon transmitting and receiving very short pulses. Three types of UWB pulses have often appeared in the recent UWB research literature, i.e., Gaussian pulse, monocycle pulse, and doublet pulse. These pulses are usually employed to conduct basic theoretical analysis and simulation study. The information bits are embedded in the pulses by modulation. Some UWB modulation types, such as time hopping pulse position modulation, time hopping phase and amplitude modulation, direct sequence spread spectrum, and orthogonal frequency division modulation, are studied in this chapter. Bit-error-rate (BER) is a means to evaluate the performance of UWB communication

systems. Generally speaking, the BER analysis methods can be categorized into two classes. One is based upon the Gaussian assumption, and it is named GA method. The other one doesn't have to assume Gaussian distribution, and it derives the BER through characteristic function (CF). So it is called CF method. Since CF method doesn't need to make Gaussian assumption, it is more accurate than GA method is. However, Gaussian assumption makes the BER analysis simpler to calculate and easier to understand. Whenever it is reasonable to make Gaussian assumption in the real world applications, most engineers prefer GA method.

The originality in this chapter is that it simplifies the BER derivation of the characteristic function method. B. Hu and N. C. Beaulieu first introduced the characteristic function method of PPM BER analysis. But in their paper [HuBe04], conditional probabilities are used to derive the bit error rate. The derivation is complicated and not so easy to understand. This chapter simplifies the derivation by using unconditional probabilities. The analysis is easier to understand and the results are the same as what Hu and Beaulieu got.

Chapter 3 proposed a semi-analytical RAKE receiver performance assessment method on the basis of realistic UWB channel modeling, instantaneous SNR of RAKE receiver, and instantaneous bit error rate of MBOK UWB signals.

In this chapter, contemporary UWB channel modeling methods are briefly reviewed and the IEEE 802.15.3a standard UWB channel model is studied in detail. Through both analytical and simulation studies, it has been found out that the UWB channel coherence bandwidth is generally less than 30 MHz. Comparing to hundreds of mega hertz of the data rate that UWB devices try to accomplish, the UWB channel coherence bandwidth is severely less than the UWB symbol rate. This will result in ISI in pulsed UWB communication systems.

A new simulation method for performance assessment of RAKE receivers in UWB communication systems is proposed, which is based on [RaSo03]. The proposed model is more accurate than the model in [RaSo03] due to the following two reasons: (1) the old model uses average SNR to assess the RAKE receiver performance, while the proposed model uses both instantaneous SNR and the UWB channel properties to assess the RAKE performance. (2) the proposed model includes MAI while the old model doesn't.

With the proposed RAKE receiver simulation model, the performance of MBOK UWB signals are simulated for both MRC and EGC RAKE receivers under various conditions. For MBOK UWB communication systems, MRC RAKE receivers outperform the EGC RAKE receivers in all conditions.

Chapter 4 formulated an optimized transmitting and receiving filter design problem with a transmission power spectral mask constraint. A 2-stage solution to this optimization problem is proposed and demonstrated with an example, in which the transmission power is constrained within the FCC indoor transmission spectral mask. In the first stage of the optimization, a closed form of optimal transmission FIR filter coefficients is derived. In the second stage optimization, BFGS numerical method is shown to be an efficient tool to optimize the receiving filter. The three major advantages of the proposed joint optimization method are: (1) it has superior MAI suppression capability; (2) it can achieve the best system performance by optimizing transmitting and receiving filters jointly; (3) it can minimize the UWB interference to other narrow band systems to a tolerable level.

The interference suppression capability of the joint optimization method is shown to be superior to that of conventional one-stage optimization method in a comparative SNR simulation study. With the Intel channel model, the BER performance of both joint optimization method and one-stage optimization method are scrutinized under both LOS and NLOS channel environments. As noted previously, both theoretic analysis and

simulation study demonstrate that the proposed joint optimization method outperforms the one-stage optimization method in terms of SNR and BER performance within TH-PPM UWB communication systems.

In Chapter 5, a pulse shape optimizer design procedure is proposed to maximize the SNR of the received signal for time-limited sinusoidal template UWB receivers. The pulse shape optimizer is basically an all-pass filter, whose coefficients are designed to maximize the SNR with genetic algorithms.

In coherent UWB receivers, creating a template to exactly match the received signal is usually difficult and costly. If a simplified template is employed, the receiver's performance will degrade due to the unmatched template. The pulse shaping optimizer is used to mitigate the performance degradation while using unmatched simple receiving templates. The proposed pulse shaping optimizer has an all-pass filter structure, which ensures that the power density spectrum of the received signal won't be changed by the optimizer. Since the objective function of the SNR optimization has multiple maxima, traditional searching methods, which are based on gradient or higher derivatives can't guarantee to find a global optimal solution. Genetic algorithm is able to find the global optimal solution when evolution time is high enough and is employed in this all-pass filter optimization. By adjusting the coefficients of the pulse shaping optimizer, the receiver's SNR is optimized and the system performance is therefore enhanced. Through simulation study, it turns out that a second-order pulse shape optimizer is the most efficient choice in terms of SNR maximization. Higher order pulse shape optimizers won't improve the SNR significantly. The UWB receiver with fixed receiving template and fixed pulse shaping optimizer is quite sensitive to time offset, but is relatively insensitive to frequency offset.

Chapter 6 studied UWB Interferences to C-band Satellite Receivers. Based on FCC regulations on UWB emission and a generic C-band receiver link budget analysis, a

calculation method of separation distance between UWB devices and C-band satellite receivers is proposed in this chapter. This method can be easily adapted to any other practical situations. It is demonstrated both analytically and numerically that UWB power spectrum has both continuous and discrete components. The strength of the undesirable discrete lines can be reduced to a certain level by adjusting UWB pulse modulation scheme. A novel analytical method of assessing the narrowband performance degradation due to UWB interferences is proposed and demonstrated with numerical results. This method models the UWB interferences as composite noise of random like noise and jamming tones. The symbol error rate of narrowband receivers under interference of UWB devices is derived using the characteristic function of the composite interference and noise. Through simulation, it has been found out that for the same SINR, the symbol error rate decreases as the power portion of jamming tones increases. This is because that the probability distribution of jamming tones doesn't have the long tails as the Gaussian noise has.

Overall, this dissertation has investigated several important aspects of interference control, performance analysis, and performance improvement in UWB communications. Several new methods are proposed and many fruitful findings are presented.

7.2 Future Research Directions

Since UWB technology has a promising future for high-speed short-range applications, such as wireless LAN, home entertainment, wireless video downloading, etc., there still exist a significant amount of research opportunities in the future. Conventional research issues inside the physical layer, such as UWB ISI reduction, data acquisition, clock synchronization, Doppler effects on UWB systems, RAKE receiver performance under UWB channel environments, multiple access, low probability interception (LPI), etc.,

are still attracting research attention. As the data rate gets higher and higher, new research issues across physical layer, link layer, and even upper layers, such as physical layer and link layer optimization to increase overall system throughput, pico-net self-organization, and cooperation with existing wireless devices, etc., are also burgeoning research areas. Other technologies such as wide band antennas, digitally tunable RF front end, software defined radio, ADC with higher sampling rate and more bits per sample, high-speed digital signal processor, etc., are also critical to the deployment of UWB communication systems. The future of UWB technology is bright and the research in this area will remain active in at least the near future.

8 References

- [Abi03] Allied Business Intelligence, "Ultra wideband can find relief from CE industry," [Online]. Available at: <http://www.abiresearch.com/pdfs/UWB02pr3.pdf>
- [AhLe93] J. Ahn and H. S. Lee, "Frequency domain equalization of OFDM signal over frequency non-selective Rayleigh fading channels," *IEE Electronics Letters*, vol. 29, No. 16, 1993, pp 1476-1477.
- [AiRo03] G. R. Aiello and G. D. Rogerson, "Ultra-wideband wireless systems," *IEEE Microwave Magazine*, June 2003, pp.36 – 47.
- [Amba99] Ashok Ambardar, *Analog and Digital Signal Processing*. Brook Cole, 2nd edition, 1999.
- [AnTe00] A. Annamalai, C. Tellambura, and V. K. Bhargava, "Equal-gain diversity receiver performance in wireless channels," *IEEE Trans. Comm.* vol. 48, Oct. 2000, pp. 1732-1745.
- [Anto93] A. Antonio, *Digital Filters: Analysis, Design, and Application*. McGraw-Hill, 2nd Edition, 1993.
- [ArDy62] E. Arthurs and H. Dym, "On the optimum detection of digital signals, in the presence of white Gaussian noise – a geometric interpretation and a study of three basic data transmission systems", *IRE Trans. on Commu. Systems*, Vol. CS-10, pp. 336-372, Dec. 1962.
- [BaCa00] P. Banelli and S. Cacopardi, "Theoretical analysis and performance of OFDM signals in nonlinear AWGN channels," *IEEE Trans. Commu.* vol. 48, No. 3, March 2000, pp. 430 - 441.
- [Bahe90] H. Baher, *Analog and Digital Signal Processing*. John Wiley & Sons, 1st edition, 1990.
- [Barr00] T. W. Barret, "History of ultra wideband (UWB) radar & communications: pioneers and innovators," *Progress in Electromagnetics Symposium 2000 (PIERS2000)*, Cambridge, MA, July 5-14, 2000.

- [BeGi04] M. D. Benedetto and G. Giancola, *Understanding Ultra Wide Band Radio Fundamentals*. Upper Saddle River, New Jersey: Prentice Hall PTR, 2004.
- [Bren59] D. G. Brennan, "Linear diversity Combining Technique," *Proc. IRE.*, vol. 47, pp. 1075-1102, 1959.
- [BuLe64] J. J. Bussgang and M. Leiter, "Error rate approximations for differential phase-shift keying", *IEEE Trans. on Comm. Systems*, vol. CS-12, March 1964, pp. 18-27.
- [CaLe91] E. Casas and C. Leung, "OFDM for data communication over mobile radio FM channels – part I: analysis and experimental results," *IEEE Trans. Commu.*, vol. 39, No. 5, May 1991, pp. 783 – 793.
- [CaLe92] E. Casas and C. Leung, "OFDM for data communication over mobile radio FM channels – part II: performance improvement," *IEEE Trans. Commu.*, vol. 40, No. 4, April 1992, pp. 680 – 683.
- [ChDo99] M. Cherniakov and L. Donskoi, "Frequency band selection of radars for buried object detection," *IEEE Transactions on Geo-science and Remote Sensing*, vol. 37, issue 2, March 1999, pp. 838-845.
- [ChOh03] S. Choi and W. Oh, "Analysis the interference of pulse position modulated UWB into IEEE 802.11 a WLAN," *IEEE Joint UWBST & IWUWBS 2004*, May 18-21, 2004, pp. 328 – 331.
- [ChSc04] Y. Chao and R. A. Scholtz, "Novel UWB transmitted reference schemes," *The 38th Asilomar Conference on Signals, Systems and Computers*, 2004, pp. 652 – 656.
- [ChSt02] J. D. Choi and W. E. Stark, "Performance analysis of ultra-wideband spread-spectrum communications in narrowband interference," *IEEE proceedings of 02 MILCOM*, 2002, pp.1075-1080.
- [ChSu02] M. Chang and Y. Su, "Performance analysis of equalized OFDM systems in Rayleigh fading," *IEEE Trans. Wireless Commu.*, vol. 1, No.4, October 2002, pp. 721 – 732.
- [ChWi03] M. Chiani, M. Z. Win, A. Zanella, R. K. Mallik, and J. H. Winters, "Bounds and approximations for optimum combining of signals in the presence of multiple cochannel interferers and thermal noise," *IEEE Transactions on Communications*, vol. 51, No. 2, Feb. 2003, pp. 296-307.

- [CoEm05] C. A. Corral, S. Emami, and G. Rasor, "Model of Multi-Band OFDM Interference on Broadband QPSK Receivers" *IEEE International Conference on Acoustics, Speech, and Signal Processing (ICASSP '05)*, vol. 3, March 18-23, 2005, pp. 629 – 632.
- [CrSc02] J. M. Cramer, R. A. Scholtz, and M. Z. Win, "Evaluation of an ultra-wideband propagation channel," *IEEE Transactions on Antennas and Propagation*, vol. 50, No. 5, May 2002, pp. 561-570.
- [DiAn86] P. S. Diniz and A. Antoniou, "More economical state space digital-filter structures which are free of constant-input limit cycles," *IEEE Trans. Acoust., Speech, Signal Process.*, vol. ASSP-34, August 1986, pp. 807-815.
- [ElMa04] J. Ely, W. Martin, G. Fuller, T. Shaver, J. Zimmerman, and W. Larsen, "UWB EMI to aircraft radios: field evaluation on operational commercial transport airplanes," *IEEE Digital Avionics Systems Conference, DASC 04*, vol. 2, Oct. 24-28, 2004, pp. 9.D.4-1 - 9.D.4-11.
- [EeWa96] P. V. Eetvelt, G. Wade, and M. Tomlinson, "Peak to average power reduction for OFDM schemes by selective scrambling," *IEE Electronics Letters*, August 1996, pp. 1963-1964.
- [Farh98] B. Farhang-Boroujeny, *Adaptive Filters Theory and Application*. New York, NY: John Wiley & Sons, 1998.
- [FCC02] "Notice of Inquiry in the Matter of Revision of Part 15 of the Commission's Rules Regarding Ultra-Wideband Transmission Systems", FCC Docket Number (No.) 98-208/ET No. 98-153.
- [FiKo04] R. Fisher, R. Kohno, M. McLaughlin, and M. Welborn, "DS-UWB Physical Layer Submission to 802.15 Task Group 3a," IEEE P802.15-04/0137r3, July, 2004.
- [FiPr03] B. Firoozbakhsh, T. Pratt, and N. Jayant, "Analysis of IEEE 802.11a interference on UWB systems," *IEEE Conference on Ultra Wideband Systems and Technologies*, Nov. 16-19, 2003, pp. 473 – 477.
- [Flet80] R. Fletcher, *Practical methods of optimization, vol. 1, Unconstrained optimization, and vol. 2, Constrained optimization*. John Wiley and Sons, 1980.

- [Foer02a] J. Foerster, "Interference modeling of pulse-based UWB waveforms on narrowband systems," *IEEE 55th Vehicular Technology Conference, VTC Spring 2002*, vol. 4, May 6-9, 2002, pp. 1931 – 1935.
- [Foer02b] J. Foerster, "The performance of a direct-sequence spread ultra-wideband system in the presence of multipath, narrowband interference, and multiuser interference," *IEEE Proceedings of 2002 UWBST*, 2002, pp.87-92.
- [FoGr01] J. Foerster, E. Green, and S. Somayazulu, "Ultra-wideband technology for short or medium range wireless communications," *Intel Technology Journal*, Q2 2001.
- [FoLi01] J. Foerster, Q. Li, "UWB Channel Modeling Contribution from Intel," IEEE document # 02279r0P802_15_SG3a.
- [FoLi02] J. Foerster, Q. Li, "Channel modeling subcommittee report final," IEEE P802.15 WG for WPANs Technical Report, No. 02/490r0-SG3a, 2002.
- [Frie96] M. Friese, "Multicarrier modulation with low peak-to-average power ratio," *Electronics Letters*, vol. 32, No. 8, April 1996, pp. 713-714.
- [FeRa93] M. Feuerstein and T. Rappaport, *Wireless Personal Communications*. Boston, MA: Kluwer Academic Publisher, 1993.
- [GhGr] S. S. Ghassemzadeh, L. J. Greenstein, and V. Tarokhm, "The Ultra-Wideband Indoor Multi-path Model," IEEE Document#02282r0P802-15-SG3a.
- [GhMi04] M. Ghavami, L. B. Michael, and R. Kohno, *Ultra Wideband Signals and Systems in Communication Engineering*. John Wiley & Sons, Ltd., 2004.
- [GhTa03] S. S. Ghassemadeh, and V. Tarokh, "UWB path loss characterization in residential environments," *IEEE Radio Frequency Integrated Circuits Symposium*, June, 2003, pp. 501-504.
- [GiMu81] Gill, P. E., W. Murray, and M. H. Wright, *Practical Optimization*. London: Academic Press, 1981.
- [GiWi04] W. M. Gifford and M. Z. Win, "On the transmitted-reference UWB communications," *The 38th Asilomar Conference on Signals, Systems and Computers*, 2004, pp. 1526 – 1531.

- [Gong88] K. S. Gong, "Performance analysis of FH/DPSK in additive white Gaussian noise (AWGN) and multi-tone jamming," *Conference Record of MILCOM88*, vol. 3, Oct. 23-26, 1988, pp. 947-953.
- [HaHo01] M. Hamalainen, V. Hovinen, J. Iinatti, and M. Latva-aho, "In-band interference power caused by different kinds of UWB signals at UMTS/WCDMA frequency bands," *IEEE RAWCON 2001*, Aug. 19-22, 2001, pp. 97 – 100.
- [Hali01] M. Hamalainen, J. Iinatti, V. Hovinen, and M. Latva-aho, "In-band interference of three kinds of UWB signals in GPS L1 band and GSM900 uplink band," *IEEE International Symposium on Personal, Indoor and Mobile Radio Communications*, Sept. 30 -Oct.3, 2001, vol. 1, pp. D-76 - D-80.
- [Harm72] H. F. Harmuth, *Transmission of Information by Orthogonal Functions*. Second Edition, New York: Springer, 1972.
- [Harm75] H. F. Harmuth, "Range-doppler resolution of electromagnetic walsh waves in radar," *IEEE Trans. Electromagn. Compat.*, EMC-17, 1975, pp. 106-111.
- [Harm78] H. F. Harmuth, "Frequency-sharing and spread-spectrum transmission with large relative bandwidth," *IEEE Trans. Electromagnet. Compatibility*, EMC-20, 1978, pp. 232-239.
- [Harm81] H.F. Harmuth, *Nonsinusoidal Waves for Radar and Radio Communication*. New York: Academic, 1981.
- [Hash93] H. Hashemi, "Impulse response modeling of indoor radio propagation channels," *IEEE JSAC*, Vol. 11, No. 7, Sept. 1993, pp. 967-978.
- [HaTe02] M. Hamalainen, R. Tesi, and J. Iinatti, "On the UWB system performance studies in AWGN channel with interference in UMTS," *IEEE proceedings of 2002 UWBST, 2002*, pp. 321-326.
- [HoTo02] R. T. Hoctor and H. W. Tomlinson, *An Overview of Delay-Hopped, Transmitted-Reference RF Communications*, General Electric Company, 2001CRD198, January 2002, [Online]. Available at: <http://www.crd.ge.com/cooltechnologies/pdf/2001crd198.pdf>.
- [HuBe03] B. Hu and N. C. Beaulieu, "Precise bit error rate of TH-PPM UWB systems in the presence of multiple access interference," *IEEE*

Conference on Ultra Wideband Systems and Technologies, 16-19 Nov. 2003, pp. 106 – 110.

- [HuBe04] B. Hu and N. C. Beaulieu, "Accurate evaluation of multiple-access performance in TH-PPM and TH-BPSK UWB systems," *IEEE Trans. Commun.*, vol. 52, Oct. 2004, pp. 1758-1766.
- [Hwan01] C. Hwang, "A peak power reduction method for multicarrier transmission," *IEEE International Conference on Communications*, vol. 5, June 2001, pp. 1496-1500.
- [IaBe02] M. Iacobucci, M. De Benedetto, and L. Di Nardis, "Radio frequency interference issues in impulse radio multiple access communications," *IEEE proceedings of 2002, UWBST*, 2002, pp.293-296.
- [JaBo96] M. Jaureguy, P. Borederies, "Modelling and processing of ultra-wideband scattering of buried targets," *IEE Conference Publication*, No. 431, October 1996, pp. 119-123.
- [JoWi94] A. E. Jones, T. A. Wilkison, S. K. Barton, "Block coding scheme for reduction of peak to mean envelope power ratio of multicarrier transmission schemes," *IEE Electronics Letters*, vol. 30, No. 25, Dec., 1994, pp 2098-2099.
- [Koza94] J. R. Koza, *Genetic Programming*. Cambridge: MIT Press, 1994.
- [KrCo02] L. Krishnamurthy, S. Conner, M. Yarvis, J. Chhabra, C. Ellison, C. Brabenac, and E. Tsui, "Meeting the demands of the digital home with high-speed multi-hop wireless networks," *Intel Technology Journal*, vol.6, issue 4, November, 15, 2002.
- [KuMi03] A. Kurosu, S. Miyase, S. Tomiyama, and T. Takebe, "A technique to truncate IIR filter impulse response and its application to real-time implementation of linear-phase IIR filter," *IEEE Transactions on Signal Processing*, vol. 51, No. 5, 2003, p1284-1292.
- [LaFi04] D. Landi and C. Fischer, "The effects of UWB interference on GSM systems," *2004 International Zurich Seminar on Communications*, 2004, pp. 86 – 89.
- [LaMc94] M. Lawton and J. McGeenhan, "The application of a deterministic ray launching algorithm for the prediction of radio channel characteristics in small-cell environments," *IEEE Transactions on Vehicular Technology*, vol. 43, issue 4, November 1994, pp. 955-969.

- [Lee02] S. Lee, "Design and Analysis of Ultra-wide Bandwidth Impulse Radio Receiver," Ph.D. thesis, electrical engineering department, University of Southern California, 2002.
- [Leep01] D. Leeper, "A long-term view of short-range wireless," *Computer*, Vol. 34, No. 6, 2001, pp. 39-44.
- [LeHa00] H. Lee, B. Han, Y. Shin, and S. Im, "Multipath characteristics of impulse radio channels," *IEEE Vehicular Technology Conference Proceedings*, vol. 3, May 2000, pp.2487-2491.
- [LeNg01] J.S. Lee and C. Nguyen, "Novel low-cost ultra wideband, ultra-short-pulse transmitter with MESFET impulse-shaping circuitry for reduced distortion and improved pulse repetition rate," *IEEE Microwave and Wireless Components Letters*, vol. 11, No 5, May 2001, pp.208-210.
- [LiCi98] X. Li and L. J. Cimini, "Effects of clipping and filtering on the performance of OFDM," *IEEE Communication Letters*, vol. 2, No.5, May 1998, pp. 131-133.
- [LiRi97] X. Li and J. A. Ritcey, "M-sequences for OFDM PAPR reduction and error correction," *IEE Electronics Letters*, vol. 33, 1997, pp. 545-546.
- [Liu99] B. Liu, *Uncertain Programming*. New York: John Wiley & Sons, 1999.
- [LuYa03] X. Luo, L. Yang, and G. B. Giannakis, "Designing optimal pulse-shapers for ultra-wideband radios," *IEEE conference on Ultra Wideband Systems and Technologies*, Reston, Virginia, November 2003, pp. 349 - 353.
- [MaLe03] K. Marsden, H. Ha, and H. Lee, "Low power CMOS re-programmable pulse generator for UWB systems," *IEEE conference on Ultra Wideband Systems and Technologies*, Reston, Virginia, November 2003, pp. 443-447.
- [MaRo98] T. May and H. Rohling, "Reducing the peak to average power ratio in OFDM radio transmission systems," *IEEE conference proceedings VTC*, 1998, pp. 2474-2478.
- [MaWi02] R. K. Mallik, M. Z. Win, "Analysis of hybrid selection/maximal-ratio combining in correlated Nakagami fading," *IEEE Transactions on Communications*, vol. 50, No. 8, Aug. 2002, pp. 1372-1383.

- [McBu03] D. R. McKinstry and R. M. Buehrer, "LMS analog and digital narrowband rejection system for UWB communications," *IEEE Conference on Ultra Wideband Systems and Technologies*, Nov. 16-19, 2003, pp.91 – 95.
- [Meer76] K. Meerkotter, "Realization of limit cycle-free second order digital filters," *Proc. 1976 IEEE Int. Symp. Circuits Syst.*, pp295-298.
- [Mill02] L. E. Miller, "Models for UWB pulses and their effects on narrowband direct conversion receivers," *IEEE Conf. UWBST03*, 2003, pp. 101-105.
- [Mitic96] M. Mitchell, *An Introduction to Genetic Algorithms*. Cambridge: MIT Press, 1996.
- [MoFr05] Y. T. Morton, M. P. French, Q. Zhou, J. B. Y. Tsui, D. M. Lin, M. M. Miller, D. Janning, "Software approach to access UWB interference on GPS receivers," *IEEE Aerospace and Electronic Systems Magazine*, vol. 20, Issue 1, 2005, pp. 28 – 33.
- [MuOF04] *Multi-band OFDM Physical Layer Proposal for IEEE 802.15 Task Group 3a*, IEEE WG for WPANs Technical Report, No. P802.15-03/268r3.
- [MuHu97] S. H. Muller, and J. B. Huber, "A comparison of peak power reduction schemes for OFDM," *Proc. IEEE GLOBECOM '97*, New York, NY USA, pp. 1-5, 1997.
- [ONLo95] R. O'Neill and L. B. Lopes, "Envelope variations and spectral splatter in clipped multicarrier signals," *IEEE conference proceedings PMIRC*, 1995, pp. 71-76.
- [PaCh03] B. Parr, B. Cho, K. Wallace, and Z. Ding, "A novel ultra-wideband pulse design algorithm," *IEEE Comm. Letters*, 2003, pp.219-221.
- [PaKo03] J. E. Padgett, J. C. Koshy, and A. A. Triolo, "Physical-layer modeling of UWB interference effects," *Wireless System and Networks Research*, Telcordia Technologies, Inc., January 10, 2003.
- [PaKu98] M. Pauli and H. P. Kuchenbecker, "On the reduction of the out of band radiation of OFDM signals," *IEEE conference proceedings ICC*, 1998, vol. 3, pp. 1304-1308.
- [Papo65] A. Papoulis, *Probability, Random Variables, and Stochastic Processes*. McGraw-Hill Book Company, 1965.

- [PaRi82] R. F. Pawula, S. O. Rice, and J. H. Roberts, "Distribution of the Phase Angle Between Two Vectors Perturbed by Gaussian Noise", *IEEE Trans. on Comm.*, Vol. COM-30, August 1982, pp. 1828-1841.
- [Pawu01] R. F. Pawula, "Distribution of the phase angle between two vectors perturbed by Gaussian noise II," *IEEE Transactions on Vehicular Technology*, vol. 50, March 2001, pp. 576-583.
- [PeBe] M. Pendergrass and W. C. Beeler, "Empirically based statistical ultra-wideband channel model," IEEE Document#02240r0P802-15-SG3a.
- [PoCh91] S. R. Powell, and P. M. Chau, "A technique for realizing linear phase IIR filters," *IEEE Transactions on Signal Processing*, vol. 39, No. 11, 1991, p2425-2435.
- [PrGr58] R. Price and P. E. Green, "A Communication Technique for Multipath Channels," *Proc. IRE*, vol. 46, March 1958, pp. 555-570.
- [Proa01] John G. Proakis, *Digital Communications*. 4th Edition, McGraw-Hill, 2001.
- [PrTe95] W. H. Press, S. A. Teukolsky, W. T. Vetterling, and B. P. Flannery, *Numerical Recipes in C*. 2nd edition, Cambridge University Press, 1995.
- [Rapp02] T. Rappaport, *Wireless Communications: principles and practice*. 2nd Ed., Pearson Education Pte. Ltd., 2002.
- [RaGo75] L. Rabiner and B. Gold, *Theory and Application of Digital Signal Processing*. Prentice-Hall, 1975.
- [RaSo03] A. Rajeswaran, V. S. Somayazulu, and J. R. Foerster, "Rake performance for a pulse based UWB system in a realistic UWB indoor channel," *IEEE International Conference on Communications (ICC'03)*, Vol. 4, 11 – 15 May 2003, pp. 2879-2883.
- [RoRo73] G. F. Ross and K. W. Robbins, *Base-band radiation and reception system*. U.S. Patent 3,739,392 dated June 12, 1973.
- [RoRo87] G. F. Ross and K. W. Robbins, *Narrow range-gate baseband receiver*. U.S. Patent 4,695,752, dated Sep 22, 1987.
- [Ross73] G. F. Ross, *Transmission and reception system for generating and receiving base-band duration pulse signals for short base-band pulse communication system*. U.S. Patent 3,728,632 dated Apr 17, 1973.

- [Rowe65] H. E. Rowe, *Signal and Noise in Communications Systems*, Princeton, New Jersey: D. Van Nostrand Company, Inc., 1965.
- [SaHa03] A. Saito, H. Harada, and A. Nishikata, "Development of Band Pass Filter for Ultra Wideband (UWB) Communication Systems," *IEEE UWBST03 conference*, Reston, Virginia, 2003, pp. 76 - 80.
- [SaVa87] A. Saleh and R. Valenzuela, "A statistical model for indoor multipath propagation," *IEEE JSAC*, Vol. SAC-5, No. 2, Feb. 1987, pp. 128-137.
- [Scho93] R. A. Scholtz, "Multiple access with time-hopping impulse modulation," *Proc. of MILCOM Conf.*, Boston, MA, USA, October 11-14, 1993, pp. 447-450.
- [Sele00] I. Selesnick, "Linear-phase FIR filter design by least squares," <http://cnx.rice.edu/content/m10577/2.5/>
- [SeRa94] S. Seidel and T. Rappaport, "Site-specific propagation prediction for wireless in-building personal communication system design," *IEEE Transactions on Vehicular Technology*, vol. 43, issue 4, November 1994, pp. 879-891.
- [ShGa67] C. E. Shannon, R. G. Gallager, and E. R. Berlekamp, "Lower bounds to error probability for coding on discrete memoryless channels," *Infor. And Control*, vol. 10, 1967, pp.65-103 (Part I), pp. 522-552 (Part II).
- [SiBe03] K. Siwiak, H. Bertoni, and S. Yano, "On the relation between multipath and wave propagation attenuation," *Electronic Letters*, 39(1), 2003, pp. 142-143.
- [SiMc04] K. Siwiak and D. Mckeown, *Ultra-wideband Radio Technology*. West Sussex, England: John Wiley & Sons, Ltd., 2004.
- [SiPe01] K. Siwiak and A. Petroff, "A path link model for ultrawide band pulse transmission," *IEEE Vehicular Technology Conference*, vol. 2, May 2001, pp. 1173-1175.
- [Stro03] Steve Stroh, "Ultra-wideband: multimedia unplugged," *IEEE Spectrum*, September 2003, pp. 23 – 27.
- [Suzu77] H. Suzuki, "A statistical model for urban radio propagation," *IEEE Transactions on Communications*, July 1977, pp.673-680.

- [Tayl83] F. J. Taylor, *Digital Filter Design Handbook*. Marcel Dekker, Inc., 1983.
- [Thom68] J. B. Thomas, *An introduction to statistical communication theory*. New York: John Wiley & Sons, Inc., 1968.
- [ToOg03] A. Tomiki, T. Ogawa, and T. Kobayashi, "Experimental evaluation of interference from UWB sources to a 5-GHz narrowband digital wireless transmission system," *IEEE Conference on Ultra Wideband Systems and Technologies*, Nov. 16-19, 2003, pp. 498 – 502.
- [Tran03] W. H. Tranter, "Computer Aided Design and Analysis of Communication Systems with Wireless Applications," course note, 2003.
- [Turn83] L. E. Turner, "Elimination of Constant-Input Limit Cycles in Recursive Digital Filters Using a Generalised Minimum Norm," *IEE Proc.*, vol. 130, June 1983, pp. 69-77.
- [UhMa04] C. Uhl, C. Martret, J. Pla, "Jamming assessment of impulse UWB signals on Galileo receivers," *IEEE Joint UWBST & IWUWBS 2004*, May 18-21, 2004, pp. 55 - 59.
- [Verk77] G. Verkroost, "A General Second-Order Digital Filter with Controlled Rounding to Exclude Limit Cycles for Constant Input Signals," *IEEE Trans. Circuits Syst.*, vol. CAS-24, August 1977, pp. 428-431.
- [WaWa03] T. Wang, Y. Wang, and K. Chen, "Analyzing the interference power of narrowband jamming signal on UWB system," *14th IEEE Proceedings on Personal, Indoor and Mobile Radio Communications, PIMRC 2003*, vol.1, Sept. 7-10, 2003, pp. 612 – 615.
- [Weis02] C. J. Weisman, *The Essential Guide to RF and Wireless*. Upper Saddle River, NJ: Prentice Hall PTR, 2002.
- [WeSh49] W. Weaver and C. E. Shannon, *The Mathematical Theory of Communication*. Urbana, Illinois: University of Illinois Press, 1949.
- [WiBe03] M. Z. Win, N. C. Beaulieu, L. A. Shepp, B. F. Logan, J.H. Winters, "On the SNR penalty of MPSK with hybrid selection/maximal ratio combining over i.i.d. Rayleigh fading channels," *IEEE Trans. Commu.*, vol. 51, No. 6, June 2003, pp. 1012-1023.

- [WiCa01] M. Z. Win and D. Cassioli, "The Ultra-Wide Bandwidth Indoor Channel: from statistical model to simulations," IEEE Document # 02284r0P802-15-SG3a.
- [WiMa02] M. Z. Win, and R. K. Mallik, "Error analysis of noncoherent M-ary FSK with postdetection EGC over correlated Nakagami and Rician channels," *IEEE Transactions on Communications*, vol. 50, issue: 3, March 2002, pp. 378-383.
- [Win98] M. Z. Win, "On the power spectral density of digital pulse streams generated by M-ary cyclostationary sequences in the presence of stationary timing jitter," *IEEE Transactions on Communications*, vol. 46, issue 9, Sept. 1998, pp.1135 – 1145.
- [Win02] M. Z. Win, "A unified spectral analysis of generalized time-hopping spread-spectrum signals in the presence of timing jitter," *IEEE J. Selected Areas Commun.*, vol. 20, No. 9, 2002, pp. 1664 – 1676.
- [WiRa97] M. Z. Win, F. Ramirez-Mireles, R. A. Scholtz, M. A. Barnes, "Ultra-wide bandwidth (UWB) signal propagation for outdoor wireless communications," *IEEE 47th Vehicular Technology Conference*, vol. 1, May 4-7, 1997 pp. 251 – 255.
- [WiSc97a] M. Z. Win and R. A. Scholtz, "Comparison of Analog and Digital Impulse Radio for Wireless Multiple-Access Communications," *IEEE International Conference on Communications*, Montreal, Canada, June 1997, pp. 91 - 95.
- [WiSc98a] M. Z. Win and Robert A. Scholtz, "On the robustness of ultra-wide bandwidth signals in dense multipath environments," *IEEE Communications Letters*, vol. 2, No. 2, February 1998, pp. 51-53.
- [WiSc98b] M. Z. Win and R. A. Scholtz, "On the energy capture of ultrawide bandwidth signals in dense multipath environments," *IEEE Communications Letters*, vol. 2, No. 9, September 1998, pp. 245-247.
- [WiSc98c] M. Z. Win and Robert A. Scholtz, "Impulse Radio--How it Works", *IEEE Communications Letters*, vol. 2, No. 2, February 1998, pp. 36-38.
- [WiSc00] M. Z. Win and R. A. Scholtz, "Ultra-wide bandwidth time-hopping spread-spectrum impulse radio for wireless multiple-access communications," *IEEE Transactions on Communication*, vol. 48, April 2000, pp. 679 - 691.

- [WiSc02] M. Z. Win and R. A. Scholtz, "Characterization of ultra-wide bandwidth wireless indoor channels: a communication theoretic view," *IEEE Journal on Selected Areas in Communications*, vol. 20, No. 9, December 2002, pp. 1613-1627.
- [WiWe02] R. Wilson, R. Weaver, M. Chung, and R. Scholtz, "Ultra wideband interference effects on an amateur radio receiver," *IEEE Conference on UWBST*, 2002, pp. 315-319.
- [WiWi01] M. Z. Win, J. H. Winters, "Virtual branch analysis of symbol error probability for hybrid selection/maximal-ratio combining in Rayleigh fading," *IEEE Transactions on Communications*, vol. 49, No. 11, Nov. 2001, pp. 1926 – 1934.
- [Wong92] S. S. M. Wong, *Computational Methods in Physics and Engineering*. Prentice Hall, 1992.
- [WuNa02] Z. Wu, F. Zhu, and C. R. Nassar, "High performance Ultra-Wide Bandwidth systems via novel pulse shaping and frequency domain processing," *IEEE conference on Ultra Wide-band Systems and Technologies*, 2002, pp. 53 – 58.
- [WuNa02] Z. Wu, F. Zhu, and C. R. Nassar, "Ultra Wideband Time Hopping Systems: Performance and Throughput Enhancement via Frequency Domain Processing," *Conference Record of the Thirty-Sixth Asilomar Conference on Signals, Systems and Computers*, vol. 1, Nov. 3-6, 2002, pp. 722 –727.
- [WuNa01] Z. Wu, C. R. Nassar, and S. Shattil, "Ultra Wide- band DS-CDMA via Innovations in Chip Shaping," *IEEE Vehicular Technology Conference*, vol. 4, Oct. 7-11, 2001, pp. 2470-2474.
- [YaGo03] R. Yao, Z. Gao, Z. Chen, and W. Zhu, "UWB multipath channel model based on time-domain UTD technique," *IEEE Global Telecommunications Conference*, December 2003, pp. 1205-1210.
- [Yeap04] Y. W. Yeap, "Low Cost and Low Power UWB Ultra-Short Impulse Generator," [online], Available: <http://www.ntu.edu.sg/home/EYWYeap/>
- [ZeAn03] D. Zeng, A. Annamalai, and A. I. Zaghoul, "Pulse Shaping Filter Design in UWB system," *IEEE conference on Ultra Wideband Systems and Technologies*, Reston, Virginia, Nov. 16-19, 2003, pp. 66-70.

- [Zere99] "The 3G force," Red Herring, [Online], available at: <http://www.redherring.com/mag/issue69/news-threegee.html>.
- [Zhan97] Q. T. Zhange, "Probability of error for equal-gain combiners over Rayleigh channels: some closed-form solutions," *IEEE Transactions on Communications*, Mar. 1997, vol. 45, pp. 270 – 273.
- [ZhLe98] Y. Zhao, J. D. Leclercq, and S. G. Haggman, "Intercarrier interference of compression in OFDM communication systems by using correlative coding," *IEEE Communications Letters*, vol. 2, No. 8, August 1998, pp. 214-216.
- [ZhWu02] F. Zhu, Z. Wu, and C. R. Nassar, "Generalized fading channel model with application to UWB," *IEEE Conference UWBST02*, May 2002, pp. 13-17.
- [ZhHa01] L. Zhao, A. M. Haimovich, and H. Grebel, "Performance of ultra-wideband communications in the presence of interference," *IEEE proceedings of 2001 ICC*, 2001, pp.2948-2952.
- [ZhYa04] Z. Zheng, Z. Yang, C. Pan, and Y. Zhu, "Performance analysis of the OFDM-based systems with nonlinear distortion and imperfect parameters estimation," *IEEE Trans. Consumer Electronics*, vol. 5, No. 3, August 2004, pp. 835 – 843.
- [ZoWu95] W. Y. Zou and Y. Wu, "COFDM: An overview," *IEEE Transactions on Broadcasting*, vol. 41, No. 1, March 1995, pp. 1-8.

9 Appendix A. Instantaneous SER of Common Modulation Schemes

Modulation Scheme	Symbol Error Probability [AnTe00]
Coherent BPSK	$0.5\text{erfc}(\sqrt{\gamma})$
Coherent detection of DBPSK	$\text{erfc}(\sqrt{\gamma}) - 0.5\text{erfc}^2(\sqrt{\gamma})$
Coherent BFSK	$0.5\text{erfc}(\sqrt{\gamma/2})$
DBPSK	$0.5 \exp(-\gamma)$
Noncoherent BFSK	$0.5 \exp(-\gamma/2)$
MSK	$\text{erfc}(\sqrt{\gamma/2}) - 0.25\text{erfc}^2(\sqrt{\gamma/2})$
$\pi/4$ DQPSK	$\frac{1}{2\pi} \int_0^\pi \exp\left(\frac{-2\gamma}{2 - \sqrt{2} \cos\theta}\right) d\theta$
Square QAM	$2\text{erfc}(\sqrt{p\gamma}) - q^2\text{erfc}^2(\sqrt{p\gamma})$ where $q = 1 - 1/\sqrt{M}$, $p = 1.5/(M - 1)$
MPSK	$\frac{1}{\pi} \int_0^{\pi-\pi/M} \exp\left(\frac{-\gamma \sin^2(\pi/M)}{\sin^2\theta}\right) d\theta$
MDPSK	Closed form: $\frac{1}{\pi} \int_0^{\pi-\pi/M} \exp\left(\frac{-\gamma \sin^2(\pi/M)}{\sin^2\theta + \sin^2(\theta + \pi/M)}\right) d\theta$ [Pawu01] Approximation: $\text{erfc}\left(\frac{\gamma}{\sqrt{1+2\gamma}} \sin(\pi/M)\right)$ [BuLe64] or $\text{erfc}(\sqrt{\gamma} \sin[\pi/(\sqrt{2}M)])$ [ArDy62] or $\sqrt{\frac{1 + \cos(\pi/M)}{2 \cos(\pi/M)}} \text{erfc}(\sqrt{\gamma\{1 - \cos(\pi/M)\}})$ [PuRi82]

10 Appendix B. Elliptic Filter Coefficients Calculation Formulas

The pass band attenuation, A_p , and stop band attenuation, A_s , should be specified in the desired filter magnitude response. According to the pass band and stop band frequency transition, selectivity factor, k , and order number, n , can be calculated following equations from 5.4 to 5.9. Then the filter coefficients of equation 5.1 can be computed as follows [Anto93].

$$\Lambda = \frac{1}{2n} \ln \frac{10^{0.05A_p} + 1}{10^{0.05A_p} - 1}$$

$$\sigma_0 = \left| \frac{2q^{1/4} \sum_{m=0}^{\infty} (-1)^m q^{m(m+1)} \sinh[(2m+1)\Lambda]}{1 + 2 \sum_{m=1}^{\infty} (-1)^m q^{m^2} \cosh 2m\Lambda} \right|$$

$$W = \sqrt{(1 + k\sigma_0^2) \left(1 + \frac{\sigma_0^2}{k}\right)}$$

$$\Omega_i = \frac{2q^{1/4} \sum_{m=0}^{\infty} (-1)^m q^{m(m+1)} \sin \frac{(2m+1)\pi\mu}{n}}{1 + 2 \sum_{m=1}^{\infty} (-1)^m q^{m^2} \cos \frac{2m\pi\mu}{n}}$$

$$\mu = \begin{cases} i & \text{for odd } n \\ i - \frac{1}{2} & \text{for even } n \end{cases} \quad i = 1, 2, \dots, r$$

$$V_i = \sqrt{(1 - k\Omega_i^2) \left(1 - \frac{\Omega_i^2}{k}\right)}$$

$$a_{0i} = \frac{1}{\Omega_i^2}$$

$$b_{0i} = \frac{(\sigma_0 V_i)^2 + (\Omega_i W)^2}{(1 + \sigma_0^2 \Omega_i^2)^2}$$

$$b_{1i} = \frac{2\sigma_0 V_i}{1 + \sigma_0^2 \Omega_i^2}$$

$$H_0 = \begin{cases} \sigma_0 \prod_{i=1}^r \frac{b_{0i}}{a_{0i}} & \text{for odd } n \\ 10^{-0.05A_p} \prod_{i=1}^r \frac{b_{0i}}{a_{0i}} & \text{for even } n \end{cases}$$

11 Vita

Dongsong Zeng is currently employed as a system scientist at Honeywell International. In this role, he conducted system research on VDL mode 2, VDL mode 3, SATCOM, ATN, software defined radio, 802.15.4, 802.11, weather radar, avionics, and so on.

Prior to this position, he was a DSP engineer at Glocom Inc., which is a world-wide satellite communication company. In this role, he worked with a team of communication experts to design and develop channel cards and mobile terminals for various INMARSAT services. Through several years of intensive industrial experience, he has gained a clear understanding and a deep insight into communication transceiver, software radio, speech coding, antennas, RF, and DSP algorithms.

Prior to joining Glocom Inc., Dongsong was a software engineer at Venture Measurement Inc., which is a measurement instrument designer and manufacturer. In this role, he designed and implemented multi-level measurement equipment using phase tracking algorithms.

Dongsong Zeng is a member of IEEE society. He has published, spoken, and reviewed both nationally and internationally on UWB communications and various other topics. He was also a reviewer for IEEE WCNC 2004.

Dongsong holds a B.S. in Electrical Engineering from Tsinghua University, a M.S. in Electrical Engineering from Michigan State University. He is currently a Ph.D candidate in the department of Electrical and Computer Engineering at Virginia Tech, Northern Virginia Center. He expects to complete his Ph.D degree in the year of 2005. His research focuses on the interference issues in the UWB communication systems.